Towards the First Imaging Atmospheric Cherenkov Telescope Camera with Continuous Signal Digitization

---

Dissertation

zur

Erlangung der naturwissenschaftlichen Doktorwürde
(Dr. sc. nat.)

vorgelegt der

Mathematisch-naturwissenschaftlichen Fakultät

der

Universität Zürich

von

Arno Gadola

von

Disentis/Mustér GR

Promotionskomitee

Prof. Dr. Ulrich Straumann (Vorsitz)
Dr. Aaron G. Manalaysay
Dr. Thomas Kihm

Zürich, 2013

- Dedicau a mes geniturs -

The most exciting phrase to hear in science, the one that heralds the most discoveries, is not "Eureka!", but "That's funny..."

- Isaac Asimov -

Abstract

High-energy gamma-ray astroparticle physics has shown in the past 50 years great improvement in the instruments used for observations. Interesting results from space-borne and ground-based observatories have given a new exciting view of the non-thermal picture of the universe. Many known cosmic sources of electromagnetic radiation have been confirmed in the high-energy gamma-ray spectrum and new sources have been discovered. In particular, the ground-based imaging atmospheric Cherenkov technique (IACT) has allowed physicists to push the measurements of high-energy gamma rays to higher sensitivities. The current IACT telescopes still offer room for improvement of their detection electronics, trigger algorithms, etc.

This thesis presents a new concept for a ground-based IACT telescope camera that is based on a fully digital trigger and a continuous digitization of the photo-detector signals. Furthermore, it introduces a modular system that allows for various types of photo-detectors to be used with the same acquisition electronics, without having to adapt or change the readout system of the detectors. A new concept of using linear-nonlinear amplifiers for the analogue detector signals to allow for a huge dynamic range in a single signal channel has been introduced, to avoid the common practice of splitting the signal from each pixel into two separate readout channels. The concept allows the handling of the large signal dynamic range with a single signal path, hence reducing the number of analogue-to-digital converters (ADC), the number of subsequent readout-processors, and the data stream. The transfer characteristics of the analogue path with the linear-nonlinear amplifier has been studied and optimized for the use with photomultiplier tubes as detectors. The specially developed digitization electronics with 250 MSps ADCs is used for a continuous digitization of the analogue signal and for the transfer of the data to a computer. Several aspects of this new IACT camera have been studied and the results will help to lead towards the first large camera prototype.

Zusammenfassung

Die Hochenergie-Astrophysik hat in den letzten 50 Jahren grosse technische Fortschritte bei den verwendeten Beobachtungsinstrumenten und Datenanalysetechniken verzeichnen können. Orbitale und erdgebundene Observatorien haben eine neue Sicht auf das nicht-thermische Bild unseres Universums erlaubt und interessante Ergebnisse geliefert. Viele bereits bekannte kosmische Quellen von elektromagnetischer Strahlung konnten im Hochenergie-Gamma-Spektrum bestätigt werden und neue Quellen wurden entdeckt. Die erdgebundene Atmosphären Cherenkov Technik (IACT) hat Physikern erlaubt, die Präzision der Messungen der hochenergetischen Gamma-Strahlen zu erhöhen. Trotz des grossen technischen Fortschrittes gibt es immer noch Raum für Verbesserungen und Optimierungen der Detektionselektronik, Triggerimplementionen, etc.

Diese Arbeit präsentiert ein neues Kamera Konzept für erdgebundene IACT Teleskope, das auf einem vollständig digitalen Trigger und einer kontinuierlichen Digitalisierung der Fotodetektor-Signalen basiert. Des Weiteren wird ein modulares System eingeführt, welches verschiedene Arten von Fotodetektoren bedienen kann, ohne Anpassungen oder Änderungen am Auslesesystem vornehmen zu müssen. Ein neuartiges Konzept mit einem Verstärker mit einer teilweise linearen und teilweise nichtlinearen Übertragungskennlinie erlaubt, im Gegensatz zu dem weit verbreiteten Konzept eines dualen Signalpfades, einen grossen dynamischen Signalbereich mit einem einzigen Signalpfad pro Pixel abzudecken. Dies reduziert die Anzahl benötigter Analog-zu-Digital Wandler (ADC), sowie die Anzahl nachfolgender Prozessoren und die zu verarbeitenden Datenmenge. Die Übertragungscharakteristik des analogen Signalpfades unter Verwendung des linearen-nichtlinearen Verstärkers wurden studiert und für den Gebrauch von Fotovervielfacher-Röhren Detektoren optimiert. Die speziell für diesen Zweck entwickelte Digitalisierungselektronik verwendet 250 MSps ADCs und wird zur kontinuierlichen Digitalisierung der analogen Signale und zum Transfer der Daten zu einem Rechner verwendet. Verschiedene Aspekte dieser neuen IACT Kamera sind studiert worden und die Ergebnisse werden helfen, den ersten Kameraprototypen zu verwirklichen.

Contents

Chapter 1

Introduction

Astroparticle physics is the research field about elementary particles with astrophysical origin. It emerged at the beginning of the 20th century while seeking for a further source of ionizing radiation beside the known gamma rays from radioactive nuclei found in the earth's crust. The physicist Theodor Wulf measured 1910 the ionization of air at the top (300 m) and at the bottom of the Eiffel Tower in Paris and found that the radiation intensity decreased with altitude confirming the terrestrial origin of the radiation [1]. However, the radiation intensity did not vanish completely, as a purely terrestrial origin of the radiation would have predicted. He suggested further measurements with kites and balloons to investigate the radiation behavior in higher altitudes. The Swiss physicist A. Gockel [2] measured in balloon flights at the end of 1909 the ionization radiation up to a height of 4500 m above sea level. Although he found that the intensity did not drop as expected, he could not draw a final conclusion. The Austrian physicist Viktor Hess finally succeeded in August 1912 with balloon flights to take measurements of the ionization radiation up to heights of ~5500 m above sea level. The measured flux decreased as seen before during the first few hundred meters but increased with higher altitudes up to twice the values measured on ground level [3]. Hess concluded that the origin of the measured radiation had to be found beyond the earth's atmosphere. Balloon flights up to 9 km height in 1913/14 by W. Kolhörster did not only confirm Hess's measurements, but also showed a further increase of the radiation above 5 km altitude. In 1928/29, W. Bothe and Kolhörster demonstrated with Geiger-Müller detectors that the extraterrestrial ionizing radiation consisted of charged particles. Later, in the 1930s, R. A. Milikan coined the term *cosmic rays*, believing that the cosmic rays consisted of high-energy photons rather than charged particles. Nowadays, the term cosmic rays is used for both charged particles and high-energy photons, gamma rays, coming from outer space. The main portion of the cosmic rays are protons (~85%) followed by alpha particles (~12%), heavier nuclei up to uranium (~3%) and electrons and gamma rays (~1%). Cosmic neutrinos are also considered to be part of the cosmic rays, eventhough their overall flux is unknown.

The energy spectrum of the charged cosmic rays is shown in figure 1.1. The particle flux ϕ that is detectable with space-born and ground-based experiments, is given in numbers of particles per energy interval, area, solid angle and time interval:

$$\phi(E) = \frac{dN}{dE\,dA\,d\Omega\,dt} \tag{1.1}$$

The rather featureless energy spectrum drops rapidly with increasing energy having a particle flux which is reduced by about a factor 1000 for 10 times higher energy. It may be divided into four regions:

- the spectrum rolls-off below 30 GeV because the earth's magnetic field deflects and diffuses the particles
- it follows a power law with spectral index γ = -2.7 ($\phi(E) = \phi_0 E^{\gamma}$) from several GeV up to the so called 'knee' around 10^{15} eV
- the spectrum becomes steeper above the 'knee' and follows a power law with γ = -3.0 from 10^{16} eV to the 'ankle' at 10^{18} eV
- above the 'ankle', the spectrum flattens slightly.

The Greisen-Kuzmin-Zatsepin (GZK) cutoff at 6x10^{19} eV describes the theoretical upper energy limit for cosmic rays observable in our vicinity. Cosmic rays, mainly protons, with energies above 4x10^{19} eV, interact with the cosmic microwave background (CMB, ~230 μeV $\approx$ 2.7 K) in the reaction

$$\gamma + p \rightarrow \Delta^+ \rightarrow p + \pi^0 \quad \text{or} \quad n + \pi^+ \tag{1.2}$$

due to the transformation of the CMB to very-high energy photons in the rest frame of the cosmic rays. The mean energy of the ultra-high-energy cosmic rays drops below 10^{20} eV after about 100 Mpc (1 parsec = 1 pc = 3.0857x10^{16} m) [4]. Sources of ultra-high-energy cosmic rays have to be of extragalactic origin since there are no known sources for such cosmic rays in our galaxy. It is very difficult to measure the limit due to the extremely low particle count (about 0.005 particles per km^2 per year) and the non-isotropy of the particles. Charged cosmic particles with energies below

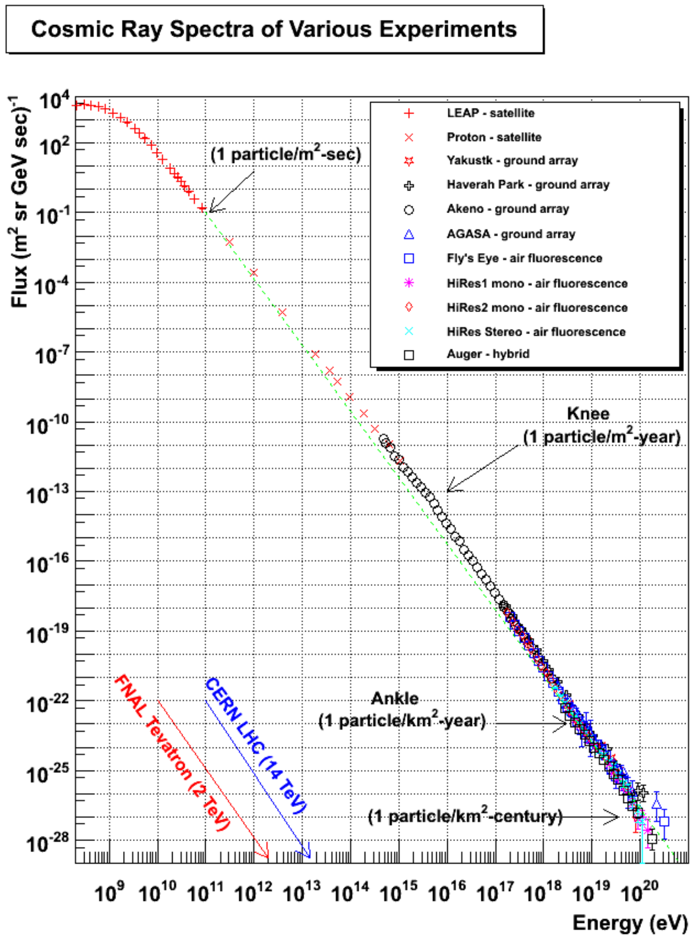

Figure 1.1: Differential energy spectrum of charged cosmic rays with data from different experiments. The colored arrows show the center-of-mass energy $E_{C.M.}$ of the current proton-proton collider LHC [5] and the discontinued Tevatron. The current LHC $E_{C.M.}$ = 7x10^{12} eV will soon be increased to its designed 14x10^{12} eV, which translates into a single particle energy in the rest frame of the other particle of $E = E^2_{C.M.}/(2m_{proton}) \approx 10^{17}$ eV. This is still three orders of magnitude smaller than the largest cosmic particle energies seen so far. Picture taken from [6].

30 GeV are deflected and diffused by the earth's magnetic field, as mentioned. This is true for all charged particles with the difference that particles with higher energies need stronger magnetic fields to be deflected significantly. Such magnetic fields can be found all over the cosmos [7]. These fields deflect the charged particles in all directions and thus produce an isotropic source of charged cosmic rays reaching the earth. Hence charged cosmic particles do not point back to their origin. However, they can be assigned to a type of source by the energy spectra and the accompanying particles or rays. This restricts the exploration of localized sources to observations of electromagnetic rays and neutrinos.

Within the electromagnetic spectrum, gamma rays with energies $\gtrsim$100 keV are of particular interest because they are produced in non-thermal processes. The following sections give a more detailed discussion of the cosmic gamma-rays, their origin, production, and detection.

1.1 The gamma-ray energy spectrum

Visible light has wavelengths of 380 nm (blue) to 740 nm (red) corresponding to energies of about 3.4 to 1.7 eV. The relation between energy E, wavelength λ and frequency ν is given as

$$E = \frac{hc}{\lambda} = h\nu \tag{1.3}$$

with Planck's constant h and the velocity of light in vacuum c. This is only a very tiny part of the whole electromagnetic spectrum, which extends over more than 35 orders of magnitude. Many experiments already exist to cover the detection of all wavelength bands so that stellar and interstellar objects can be seen in the very different 'lights', they emit. Each wavelength band gives a different inside view into the objects observed and enable us to understand them better. Especially high-energy gamma rays give a very interesting inside view, since their production cannot be of thermal origin. As a comparison: the black-body radiation of a star like our sun covers a range of 15x10^6 K (~1.3 keV) at the core to around 5000 K (~0.4 eV) at the surface. High-energy gamma-rays start off with about 100 keV and go up to several hundreds of EeV (10^{18}). It is useful to classify some regions in this huge energy interval, and a common classification is shown in table 1.1.

Band	Low/medium	High	Very high	Ultra high
Shorthand	LE/ME	HE	VHE	UHE
Range	0.1-30 MeV	0.03-100 GeV	0.1-100 TeV	>100 TeV
Detection	Space	Space	Ground-based	Ground-based

Table 1.1: Classification of the gamma-ray energy bands as described by T. C. Weekes [8] and their possible detection environment.

1.2 High-energy and very high-energy gamma-rays

The HE and VHE gamma rays are of great interest since their detection can be done with dedicated telescopes in space and on ground, the event statistics are large, and the detection techniques quite mature. These non-thermally produced gamma rays can tell us about working principles taking place in many cosmic objects and they may even provide a candidate to indirectly detect dark matter [9].

1.2.1 Sources of HE and VHE gamma-rays

The HE and VHE gamma rays cannot be of thermal origin, as stated before. Using Wien's modified displacement law with Planck's constant k_B

$$T(K) = \frac{E(eV)}{k_B} = \frac{E(eV)}{8.617 \cdot 10^{-5} \frac{\mathrm{eV}}{\mathrm{K}}} \tag{1.4}$$

shows that a blackbody with an emitted maximum photon energy of 30 MeV would have a temperature of about 3.5x10^{11} K, which is more than four orders of magnitude larger than our sun. Sources of HE and VHE gamma rays involve high dynamic magnetic fields, relativistic particles and probably the most violent surroundings existing in the universe. Such places can be found in our galaxy (galactic sources) and or outside our galaxy (extragalactic sources).

Galactic sources:

The galactic plane and center

The observation of the sky in gamma rays shows that a significant fraction of the observed rate comes from the galactic plane with increasing density towards the galactic center [10]. Several VHE gamma ray sources in the galactic plane and center could already be identified and localized, as figure 1.2 shows. Localizing a source within the galactic plane is difficult since the largest part (~75%) of the gamma rays comes from a diffuse emission, being strongest in the galactic plane but spanning as well over the whole sky. The diffuse gamma ray emission results mainly from interactions of charged cosmic rays with the interstellar gas and dust, but also some extragalactic sources, too faint to be localized, contribute. Dark matter annihilation, as described in section 1.2.2, may also contribute to the diffuse emission, especially in the galactic center [11]. An intense radio source, the Sagittarius A* (Sgr A*) which is likely to be a supermassive black hole, is localized in the center of our galaxy and radiates HE and VHE gamma rays [12]. These gamma rays can for example be observed by ground-based gamma-ray telescopes, located on the southern hemisphere.

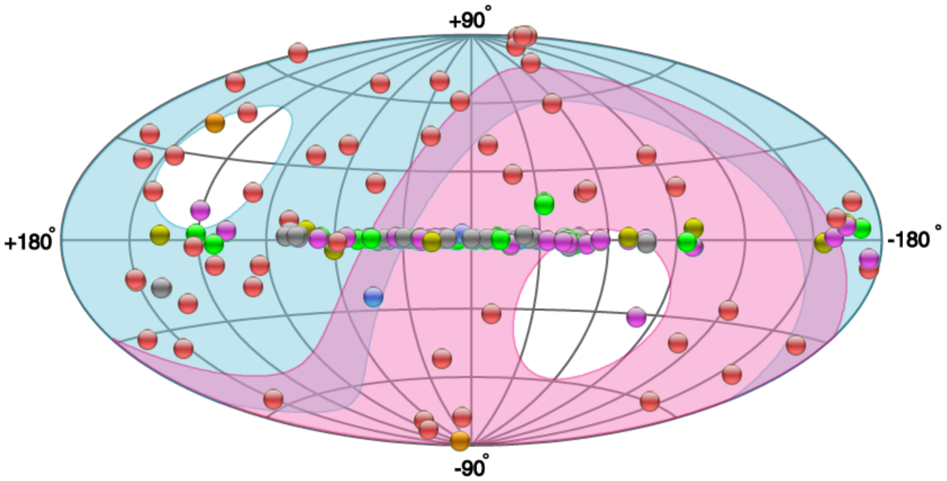

Figure 1.2: All-sky map of the known VHE sources from the TeVCat catalog plotted in galactic coordinates. Each colored point denotes a TeV gamma-ray source. The colors correspond to: pulsar wind nebula (magenta), starburst (orange), active galactic nuclei (red), supernova remnants (green), binary systems (yellow), others identified (blue) and others unidentified (gray). The background colors show the visible sky for the H.E.S.S. telescopes (pink) and VERITAS/MAGIC telescopes (blue). The overlap of the telescopes is violet. The white spots are the blind regions of the telescopes (zenith angle >50° with respect to perpendicular to ground). Taken on January 2013 from the TeVCat catalog [13].

Supernova remnants and pulsars

A normal star constantly burns hydrogen such that radiation pressure balances the gravitational pressure, hence preventing the star from collapsing. Towards the end of the star's life, when the hydrogen is exhausted in the core, the star will start to collapse under its own weight. This releases gravitational energy that heats the core of the star inducing the burning of helium, again preventing the star to collapse. The collapse of the star continues as the helium runs short and rising core temperatures start to allow the fusion of heavier elements through the helium products. Since heavier elements than iron cannot be produced by fusion, the processes stops latest with the production of iron (no further energy is released by the fusion of iron) and the star collapses subsequently.

A star with a size greater than our sun will explode at the end of its life as a supernova, one of the most luminous events known. The supernova explosion will eject almost all material of the star in a shock front that travels through space with about 20000 km/s [14]. The remains of the star will be packed by gravity into a small, incredibly dense neutron star or, if the star was large enough, even into a black hole (this is then called a hypernova). Some neutron stars are highly magnetized, rotating rapidly with frequencies in the order of milliseconds to seconds and emitting a beam of electromagnetic radiation. These neutron stars are called pulsars and their beam can be seen each time it points to the earth. The slowing down of the rotation can be explained by the electromagnetic emission and by the pulsar wind leaving the pulsar's magnetosphere carrying away rotational energy. This stream of particles causes the nebula, a cloud of dust and light ionized gases from the dead star, forming the pulsar wind nebula that remains even after the supernova remnant has disappeared, to expand further. Such violent surroundings are capable of producing HE and VHE gamma rays through inverse Compton scattering or shock acceleration (see section 1.2.2).

The Milky Way hosts one of the strongest and steadiest gamma-ray sources that can be observed from earth. The supernova explosion of the Crab was observed in 1054. The Crab nebula, located on the outermost right side of the all-sky map in figure 1.2 indicated as a pulsar wind nebula (magenta point), is the supernova remnant (SNR) and the pulsar wind nebula (PWN) of the supernova, located in the Perseus Arm of the galaxy. It is visible from the northern and the southern hemisphere and was the first detected VHE gamma-ray source. The gamma-ray energies are spread over a wide range from about 100 MeV up to 100 TeV [15]. Figure 1.3 shows the multi-waveband spectrum of the Crab nebula. The proximity of the Crab nebula and its continuous and steady gamma-ray emission has made it a standard candle, a source of reference for most other measured sources. It was only recently that instabilities, flares of gamma-rays with energies in the GeV and TeV regime, have been observed by the FERMI satellite [16] and the ground-based observatory ARGO-YBJ [17].

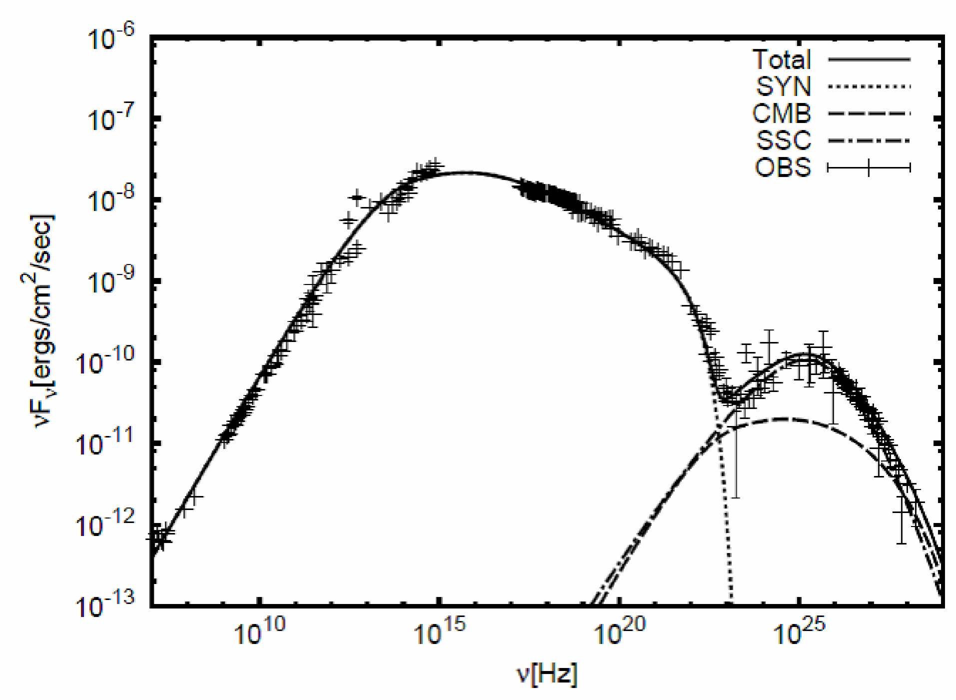

Figure 1.3: Multiwaveband spectrum of the Crab nebula. The solid line denotes the simulated total spectrum composed of the synchrotron (dotted line), inverse Compton (dashed line) and synchrotron self-Compton (dotted-dashed line) spectra. The observed data (OBS) are a combination of measurements taken with radio to VHE gamma-ray experiments. Taken from [15].

Binary systems

A normal star with an accompanying neutron star, pulsar or black hole orbiting around a common mass center is a subgroup of binary systems. The heavy and compact companion can accrete gas and matter from the normal star by its gravitational field. The accreting flow is either turned directly into radiation (mostly X-rays) or collected in an accretion disc. The accretion [18] releases gravitational potential energy, called accretion-luminosity, which heats up the gas to a hot plasma. The plasma generates very strong magnetic fields making a binary system an excellent particle accelerator and hence a source for HE and VHE gamma-rays.

Extragalactic sources:

Active galactic nuclei

Active galactic nuclei (AGN) are very luminous and compact regions in the center of some galaxies. A possible model for an AGN is a supermassive black hole (10^5-10^{10} solar masses) in the center of the galaxy, accreting mass [19]. The accretion of mass and the rotation of the system make particles of the gas and dust collide and possibly ionize, creating a hot plasma. Magnetic fields deflect the ionized particles and hence produce electromagnetic radiation. If the accretion rate is high enough, two highly collimated jets of ultra-relativistic particles form perpendicular to the accretion disc. The hot plasma outflow of the jets produces electromagnetic radiation up to the highest energies. The radiation can be seen in all wavebands from radio, IR, optical, UV, X-rays and gamma-rays, depending on the type of AGN. The terms blazar, quasar, BL Lac and others define the line of sight an AGN's jet is seen.

Gamma-ray bursts

Gamma-ray bursts (GRB) are very bright flashes of gamma rays occurring uniformly distributed over the whole universe. They are among the most violent and most luminous incidents in the universe and last for milliseconds to several minutes. The energy released with a GRB is comparable to the energy our sun releases in its entire life. An afterglow with longer wavelengths (X-rays to radio) is usually observed after the initial GRB [20]. A hypernova explosion seems to be an excellent candidate for GRBs, though it is unclear if other mechanisms like colliding neutron stars or exploding mini black holes could produce such enormously energetic outbursts.

1.2.2 HE and VHE gamma-ray production mechanisms

High-energy gamma rays can be produced in a number of sources like supernovae and their remnants, pulsars, active galactic nuclei (AGN) and black holes, as described before. The non-thermal mechanisms which allow the production of such high energies are:

- synchrotron radiation and synchrotron self-Compton
- Bremsstrahlung
- inverse Compton scattering

- shock wave acceleration
- π^0 decay: $\pi^0 \rightarrow \gamma + \gamma$
- Standard Model matter-antimatter annihilation
- dark matter annihilation: $\chi + \bar{\chi} \rightarrow \gamma + \gamma$

Synchrotron radiation, synchrotron self-Compton and Bremsstrahlung

All charged particles emit electromagnetic radiation when accelerated. The produced radiation due to acceleration in a magnetic field is called synchrotron radiation, and in an electric field (e.g. the Coulomb field of a nucleus) Bremsstrahlung. The radiation carries away energy quanta in the range of some keV (X-rays) to GeV (gamma rays). In cosmology, most synchrotron and Bremsstrahlung radiation is produced by electrons due to their low mass. The power of the radiated photons for both processes follows a continuous spectrum. The total power P radiated by a charged particle with energy E_p can be calculated with the generalized relativistic Larmor equation integrated over the whole solid angle of 4π

$$P = \frac{q^2\gamma^6}{6\pi\epsilon_0 c}(\dot{\beta}^2 - (\vec{\beta} \times \dot{\vec{\beta}})^2) \tag{1.5}$$

with $\beta = v/c$ the velocity of the particle, q the charge of the particle and $\gamma = 1/\sqrt{1-\beta^2}$ the Lorentz factor. The two special cases for the velocity v perpendicular and parallel to the acceleration a of the particle and with the relativistic energy $E_p = \gamma mc^2$ lead to

$$P_{v\perp a} = \frac{q^2\gamma^4 a^2}{6\pi\epsilon_0 c^3} = \frac{q^2 E_p^4 a^2}{6\pi\epsilon_0 m^4 c^{11}} \propto \left(\frac{E_p}{m}\right)^4 \tag{1.6}$$

and

$$P_{v||a} = \frac{q^2\gamma^6 a^2}{6\pi\epsilon_0 c^3} = \frac{q^2 E_p^6 a^2}{6\pi\epsilon_0 m^6 c^{15}} \propto \left(\frac{E_p}{m}\right)^6 . \tag{1.7}$$

Since the acceleration of the charged particle in the magnetic field is perpendicular $\vec{F} = m\vec{a} = q\vec{v} \times \vec{B}$ to the velocity and assuming a relativistic particle with $v \approx c$ we can use the Lorentz force equation to get

$$a = \frac{q}{\gamma m} vB \tag{1.8}$$

Putting this equation in 1.6 and using $v \approx c$ leads to

$$P_{synchrotron} = \frac{q^4}{6\pi\epsilon_0 m^4 c^5} B^2 E_p^2 \tag{1.9}$$

It is obvious that light-weight electrons are most efficient to produce synchrotron radiation since the radiation power is proportional to m^{-4}. For Bremsstrahlung with the Coulomb force $\vec{F} = m\vec{a} = q\vec{E}$ and hence $v||a$ using equation 1.7 with the particle energy E_p we get

$$P_{bremsstrahlung} = \frac{q^4}{6\pi\epsilon_0 m^6 c^{11}} |\vec{E}|^2 E_p^4 \tag{1.10}$$

Also here it is obvious that electrons are most likely to produce high energy Bremsstrahlung. Figure 1.4 shows the two processes with an electron deflected by the Coulomb field of a nucleus producing Bremsstrahlung and an electron spiraling around a magnetic field line producing synchrotron radiation.

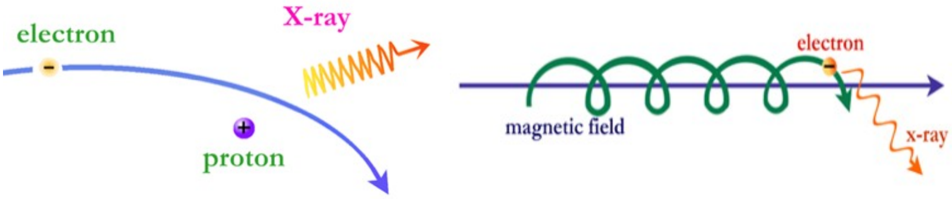

Figure 1.4: The processes of Bremsstrahlung in the Coulomb field of a nucleus and of synchrotron radiation by an electron spiraling a magnetic field line. Pictures taken from [21].

The synchrotron self-Compton mechanism (SSC) involves the same relativistic electrons in two processes. First, low energy synchrotron photons are produced by the deflected electrons. These photons are then shifted up to X-rays and gamma rays by inverse Compton scattering on the same population of electrons. Observed ultra-high energy gamma rays in some of the most extreme AGNs could originate from the special case where the energy density of the synchrotron photons is so high that the electrons lose almost all energy by the SSC process [22]. The photons may then be scattered off several times to gain such energies.

Inverse Compton scattering

In Compton scattering a photon scatters of elastically from a shell or free electron transferring a part of its energy to the electron. The inverse Compton (IC) scattering in contrast involves low-energy photons scattering off highly relativistic electrons, thus gaining a huge amount of energy and hence slowing down the electron. Low energy photons can be photons from the cosmic microwave background (CMB) with about 2.7 K (~230 μeV), photons from starlight with ~1 eV, synchrotron and Bremsstrahlung photons as well as other low energy photons. The relativistic electrons were previously accelerated for example in supernovae or AGNs.The IC process is a non-thermal process, since it does not depend on the temperature of the particles involved. The IC energy spectrum looks similar to the spectrum of synchrotron radiation as shown in figure 1.5. The inverse Compton scattering produces energies of very high values up to TeV.

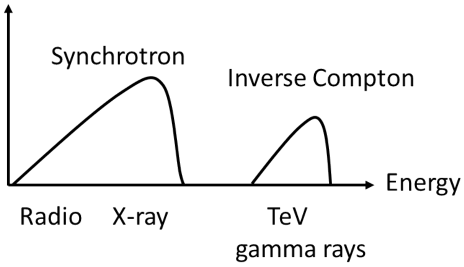

Figure 1.5: Electromagnetic spectrum as produced by synchrotron radiation and inverse Compton scattering.

The maximal energy $E_{\gamma max}$ a photon can gain through IC can be estimated with

$$E_{\gamma max} \approx 4\gamma^4 E_\gamma \tag{1.11}$$

where γ is the Lorentz factor of the electron and E_γ the initial energy of the photon. Figure 1.6 shows the multi wavelength spectrum of the supernova RX J1713. The synchrotron part on the left side is rather low-energy and visible with radio and X-ray telescopes. The inverse Compton, π^0 decay and non-thermal Bremsstrahlung parts on the right side above 10^7 eV can only be measured with dedicated gamma-ray telescopes in space or on the ground, described in section 1.5.

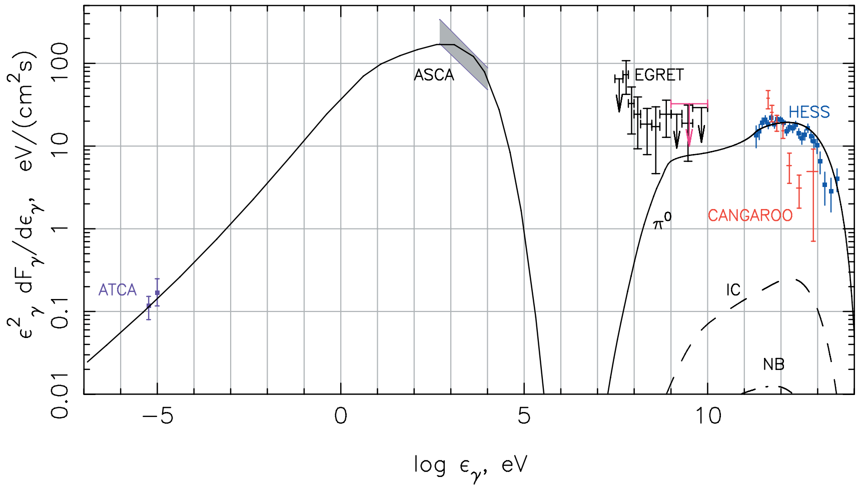

Figure 1.6: Spatially integrated spectral energy distribution of the supernova remnant RX J1713.7-3946. The energy distribution below 10^6 eV corresponds to the synchrotron radiation. Above 10^7 eV the contributions come from gamma-ray emission of π^0 decay (solid line), inverse Compton scattering (dashed line) and non-thermal Bremsstrahlung (dashed-dotted line). EGRET data are from the nearby unidentified source 3EG J1714-3857, which is probably not physically associated to the supernova remnant RX J1713. Picture taken from [23].

Shock wave acceleration

A shock front of material is produced when a star ends its life in a supernova explosion. The shock front will hit particles of the interstellar medium and reflect them. This interaction with the shock front can accelerate the interstellar particles shifting them to much higher energies. A similar effect is possible with particles trapped between two shock fronts where the inner one has a much higher velocity than the outer front. The particles bounce back and forth and may gain energy. Maximum energies of about 100 TeV can be reached this way [19].

π^0 decay

The neutral pion π^0 is the most frequently produced neutral particle in hadronic interactions and decays. Since protons are the most abundant particles of the interstellar medium it may be produced in proton-antiproton annihilation ($p + \bar{p} \rightarrow \pi^+ + \pi^- + \pi^0$) or by proton-nucleus interaction ($p + nucleus \rightarrow p' + nucleus' + \pi^+ + \pi^- + \pi^0$). The π^0 has a life time of 8.4x10^{-17} s and decays with 98.8% branching ratio into two photons. These photons are already high-energy photons due to the kinetic pion energy or they may be shifted to higher energies for example by IC.

Standard Model matter-antimatter annihilation

The annihilation of Standard Model matter and antimatter particles can directly produce photons like in the case of electrons and positrons

$$e^+ + e^- \rightarrow \gamma + \gamma \tag{1.12}$$

or indirectly over a secondary product like in the case of the proton-antiproton annihilation

$$p + \bar{p} \rightarrow \pi^+ + \pi^- + \pi^0 \tag{1.13}$$

where the π^0 decays into two photons.

Dark matter annihilation

The universe consists of ~4.6% ordinary baryonic matter. What exactly the other constituents, the dark matter (~23%) and the dark energy (~72%), are, is still a matter of speculation. However, an evidence for the existence of dark matter can be found in the rotation curves of galaxies. The curve describes the dependence of the rotational velocity of the visible matter like stars and dust of a galaxy and its radial distance from the center of the galaxy. The Newtonian mechanics predicts a decreasing of the velocity with $v(r) \propto 1/\sqrt{r}$ but measurements show an approximately constant velocity. This can only be explained with the existence of dark matter [24]. These dark matter particles could annihilate into two photons and be a viable source for GeV to TeV gamma rays [25].

1.3 Detection physics

The cosmic rays are composed of charged particles and gamma rays as already mentioned. The processes involved in the interaction with the earth's atmosphere depend on the type of particle. Protons and nuclei interact through the strong and the electroweak force, electrons through the electroweak force and gammas through the electromagnetic force. Three possible processes are involved in gammas interacting with matter: the photoeffect ($\gamma + atom \rightarrow e^- + ion$), Compton scattering ($\gamma + e^- \rightarrow \gamma + e^-$) and pair production ($\gamma + Z \rightarrow e^+ + e^- + Z$). The interactions happen at different altitudes in the atmosphere, depending on the primary particle's type and energy. A proton interacts already at a height of about 20 km, a high-energy gamma ray only at about 10 km above sea level. Here, the pair production is the only important interaction process for high-energy gamma rays.

Understanding the effects of the interaction of photons with matter as well as the generation and development of particle showers in the atmosphere is essential to understand the detection instruments and techniques used in gamma-ray astronomy. The following discussion gives a brief introduction to the phenomena of these effects.

1.3.1 Photon interaction

Photons interact with matter in three dominant ways, depending on the photon energy (figure 1.7). The photo-electric effect dominates for photon energies below twice the electron mass of $m_e c^2 = 511\,\mathrm{keV}$ and for heavy materials with a high atomic number of the absorber. The photon is thereby completely absorbed by an atom, which releases a photoelectron from one of its shells. The effect is most likely if the photon energy is just above the binding energy of a shell electron. The photo-electric effect is forbidden for free electrons due to energy and momentum conservation.

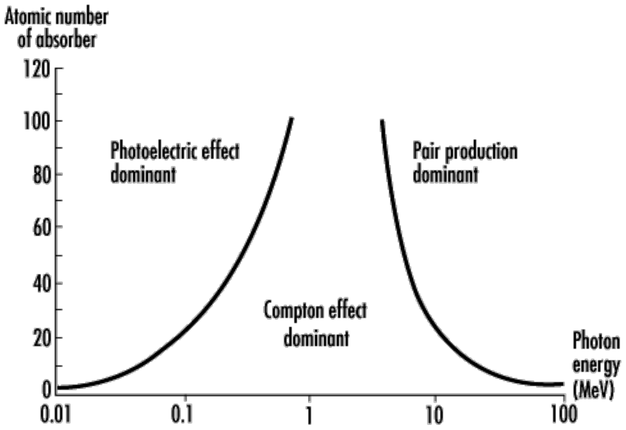

Figure 1.7: The three photon interaction processes with matter and their dominate energy regions in function of the absorber's matter density. Picture taken from [26]

The Compton effect or Compton scattering is most dominant around 1 MeV. A photon scattering off a matter electron or a free electron transfers energy to the electron. The transfered energy can vary from zero to a very large fraction of the photon's energy taking energy and momentum conservation into account. The photon energy $h\nu'$ after the scattering on an electron with mass $m_e c^2$ is described in equation 1.14, where $h\nu$ is the photon energy before the scattering and θ the scattering angle. The Compton electron energy E_e is given in equation 1.15 for free electrons.

$$h\nu' = \frac{h\nu}{1 + \frac{h\nu}{m_e c^2}(1 - \cos\theta)} \tag{1.14}$$

$$E_e = \frac{h\nu}{1 + \frac{m_e c^2}{h\nu}\frac{1}{\cos\theta}} \tag{1.15}$$

The third interaction, the electron-positron pair production, has its energy threshold at above twice the electron mass (1.022 MeV) and becomes dominant at energies $\gtrsim$10 MeV. The photon hence has enough energy to create an electron positron pair in the Coulomb field of a nucleus or of a shell electron, transferring all its energy to the pair particles. The energy equation for the electron-positron pair and the incident photon is:

$$E_{e^+} + E_{e^-} = h\nu - 1.022\,MeV \tag{1.16}$$

The energy threshold for the process is given by:

$$E_\gamma = 2m_ec^2 + 2\frac{m_e^2c^4}{M_N} \approx 2m_ec^2 \tag{1.17}$$

where m_e is the mass of the electron and M_N the mass of the nucleus.

1.3.2 Cherenkov effect

Charged particles traveling through a medium polarize atoms and molecules along their trajectory. This polarization will eventually relax and like a dipole produce electromagnetic radiation. The radiation of the polarized atoms and molecules will interfere destructively due to the symmetrical polarization of the medium (figure 1.8(b)) and not be detectable. If the charged particle travels faster through the medium than light does, then the polarization is no more symmetric and the radiation will have some constructive interference and the produced radiation will become observable. Figure 1.8(a) shows a charged particle traveling through a medium with a velocity v, smaller than the velocity of light c', in the medium. Figure (b) shows the same picture with $v>c'$.

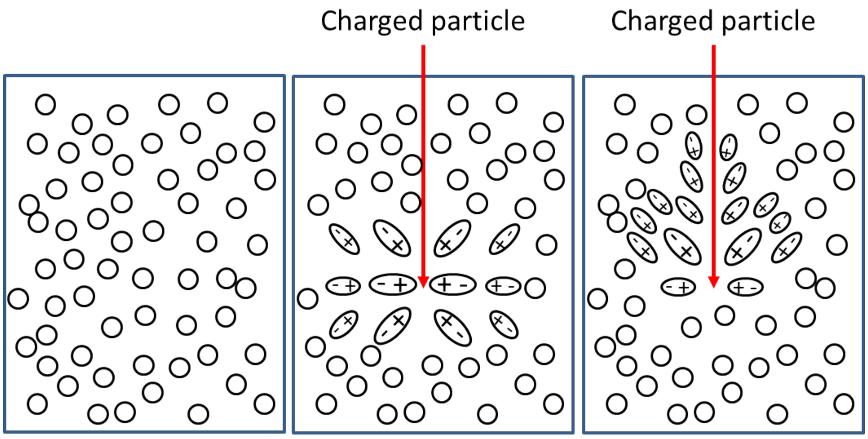

Figure 1.8: Polarization of a medium by a negatively charged particle passing through. Left pictures shows the undisturbed medium. Middle: The particle traveling with a velocity below the velocity of light in the medium polarizes the medium in its vicinity symmetrically. The electromagnetic radiation produced by the relaxation of the medium interferes destructively. Right: Constructive interference happens only when the particle's velocity is greater than the velocity of light in the medium, allowing for constructive interference.

The red line represents the wave front of the constructively interfered waves. The opening angle θ_C changes with the velocity and the refractive index n of the medium as:

$$\cos(\theta_C) = \frac{1}{n\beta} \tag{1.18}$$

where $\beta = v/c$ and c the speed of light in vacuum. The condition that the cosine is limited to ±1 leads to the energy threshold for coherent Cherenkov radiation with $\beta \geq 1/n$. The threshold energy for an electron (mc^2 = 511 keV) and for a muon (mc^2 = 106 MeV) traveling through air ($n \approx 1.00029$) or water ($n \approx 1.33$) can be calculated with

$$E_{thresh} = \frac{1}{\sqrt{1-\beta^2}} mc^2 = \frac{1}{\sqrt{1-\frac{1}{n^2}}} mc^2. \tag{1.19}$$

Table 1.2 shows the corresponding values of the threshold energies in air and in water.

Particle	Mass mc^2 [MeV]	E^{air}_{thresh} [MeV]	E^{water}_{thresh} [MeV]
Electron	0.511	21.2	0.78
Myon	106	$4.4 \text{x} 10^3$	160.8

Table 1.2: Threshold energy for Cherenkov radiation in different media.

The wave front of the Cherenkov light is shown in figure 1.9, assuming spherical waves produced by the de-polarization of the medium.

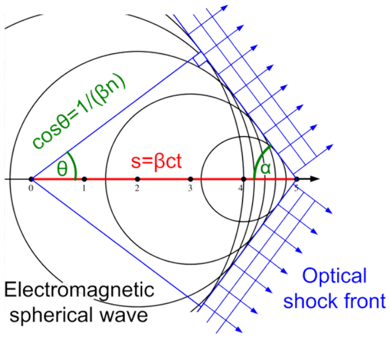

Figure 1.9: Building up of the optical shock front of the Cherenkov effect. Picture taken from Wikipedia. Information added.

The effect can be compared with the effect of an aircraft breaking the sound barrier, flying supersonic. The spherical sound waves compress more and more at the front with increasing velocity of the aircraft and finally create the shock wave front, know as sonic boom. However, the difference to the Cherenkov wave front is that the sonic boom wave front is produced by the traveling object (the aircraft) and not by the medium flown through (the de-polarizing medium).

The emitted energy dE per unit length dx and per unit of angular frequency $d\omega$ is defined by the Frank-Tamm formula [27]:

$$dE = \frac{\mu(\omega)q^2}{4\pi} \cdot \omega \cdot \left(1 - \frac{c^2}{v^2 n^2(\omega)}\right) dx d\omega \tag{1.20}$$

with $\mu(\omega)$ the frequency-dependent permeability, q the electric charge of the particle, v the particle's velocity, c the speed of light in vacuum and n the frequency-dependent refractive index. The emitted intensity is almost proportional to the frequency, or inversely proportional to the wavelength emitted ($1/\lambda$) and peaks in the ultraviolet, as shown in figure 1.10.

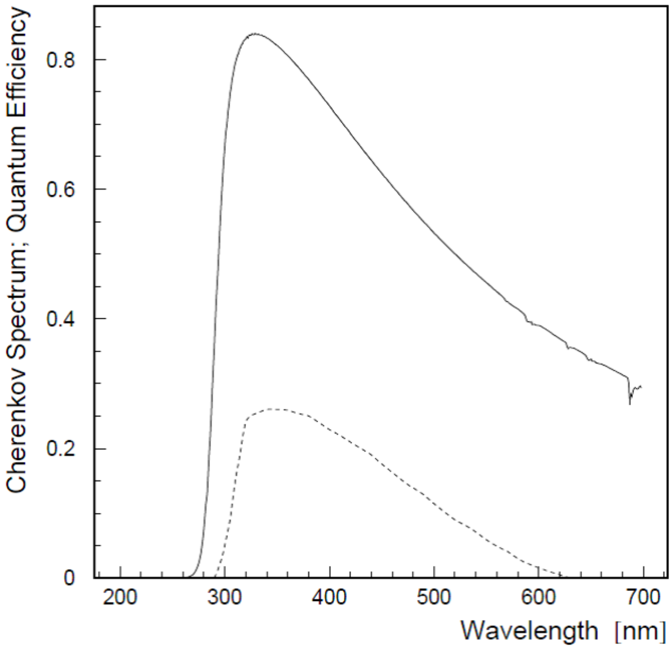

Figure 1.10: Typical Cherenkov light spectrum generated by a vertical hadronic TeV air shower as seen by the imaging atmospheric Cherenkov telescope HEGRA at 2200 m above sea level. The solid line denotes to the Cherenkov light spectrum in arbitrary units and the dashed line shows a typical quantum efficiency curve of a photomultiplier tube used in the HEGRA telescope. The Cherenkov spectrum is mainly limited on the low-wavelength side (<300 nm) by absorption of the Cherenkov photons by ozone. Taken from [28].

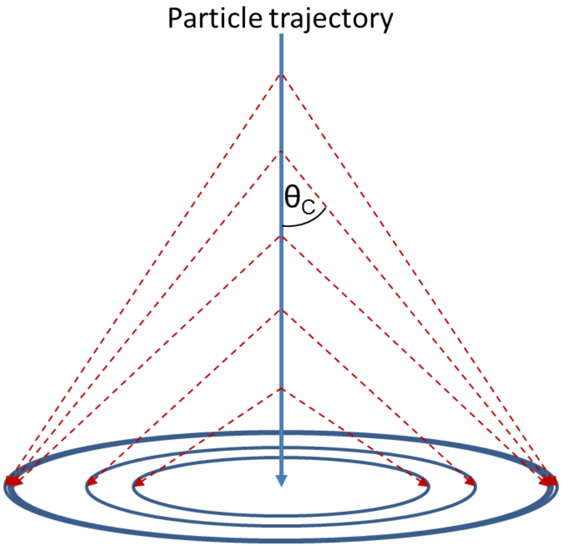

Figure 1.11: Sketch of the formation of the Cherenkov light pool on ground level due to change of the refractive index and the varying speed of the electrons inducing Cherenkov light.

The number of emitted photons dN per wavelength interval $d\lambda$ and path length dx is proportional to $1/\lambda^2$ as equation 1.21 indicates. ez is the charge of the particle, h the Planck constant.

$$\frac{d^2N}{d\lambda dx} = \frac{(2\pi ez)^2}{hc\lambda^2}\left[1 - \frac{1}{n^2(\lambda)\beta^2}\right] \tag{1.21}$$

The term $2\pi e^2/hc$ is the fine structure constant $\alpha = 1/137$ and the factor in brackets can be rewritten as $\sin^2(\theta_C)$ with equation 1.18. Integration of this equation over the expected Cherenkov wavelength spectrum of 290 to 600 nm in air leads to the following formula for an approximation of the number of emitted photons per path length in units of photons per mm:

$$\frac{dN}{dx} \approx 80 \cdot z^2 \sin^2(\theta_C) \ \ [\text{photons/mm}] \tag{1.22}$$

The Cherenkov angle θ_C for a particle traveling through the atmosphere with a velocity $\beta \approx 1$ changes from about $0°$ ($n = 1$ at 20 km a.s.l.) to $1.4°$ ($n = 1.00029$ at 0 m a.s.l.), producing a light cone (figure 1.11). The light cone is aligned with the axis of the flight trajectory of the primary particle. The light flash is very short $\mathcal{O}$(ns) since the particle travels with ultrarelativistic velocity through the atmosphere. An electromagnetic shower, as described in the next section, involves ultrarelativistic electrons and positrons, each producing a Cherenkov light cone. These cones superimpose and illuminate at ground level a circular region, like a 'pool'. Figure 1.12 shows the simulated development of an electromagnetic shower induced by a gamma ray and induced by a proton with the corresponding light pools on ground.

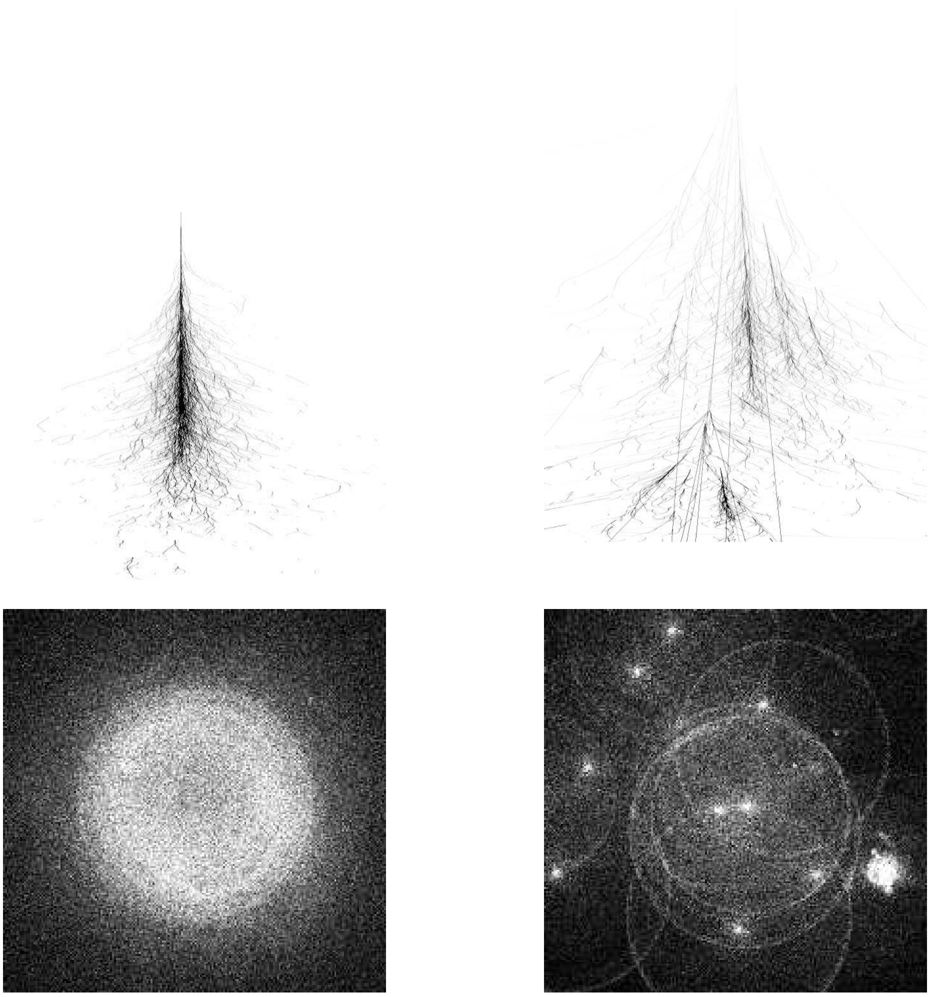

Figure 1.12: Left: Simulated development of an electromagnetic shower induced by a 300 GeV gamma-ray with the secondary particles trajectories (top) and the distribution of the Cherenkov light at ground level (bottom). The Cherenkov light is projected onto a single plane and the shown light pool section is 400 by 400 m^2. Right: Same simulation but with a proton of 1 TeV as primary particle. Picture taken from [29].

The Cherenkov photon density at sea and at mountain level, produced by

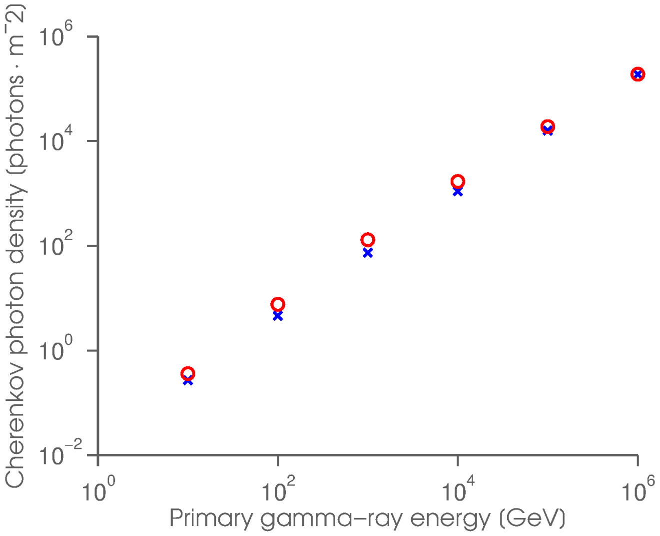

Figure 1.13: Log-log plot of the Cherenkov photon density as a function of the primary gamma-ray energy. The values are shown for sea level (blue crosses) and for a mountain level of 2300 m asl (red circles). Data taken from [8].

a primary gamma ray, is shown in figure 1.13.

1.3.3 Electromagnetic shower

A gamma ray entering the atmosphere will eventually undergo pair production in the vicinity of a nucleus and create an electron-positron pair. This production is most dominant for gamma energies >5 MeV. The pair particles, which share the gamma's energy, are relativistic, depending on the primary energy. They lose energy by Bremsstrahlung, if the energy is larger than the critical energy E_c of ~85 MeV, while moving through the electric fields of the molecules and atoms in the atmosphere. Moreover, because of their velocity, they produce Cherenkov light, as explained in the previous section. The Bremsstrahlung photons can also undergo pair production, creating an electromagnetic shower of electrons, positrons and EM radiation. Figure 1.14 shows the process of the shower development. The radiation of a Bremsstrahlung photon and the subsequent pair production happens on average after one radiation length. The leptons will eventually lose enough energy to slip under the critical energy threshold. The particles lose the remaining energy by ionization of the surrounding medium, until the shower faints out. The electromagnetic shower describes a cylinder

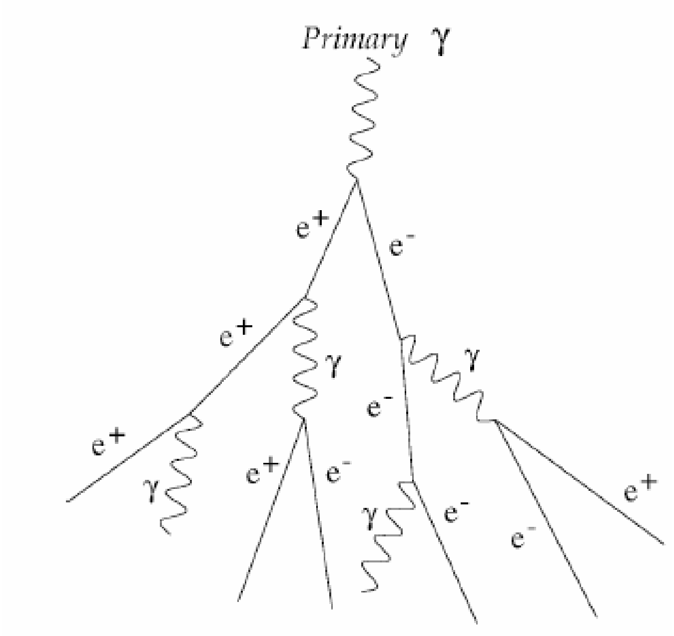

Figure 1.14: Electromagnetic shower induced by a gamma particle showing the emission of Bremsstrahlung and subsequent pair production. Picture taken from [30].

with a radius R_M, which contains 90% of the shower energy, of

$$R_M = \frac{21\,\mathrm{MeV}\,X_0}{E_c[\mathrm{MeV}]}. \tag{1.23}$$

E_c the critical energy in units of MeV (~85 MeV) and X_0 is the radiation length defined as

$$X_0 = \frac{1}{\rho} \cdot \frac{716.4 \cdot A}{Z(Z+1)\ln\frac{287}{\sqrt{Z}}}\,\mathrm{g}\cdot\mathrm{cm}^{-2} \tag{1.24}$$

with ρ the density of the medium. R_M is about 78 m in air with $\rho_{air} \approx 1.2\,\mathrm{kg/m^{-3}}$ at 20°C. The radiation length for electrons and positrons flying through air with ~78% nitrogen and ~21% oxygen and a mean atomic number of $Z = 7.14$ and a mean mass number of the nucleus $A = 14.3$ is approximately $X_0\rho \approx 37.8\,\mathrm{g/cm^2}$ at 0°C and 1 atm. The atmosphere corresponds to about 27 radiation lengths for electrons and positrons. The lateral expansion of the shower is rather small and mainly dominated by low-energy electrons at the end of the cascade.

1.3.4 Extended air shower

A shower induced by a charged cosmic particle like a proton or a heavy ion is called an extended air shower (EAS) and is shown in figure 1.15.

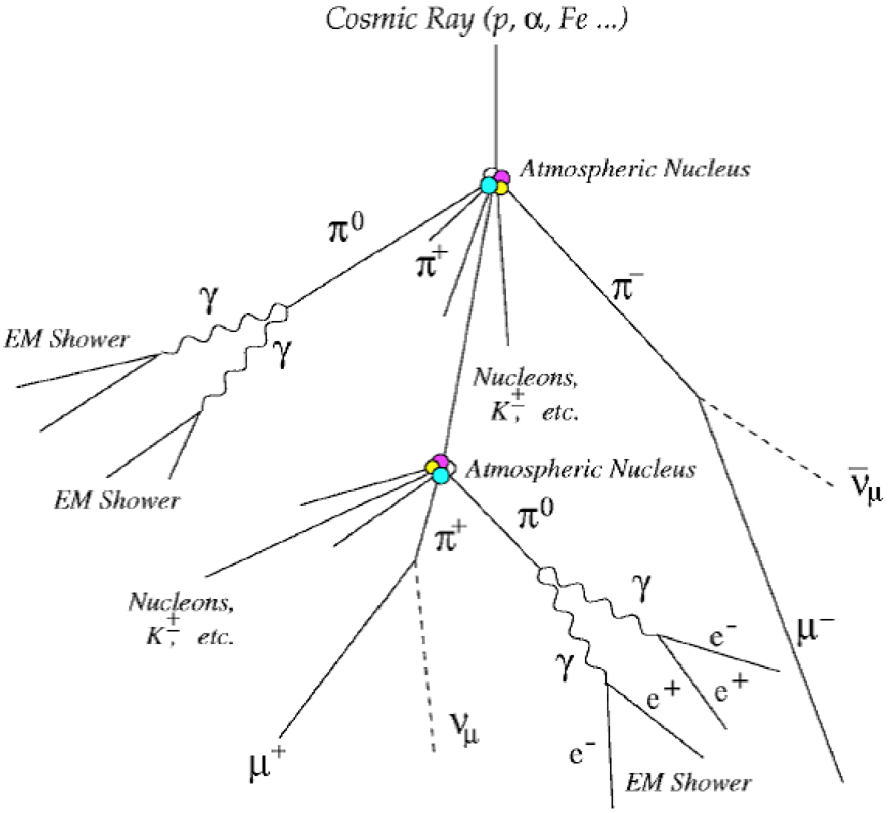

Figure 1.15: Shower induced by a proton or heavy ion. Both components of the shower are visible, the hadronic and the electromagnetic part. Picture taken from [30].

The shower consists of both hadronic and EM components, but is dominated by the hadronic particles. The most abundant secondary hadronic particles are the charged and neutral pions[1]. Other hadronic particles like kaons will decay as well very soon after their production into pions. The pions decay dominantly into the following channels [31]:

$\pi^0 \rightarrow \gamma\gamma$ (branching ratio: 98.80%, mean life time: 8.4x10^{-17} s)
$\pi^+ \rightarrow \mu^+\nu_\mu$ (branching ratio: 99.99%, mean life time: 2.6x10^{-8} s)
$\pi^- \rightarrow \mu^-\bar{\nu_\mu}$ (branching ratio: 99.99%, mean life time: 2.6x10^{-8} s)

---

[1] Each pion flavor makes about 1/3 of the total pions due to the isospin symmetry of the pions.

The π^0 predominately decays into two photons, inducing the electromagnetic cascade as described in the previous section. Muons make a large portion of the secondary particles that reach ground level, since they are ultrarelativistic and hence do not decay beforehand.
Both electromagnetic showers induced by primary gamma rays and neutral pions can be characterized by the following main parameters:

- shower axis: flight direction of the primary particle
- longitudinal dimension: distribution of the secondary particles (e^+e^-) along the shower axis
- lateral dimension: distribution of the secondary particles perpendicular to the shower axis
- impact parameter: distance of the shower center to the detector on detector level
- number of Cherenkov photons (or secondary particles for the hadronic shower): this number is proportional to the energy of the primary particle.

These parameters help to identify a primary particle, its direction and its energy. The different components of a shower can be detected with dedicated instruments as explained next.

1.4 Detection instruments

Direct detection of primary comic rays is only possible in space, since the earth's atmosphere is opaque to them. Thus, only high altitude balloon and satellite experiments may measure the flux and the properties of the cosmic rays undisturbed of the earth's atmosphere. However, the flux of VHE gamma-rays and high-energy charged cosmic rays is very small and demands large detection areas or volumes to gain sufficient statistics. Building space or balloon experiments with large detection volumes is not feasible, since space shuttles and balloons do not permit high loads or transportation is very expensive. In contrast, ground-based detectors allow much larger areas to be covered at modest prices, but may only detect the cosmic rays indirectly using the atmosphere as a calorimeter. The performance of this unique calorimeter is however not very constant in time and space and forbids the reconstruction of the energy and flight direction of the primary particle with a high accuracy. Current experiments give reconstruction accuracy numbers as low as 30% for the energy and 60% for angular reconstruction.

Ground-based detectors will either measure the secondary products like the charged component of an EAS and the accompanying fluorescence light or Cherenkov flashes, produced by the relativistic electrons and positrons. The EAS detectors have the advantage that they can be operated under all weather conditions, but with the drawback of being restricted to the ultra-high-energy cosmic rays (>10 TeV). The optical Cherenkov light, as induced by the secondary particles of gamma rays in the atmosphere, can only be measured during dark and clear nights but detection levels can reach down to gamma-ray energies of some tens of GeV. A detailed list of cosmic rays, gamma-rays, neutrino and similar experiments can be found on [32].

1.4.1 Space-borne instruments

After many missions with balloons, rockets, and aircrafts, the time for space-borne cosmic ray detectors had arrived in 1958 when the Russian Sputnik 3 satellite was launched. The satellite was equipped with cosmic rays detectors to measure the charged particle flux, gamma-rays and heavy nuclei. The US satellite Explorer, launch only a few days before Sputnik 3, discovered the Van-Allen belt[2] with built-in magnetometers. The detectors carried by these satellites were rather simple in their functionality. However, as time went by they improved and became much bigger but also more precise and more reliable, as new techniques emerged to launch heavier objects into orbit.

One of the first large space-borne experiments (15.6 t, 9.1 m height and 21.3 m width) was NASA's Compton Gamma Ray Observatory (CGRO) satellite (1991-2000). It hosted four gamma-ray dedicated experiments to cover a gamma-ray energy range of 20 keV to 30 GeV. The Energetic Gamma Ray Experiment Telescope (EGRET [33]) experiment on board of CGRO was designed to detect gamma-rays between 20 MeV and 30 GeV, while the other three experiments covered the lower energy range up to about 30 MeV. EGRET, shown in figure 1.16, consisted of two spark chambers for the detection and identification of gamma-rays by inducing pair production. A calorimeter placed beneath the spark chamber was used to determine the energy of the electron-positron pair. Plastic scintillators, placed around the main detector, were used to veto non-gamma events.

---

[2] The Van-Allen belt is a ring of high energy particles (mostly protons in the inner belt and electrons in the outer belt) captured by the earth's magnetic field.

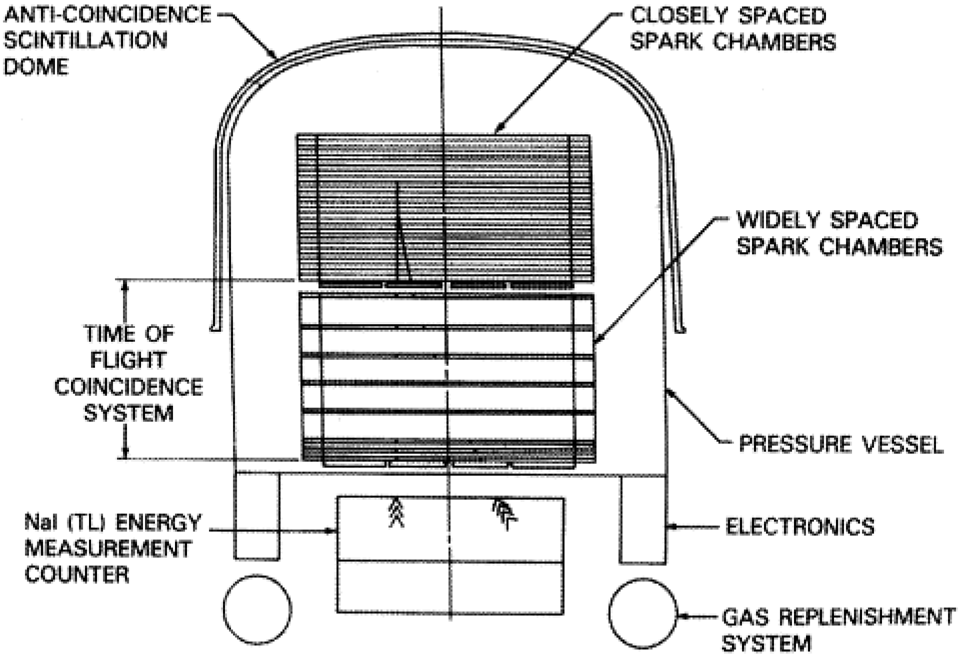

Figure 1.16: Schematical drawing of the EGRET instrument. An electron-positron pair is drawn in the spark chamber as well as the scintillation light they would produce in the NaI scintillator. Picture taken from [34].

The first year of observation already revealed a glimpse of what was hidden behind the HE energy gamma-rays. Figure 1.17 shows an all-sky map with first year data of EGRET. The Galactic plane is visible in the middle of the picture as a bright white band in this Hammer-Aitoff projection (equal-area projection). Radiation from the Galactic plane comes mainly from interactions of cosmic rays with the stellar medium. Three bright sources are already visible on the right side of the Galactic plane. They correspond to the Vela, Geminga, and Crab pulsars. The blazar 3C279 is visible on the upper half, right of the middle.

More space missions dedicated to gamma-ray physics followed EGRET and revealed new sources of gamma-rays. The FERMI [36] satellite (formerly called GLAST), launched in 2008, currently orbits the earth, taking data of gamma-rays and gamma-ray bursts. FERMI covers the photon energy range of 8 keV to 300 GeV. The satellite hosts two instruments, the Large Area Telescope (LAT) and the Gamma-ray Burst Monitor (GBM). The LAT (figure 1.18), the main detector of FERMI, is constructed similar to the EGRET system. A converter foil makes gamma rays undergo pair production. The pairs' trajectories are then tracked by the tracker system

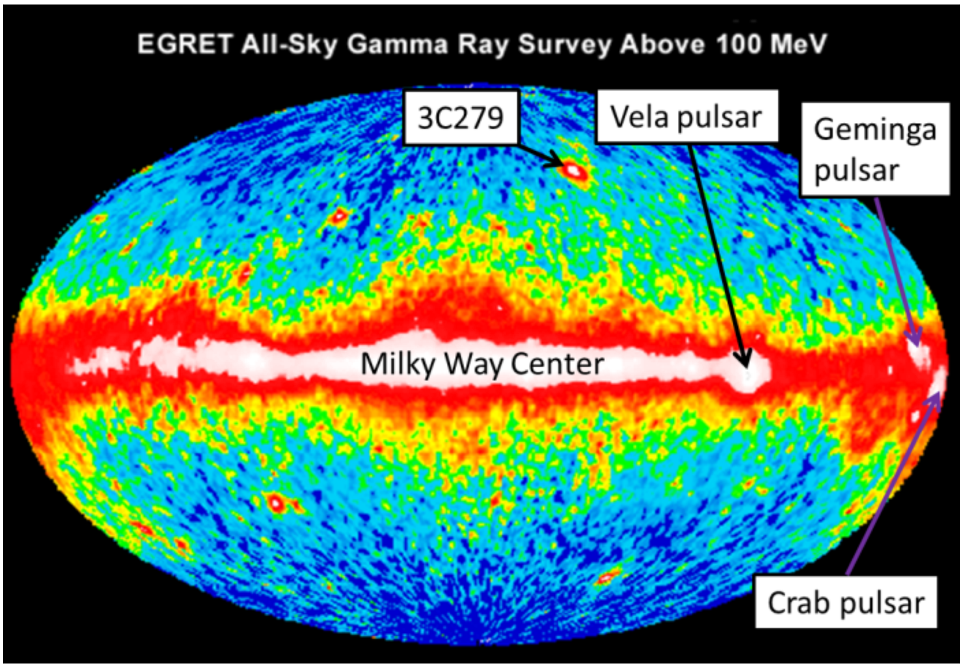

Figure 1.17: The picture shows an all-sky view of the EGRET detector with first year data of gamma-rays with energies above 100 MeV. Some bright sources as the Vela, Geminga, and Crab pulsars and the blazar 3C279 are already visible on this picture. Brighter colors correspond to brighter gamma-ray sources. Picture taken from NASA's EGRET page [35]. Labels added.

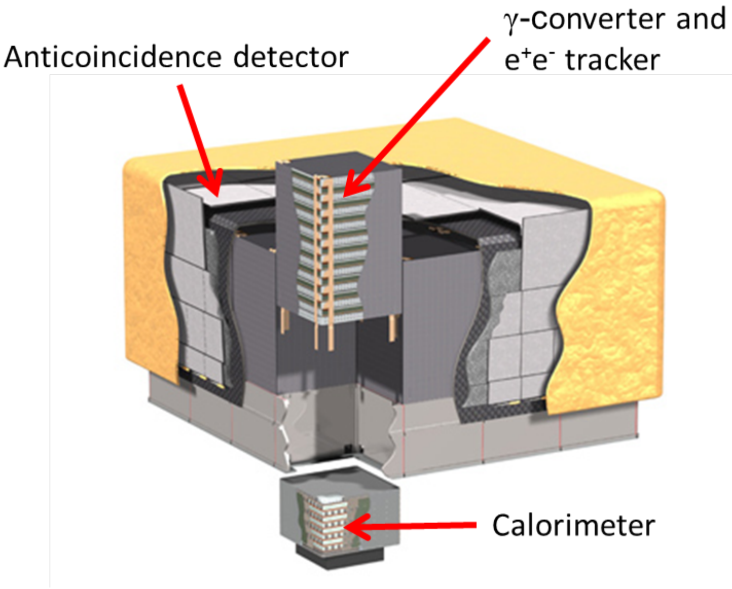

Figure 1.18: Sketch of FERMI's LAT detector. The converter/tracker consists of layers of conversion foils to force the gamma-rays to undergo pair production and particle tracking detectors to track the pair. Picture taken from [37].

similar to the spark chamber of EGRET. The calorimeter system measures the energy of the electron-positron pair as they are fully absorbed and a surrounding anticoincidence shield made of scintillating plastic is used to veto non-gamma events. The LAT detector covers the photon energy range from 30 MeV up to 300 GeV and is able to 'see' 20% of the full sky at any one time.

The GBM looks out for gamma-ray bursts, events known as the brightest in gamma-rays. Such events can be detected by the accompanying lower energy gamma-rays or X-rays. The detector needs to cover as much solid angle as possible to catch the light from the GRBs from all directions. The GBM covers photon energies of 8 keV up to 30 MeV. The LE gamma-rays are detected with NaI scintillators in a disc shape, producing scintillation light flashes that are measured with photomultiplier tubes. HE gamma-rays are measured with two additional scintillators made of bismuth germanium oxide (BGO), an inorganic scintillation material with a high stopping power.

Figure 1.19 shows the sky in gamma-rays seen by the LAT detector of the FERMI satellite. One can see the improvement in resolution compared to the EGRET image. The color scale from black to white corresponds to the

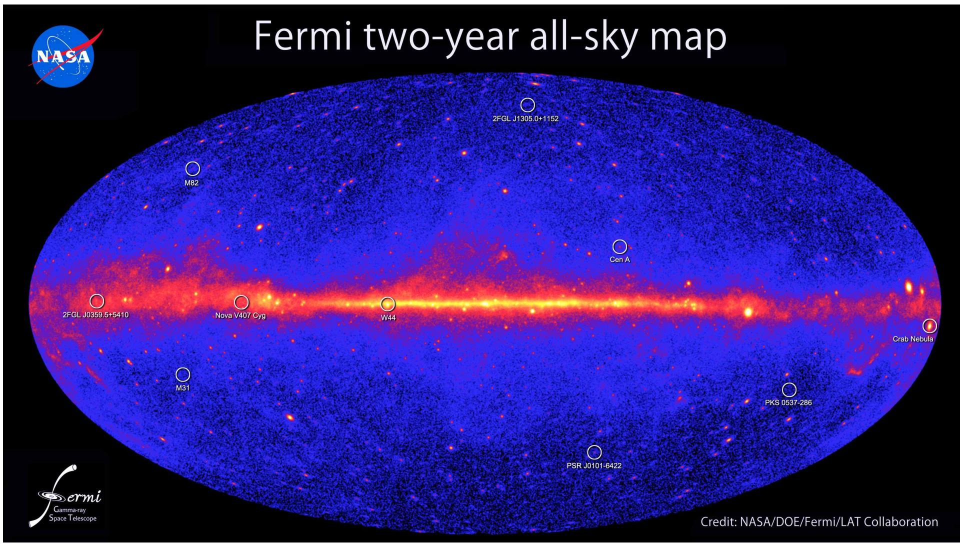

Figure 1.19: All-sky map constructed from two year FERMI data. The lower energy limit is 1 GeV. Brighter colors correspond to brighter gamma-ray sources. Picture taken from [38]. Credit: NASA/DOE/Fermi LAT Collaboration.

brightness of sources in gamma-ray.

The disadvantage of satellites is clearly their small detection area. Also, running an instrument in space is more challenging and needs matured and reliable techniques. However, the field of view of a freely flying satellite is much larger than the one of a ground-based detector and not disturbed so much by the earth's shadowing. Ground-based observatories can provide larger detection areas and hence extend the detectable energy range of gamma-rays, being a good complement to the satellites.

1.4.2 Ground-based instruments

Ground-based instruments can be divided into two categories: instruments detecting the secondary particles produced in the shower and detectors collecting the Cherenkov light produced in the shower. The Pierre Auger experiment [39] in Argentinia can detect the secondary products primarily of cosmic hadrons within an energy window of 10^{17} to 10^{20} eV. Two detectors, an array of surface detectors and a collection of air fluorescence detectors, detect the different parts as a hybrid detector. The surface detectors are

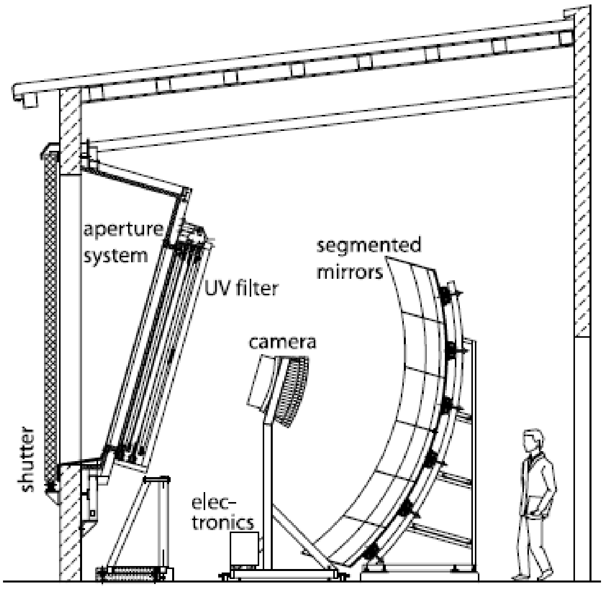

Figure 1.20: Working principle of the Pierre Auger fluorescence detector. Picture taken from [40].

tanks, each filled with 12 tons of pure water and equipped with photomultiplier tubes. These tanks are distributed as a large array (covered area is about 3000 km^2, 30 times the city of Paris). High-energy charged particles from the EAS reaching the ground and passing through the water will produce Cherenkov light. The Cherenkov light is detected by PMTs and a correlation of the signals from several tanks will give a hint if the particles are part of an EAS or not. The measured arrival time and number of particles help to reconstruct the direction and the energy of the primary particle. About 30 events with energies around 10^{20} eV are measured per year with this detector. Lower-energy primary particles are measured more often.

The second instrument used in the Pierre Auger observatory, the air fluorescence detector, measures the faint fluorescence light produced by previously excited air molecules. The air molecules are excited by the secondary photons of the EAS and emit fluorescence light while relaxing into the ground state. This can be detected by one or several of the 27 telescope detectors, each containing a tessellated mirror focusing the light onto a photomultiplier array (figure 1.20). The detector measures the longitudinal development *dE(x)/dx* of the air shower and its integral gives the approximate total energy of the primary particle since about 90% of the dissipated shower energy is electromagnetic. The direction of the primary particle

can be estimated by the shape of the fuorescence image. The combination of both numbers allows for an identification of the particle type. The fluorescence detector may, in contrast to the water tanks, only be used during moonless nights, since the detected light is very faint and in the visible light range.
Another fluorescence detector was the HiRes Fly's eye experiment in New Mexico, which observed the GZK cutoff in 2007 [41] and presented their final results in 2010 [42]. A four-square-meter mirror focuses the light onto an array of 256 PMTs. The successor, the telescope array project [43] which is designed to study the EAS of UHE cosmic rays, uses the same technique as the HiRes experiment to detect the fluorescence part of the air shower, and in addition an array of many large-surface detectors built of two stacked plastic scintillators of each $3\,\mathrm{m}^2$ and 1.2 cm thickness to cover an area of $762\,\mathrm{km}^2$.
The High-Altitude Water Cherenkov Gamma-Ray Observatory (HAWC), currently under construction, is designed to detect gamma-ray induced air showers with primary energies in the TeV regime, and additionally cosmic ray EASs. It is located at an altitude of 4100 meters above sea level in Mexico and uses the water Cherenkov technique like the Pierre Auger water tanks. However, the HAWC water tanks are much larger (4 meters high and 7.3 meters in diameter) and equipped with four PMTs per tank in a Y shape at the bottom. Both charged particles from the EAS and gamma-rays will produce a detectable Cherenkov pulse in the water. HAWC will have an energy resolution of below 50% and an angular resolution <0.2 degrees for >10 TeV primary particles.

The previously mentioned ground-based observatories look for cosmic rays and gamma rays and cover the energy range above 10 TeV. Their spatial and energy resolutions worsen towards lower energies. There, the so called Imaging Atmospheric Cherenkov Technique (IACT) steps in and covers the HE and VHE range from some tens of GeV up to some tens of TeV. The technique allows for the detection of the faint and short Cherenkov light flashes produced by charged relativistic particles of the air shower.

1.5 Imaging Atmospheric Cherenkov Technique

The story of observations with IACT telescopes started in 1952 with a dustbin and a World War II signaling mirror of 25 cm diameter with a photomultiplier tube in its focus (figure 1.21). An amplifier and an oscilloscope made

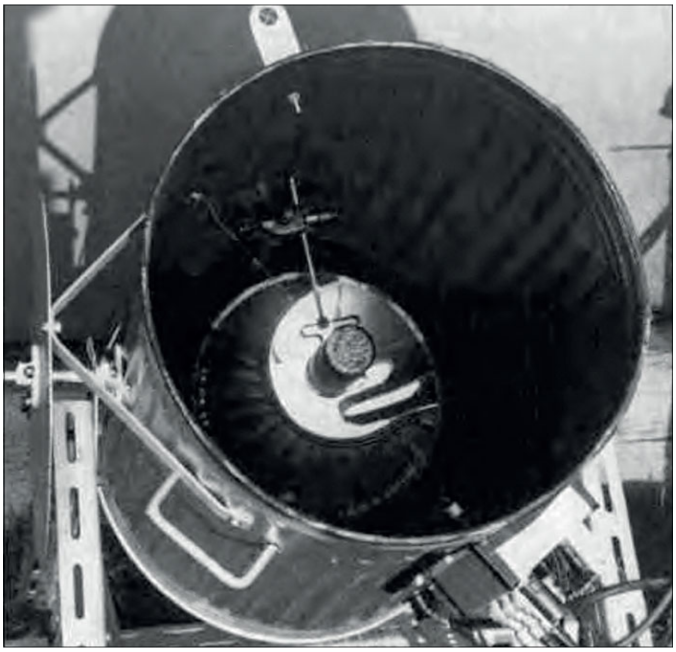

Figure 1.21: First gamma-ray 'telescope' to detect Cherenkov light flashes built of a dustbin, a small mirror and a PMT. Picture take from [44].

the first gamma-ray ground-based telescope complete. It was W. Galbraith and J. Jelley who started a completely new area of ground-based gamma-ray telescopes and opened up the new field of HE and VHE gamma-ray physics.

After the idea to collect Cherenkov light from a shower with a spherical or parabolic mirror and measure it with a detector array (camera) was born, the technique evolved and the Imaging Atmospheric Cherenkov Technique (IACT) was introduced more than 15 years later by the Whipple collaboration. However, success did not come for a long time. The 10 m Whipple telescope in southern Arizona started its operation in 1968, detecting the first HE gamma-ray source in 1977 and its first TeV gamma-ray source, the Crab Nebula, in 1989 [45]. The fundamental ideas of the IACT were developed during that time. A huge step forward was taken with the introduction of the Hillas parameters by A. M. Hillas in 1983 [46], which allow for the separation of gamma-rays from the more abundant hadron-induced showers.

Better, second generation telescopes like HEGRA, CANGAROO, CAT and TA followed. The turn of the millennium finally brought the third generation of telescopes with even better energy and direction resolution, larger cameras and dish diameters and the multi-telescope operation by VERI-

TAS (four), CANGAROO-III (four), HESS (four, five in future) and MAGIC (two since 2009). These IACT telescopes have detected a large number of sources together with satellite experiments.

1.5.1 IACT working principle

The working principle of an IACT is similar to the previously described fluorescence detectors. Hence, dark and cloudless nights far away from any artificial light sources are needed for the detection of the faint Cherenkov light. The Cherenkov light produced by an electromagnetic shower covers an area of about 50000 m^2 at ground level, depending on the primary particle energy. This is a circular shaped light pool with a radius of about 130 m for a gamma-ray impacting the atmosphere from a vertical direction (section 1.3.2). The light pool becomes more elliptic and distorted the more the impact angle deviates from the vertical incident direction. The Cherenkov light is emitted with an opening angle θ_C, which is inversely proportional to the refractive index of the atmosphere. The variation of θ_C can be captured by an IACT telescope and give information about the shower energy and direction. Figure 1.22 shows the working principle of an IACT telescope. The different parts of the cigar-shaped shower are imaged along the camera plane, producing an image which looks like an ellipse for gamma ray events. This ellipse has some outliers for a hadron induced shower or becomes even a ring for muons (figure 1.23). The Hillas parameters describe the resulting image by the width and the length of the ellipsoidal picture, the overall content (the size) of the image, the distance of the image's center of gravity (COG) to the camera's center, the angle between the ellipse major axis and the radial distance of the COG to the camera center etc. These parameters describe the lateral and vertical development of the shower, the energy of the primary particle and the position of the image in the camera etc., and allow for a better discrimination of the different primary-particle-induced events.

Such an image reconstruction is only possible after the camera image has been cleaned from 'noise' pixels, pixels with night sky background (NSB) light which does not belong to the shower[3]. The problem which arises with the Hillas parametrization is the ambiguity in the reconstructed shower and primary particle direction, respectively. This problem can be solved by stereoscopic observation of the shower as shown in figure 1.24. It is also

---

[3] The NSB is usually a combination of visible light from stars, scattered or direct moonlight, zodiacal light (sunlight scattered by space dust in the zodiacal cloud), light pollution from nearby artificial sources as cities and airplanes etc.

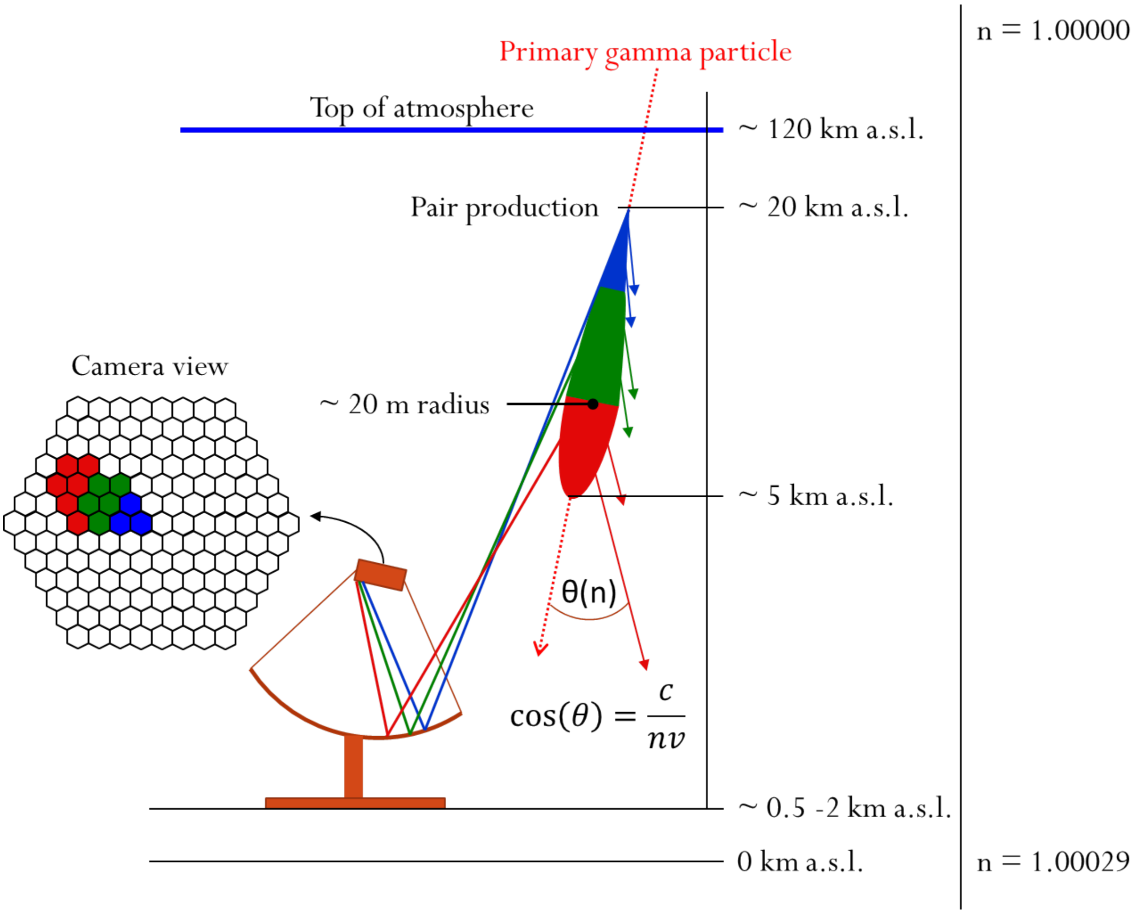

Figure 1.22: Imaging of the different Cherenkov light sections. The emission angle θ of the Cherenkov light varies with the refractive index n of the atmosphere. n changes very slightly, but enough to cause the Cherenkov light to be spread along the camera plane.

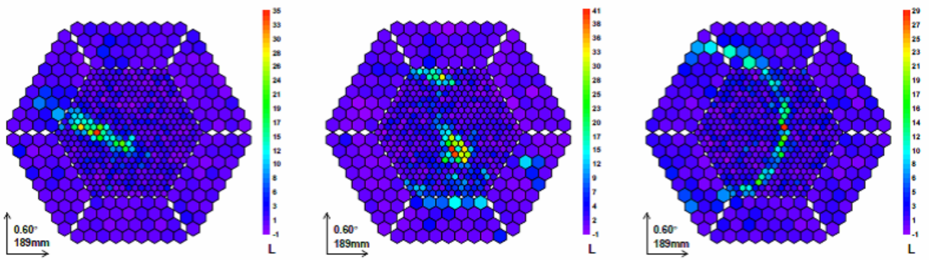

Figure 1.23: Camera images recorded by MAGIC-I during observations of the Crab nebula. The color scale denotes the amount of (Cherenkov) photons per pixel. Shown are a gamma-ray (left), a hadronic (center) and a muon (right) event. Picture taken from [47].

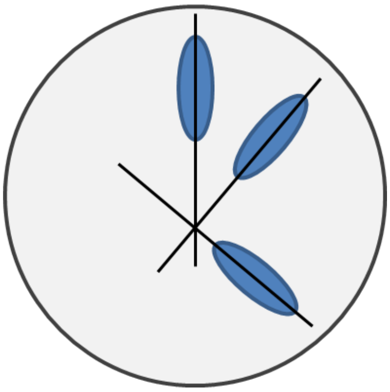

Figure 1.24: Superposition of three telescope camera images for the non ambiguous reconstruction of the shower direction.

possible, under certain conditions, to evaluate the Cherenkov photon arrival time in the camera and hence determine the evolution and direction of the shower. This however, is only possible if the camera electronics are fast enough and the signals from the photo-sensors are not integrated to get more signal. New, more sophisticated analysis methods have recently been studied, as an improved 3D model algorithm, multivariate analysis with boosted decision trees and neuronal networks etc. [48].

1.5.2 The upcoming IACT project

The Cherenkov Telescope Array (CTA) project [9], for which development and construction is in progress and first operation is expected in 2016, aims at improvement of the detection sensitivity and an extension of the detectable energy range compared to the current IACTs H.E.S.S., MAGIC, and VERITAS. A southern and a northern hemisphere array assembled with up to three different telescope sizes to cover the different energy ranges will be installed. The dish diameters will be 4-6 m (small size telescope SST), 10-12 m (mid-size telescope MST) and 24 m (large size telescope LST) for the detection of gamma-rays of energies SST >10 TeV, MST 100 to 10 TeV and LST tens to hundreds of GeV.
About 30 SSTs will be built in the southern hemisphere to detect the more rare TeV gamma rays. The 'workhorse' will be the MST with quantities in the same order as the SST. The low energy regime covered by LSTs needs large collection areas since the Cherenkov signals are extremely faint. Only four to five LST telescopes will be built, since the costs are the limiting factor. However, this will be enough since gamma rays in that energy regime are more frequent and hence good statistics is achievable with fewer tele-

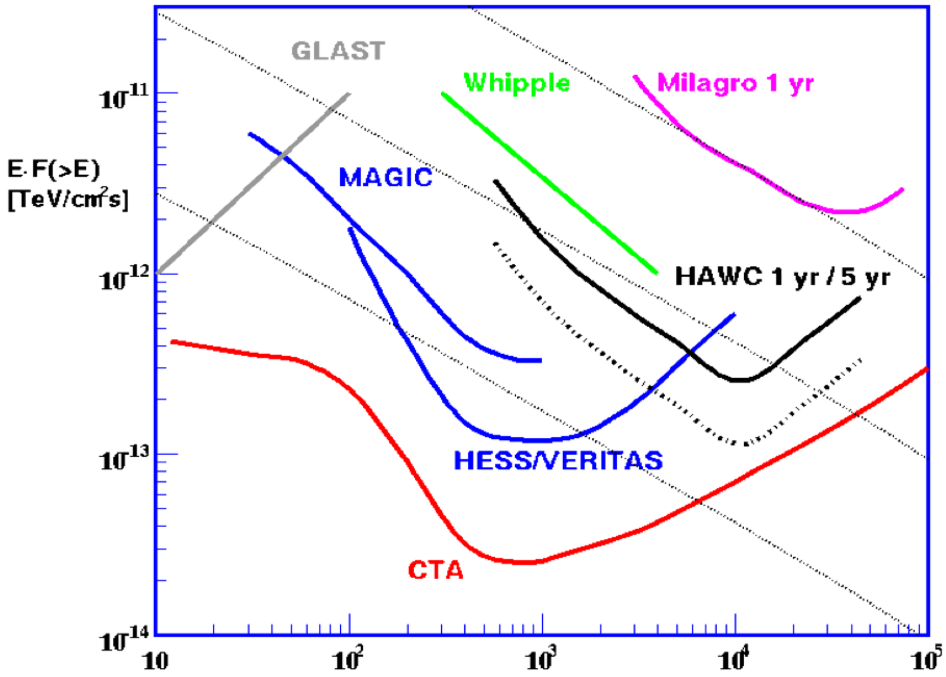

Figure 1.25: Expected integral sensitivity for a Crab-like spectrum for current IACTs and ground based cosmic particle detectors. The horizontal axis denotes the energy of the primary particle in GeV. The three dotted lines correspond to the flux from the Crab nebula and show from top to bottom: 100% Crab flux, 10% Crab flux and 1% Crab flux. The black solid (dotted) HAWC line is a 1 (5) year of HAWC exposure while the indicated IACT sensitivities correspond to 50 hours of observation. Picture taken from [50].

scopes.

The camera sensors will predominantly be photomultiplier tubes. Efforts are ongoing to build cameras with semiconductor photo-sensors for the SST or even MST. Figure 1.25 shows the expected sensitivity of CTA as a function of energy compared to the current gamma ray observatories. The design concept can be found in [49].

Chapter 2

The imaging atmospheric Cherenkov telescope camera

This chapter introduces and discusses the concept of Imaging Atmospheric Cherenkov Telescope (IACT) cameras as implemented in current telescopes. It gives a rough overview how such a camera works and discusses some specific parts in more detail. One aim of the thesis is the improvement of the existing concept and the development of a new concept to reduce power consumption and data stream, to introduce more flexibility in the camera trigger and to build a light-weight, reliable camera. This new concept and the improvements are discussed in chapter 3.

2.1 Principle of an IACT camera

An IACT camera can be compared with a commercial compact digital camera. The main differences are the mechanical size and that the IACT camera has no lenses to image a picture on the photo sensor. The parts of a compact camera are the multi-pixel photo sensor, the shutter-release button to capture an image, the fast data buffer which stores the image temporarily and a processor chip which possibly processes and compresses the image before writing it to the slower memory card. The corresponding parts of an IACT camera are photo-detectors like photomultiplier tubes (PMT), a trigger system that identifies an event, a data buffer to bypass the time to calculate the trigger and to write the data to a storage and a processor, realized with a field programmable gate array[1] (FPGA) and a storage unit

---

[1] A field programmable gate array is an integrated circuit that can be configured and programmed many times. It is designed as an array of simple logic gates like ANDs and XORs that can be arranged into more complex logical functions. Some FPGAs also host a

(computer farm or similar). Figure 2.1 shows a sketch of an IACT camera with the main parts and the signal flow.

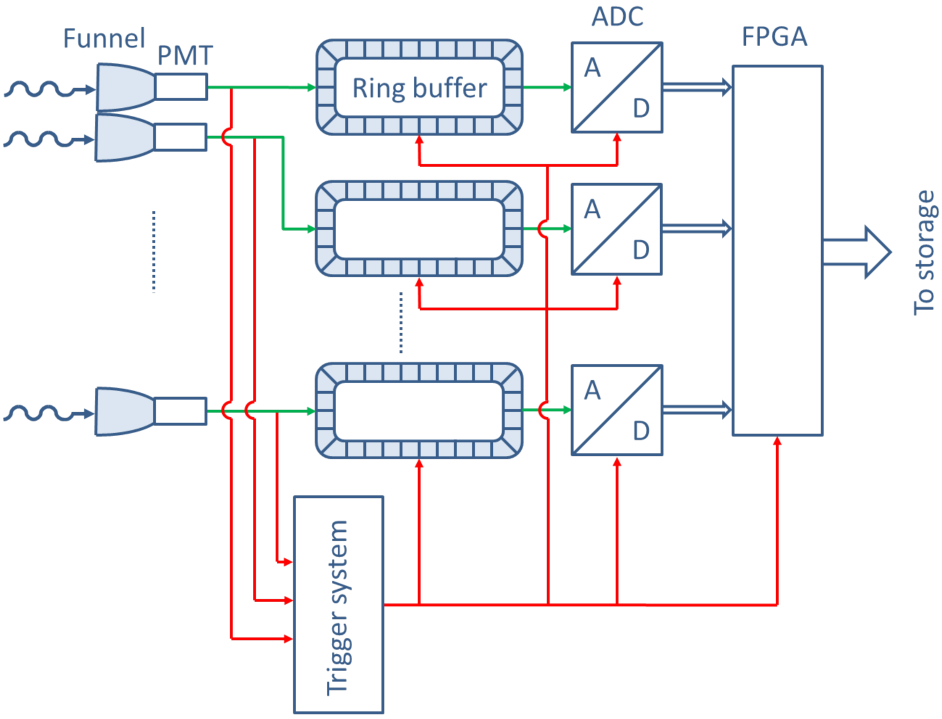

Figure 2.1: Sketch of an IACT camera. Green arrows denote the analogue signal flow, red arrows belong to the trigger system and blue arrows are digital data flows.

The photo sensor of a compact camera, a CMOS or CCD chip, consists of many small (~1-3µm) pixels sometimes having a micro-lens in front to collect the light. The IACT camera uses hollow light funnels like Winston cones [51] with reflective surfaces to collect light for a pixel. These funnels increase not only the light collection efficiency, but simultaneously restrict the field of view of a single pixel. This is necessary to prevent stray light from the ground behind the dish to be seen. Another benefit of these light funnels is their almost arbitrary selectable geometry of the entrance and exit apertures. A hexagonal entrance and exit geometry is ideal since it shows the best optical performance and allows pixels to be arranged together without leaving dead space in between.
A pixel of the photo-sensor of an IACT camera is much larger in diameter than the one of a CMOS or CCD chip. This is useful since the 'image' which

---

small microprocessor, memory blocks and even analogue features like ADCs.

is captured with the IACT camera has fewer distinct details than a an image taken with a compact camera and a smaller pixel size would not improve the information much but would increase the data stream, the number of electronics channels, and the costs. The other part of the photo sensor is the sensor itself. Most IACT cameras use photomultiplier tubes to convert the light into an electronic signal. These photo detectors are extremely sensitive and able to capture single photons. They are also rather noise-quiet compared to a CMOS or CCD chip.

The trigger system of the IACT camera can be compared to face recognition systems built in some compact cameras. These systems constantly analyze the image of the photo sensor and if they find something that looks like a human face they release the shutter and take a photo. Since there are no faces to be captured with an IACT camera, the trigger system looks for other characteristics in the picture like structures that are typical for gamma-ray events. The analysis of the picture happens also constantly but needs to be much faster, on the order of a few tens to hundreds nanoseconds. This requires very fast electronics and simple but efficient recognition algorithms. A data buffer is needed, due to the 'long' time the trigger needs to calculate a decision (almost the same order of magnitude as the shower duration). Current IACTs use analogue ring buffers, which store the analogue signals of the PMTs. A trigger event will stop the ring buffer and allow the single buffer cells to be read out. This introduces a dead time of the camera where no further events can be captured, like the compact camera. The signals from the ring buffer are digitized with analogue to digital converters (ADC) and fed into processors for further processing. The camera is ready again as soon as the FPGAs have sent the data to a storage outside the camera. All stored events are analyzed off line with more sophisticated methods to separate wanted from unwanted events, to clean images from noise, and to extract the signal from the background.

The following sections discusses the different parts and their possible implementations in more detail.

2.2 Photo-detector

2.2.1 The photomultiplier tube

The photomultiplier tube (PMT) was invented in 1930 by the Russian physicist L. A. Kubetsky [52]. A PMT is an evacuated glass tube with electrodes to convert light into an amplified electronic signal. Two main physical processes are involved. The photo-electric effect converts the photons into (photo)electrons (pe). This happens on a photoemissive semiconductor[2], called the cathode. The conversion efficiency, called quantum efficiency (QE), of the cathode is on the order of 10% to 45% of the incident photons[3]. The released photoelectrons are accelerated through an electrical field towards a first dynode (a polished metal electrode). While hitting the dynode, more electrons are released by the secondary electron emission effect multiplying the number of charged particles. This process can only take place if the primary photoelectrons have gained enough kinetic energy through the field to kick out the secondary electrons of the dynode. The multiplied charge is again accelerated and led by an electric field between the neighboring dynodes so the multiplication process continues building up an avalanche of photoelectrons until the last dynode. Finally, an electric field leads the photoelectrons to the anode where the charge is collected. An externally connected load resistor converts the charge pulse into a voltage pulse.

Figure 2.2 shows a sketch of a PMT connected to a voltage divider to create the accelerating electric fields and an external load resistor R_T.

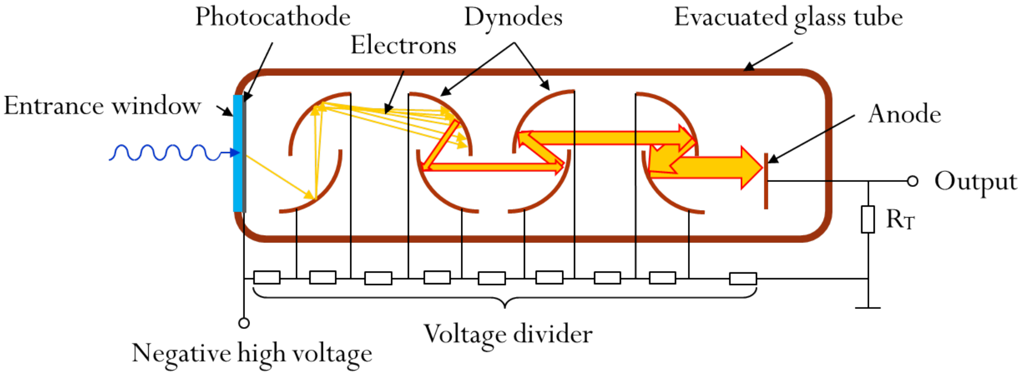

Figure 2.2: Sketch of a photomultiplier tube. The light is incident from the left, passing the entrance window, hitting the photocathode and releasing electrons. The electrons are multiplied by each dynode stage and finally collected at the anode to produce a current/voltage pulse through the load resistor R_T. The high voltage provides the electric field between the dynodes to accelerate the electrons.

---

[2] Semi-transparent cathodes are evaporated directly on the glass of the PMT windows and emit the photoelectron on the opposite side to the incident photon. Opaque cathodes are metal electrodes emitting the photoelectron on the same side as the incident photon.

[3] The QE often includes the collection efficiency (CE) of the first dynode, that is the probability that a photoelectron comming from the cathode reaches, and is amplified by the first dynode. CE values are usually greater than 80%.

The multiplication process makes the tube sensitive to single photons. A single photon will produce a charge of 10^4 to 10^8 photoelectrons at the anode, mainly depending on the number of dynodes and the applied high voltage of several hundred volts between dynodes. Intense light yield exposure of a PMT under operation will hence create a very large photoelectron current and possibly damage and age the PMT early. The aging happens through changes in the surface state of the dynodes decreasing the multiplication effect and hence the gain of the PMT. This aging is also noticeable under constant illumination, but strongly depends on the photoelectron currents inside the tube. The surface state of the dynodes changes also after long storage of the PMTs or after exposure to bright light (for example day light) without operation of the PMT. The PMT will eventually recover and reach again a stable gain after a few hours or days, depending on the storage time and light exposure (figure 2.3). Best stable performance can be expected by continuous, uninterrupted operation of the PMT with modest light yield and PMT gain.

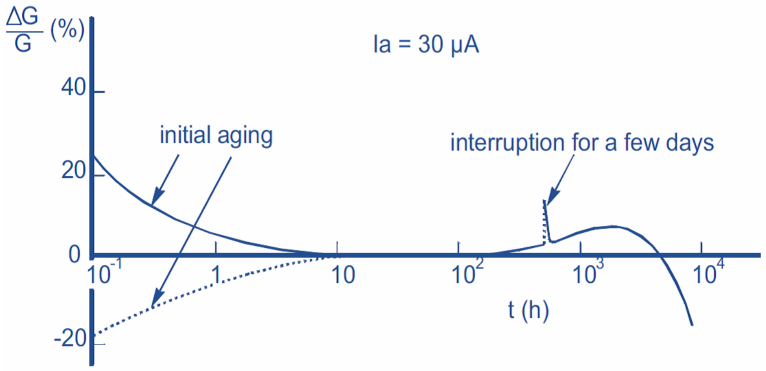

Figure 2.3: Relative gain variation over time at a high average anode current of 30 μA, normalized to the stable gain after the initial aging period. The gain drift after starting the operation life of the PMT is due to an initial aging of the PMT, taking up to 24 hours. This aging happens faster with a high anode current. The switching off of the high voltage for several days renews the PMT gain, but only for a very short time where the gain catches up again with the old value and eventually drifts to very low values. Aging of the PMT is not only due to the mean anode current, but also due to helium intrusion etc. Taken from Photonis Photomultiplier Tube Catalogue.

Photons hitting the cathode are unfortunately not the only sources producing signals that can be measured at the anode. There are two other sources for signals that cannot be distinguished from photon-events: afterpulses (AP) and dark currents. Afterpulses occur when positively ionized resid-

ual gas molecules (e.g. H_2O, CH_4, He) are accelerated by the electric fields, hitting the cathode or the first dynodes releasing electrons. Also photons emitted by luminescence of the dynodes during the bombardment with the photoelectrons can make their way back to the cathode and give rise to a signal. These afterpulses can occur after each photon event. The effect is most noticeable after exposure of the PMT to intense light pulses since the large number of released photoelectrons increases the probability of dynode photons and molecule ionization. The dynode photons are fast and the resulting signal appears just a few tens of nanoseconds after the photon-event, often hiding beneath that signal. The large mass of the ionized molecules lets them travel slower than the photoelectrons, hence producing electric pulses which appear hundreds of nanoseconds to microseconds after the photon-pulse.
Figure 2.4 shows the distribution of the PMT amplitudes with and without afterpulses.

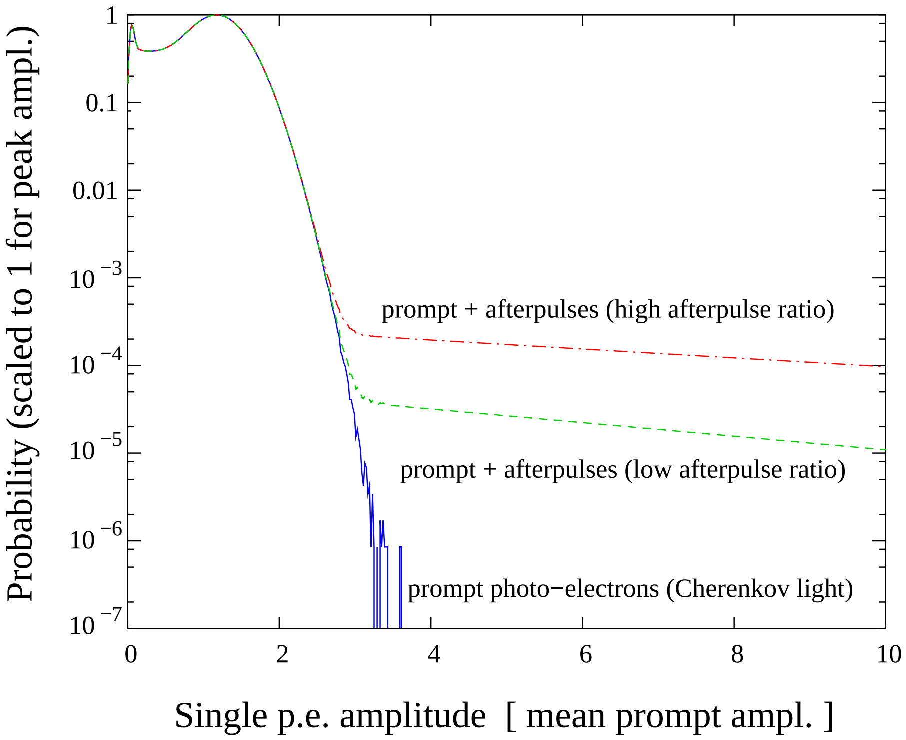

Figure 2.4: Simulated PMT amplitude distribution spectrum for single photo-electron signals (blue) and with afterpulsing for two different PMT types (red and green). The high signal probability below 1 pe results from photo-electrons missing the first dynode and hence being less amplified. Picture taken from [53].

The rates for AP with amplitudes above 4 pe are on the order of 0.005-0.8% for Cherenkov camera PMTs. Extensive studies on AP of CTA PMT candidates have been done by [54].

The dark current, the second source of 'noise' signals, comes from thermionic electron emission of the cathode and the first few dynodes, electrons released from dynodes through the electric field (field emission) hitting the PMT glass tube and causing emission of photons, leakage currents of the applied high voltage through electrode supports etc. and others. The dark current is the largest source of 'noise' with a rate of a few kHz. This noise can be neglected in Cherenkov astronomy since the night sky and other artificial light sources produce signal rates of $\mathcal{O}$(MHz) per PMT. Section 5.1.2 gives a more in-depth description of the statistics and the calibration of PMTs.

2.2.2 PMT candidates used in this work

PMTs from two manufacturers have been used in this work. The Photonis XP2960, used in all H.E.S.S. cameras, was first used in absence of a CTA PMT candidate. The PMT is an 8-dynode tube designed for use in an IACT. The CTA PMT candidate R11920 is specially designed for CTA by the company Hamamatsu and is still under development. Table 2.1 shows the most important parameters for these tubes.

Parameter	XP2960	R11920-100-01	R11920-100-05
Producer	Photonis	Hamamatsu	Hamamatsu
Type	Head-on	Head-on	Head-on
Diameter	29 mm (1 1/8")	38 mm (1.5")	38 mm (1.5")
Number of dynodes	8	8	8
Photocathode	Bi-alkali	Super bi-alkali	Super bi-alkali
Capacitance	5 pF	8 pF	4.5 pF
Voltage cathode-DY1	350 V	300 V	400 V
Transit time	23 ns	23 ns	23 ns
Transit time spread	not specified	1.3 ns	2.0 ns

Table 2.1: Comparison of some parameters for PMTs used in this work. The first version of the Hamamatsu R11920 (-01) has been further improved and optimized towards version -05, introducing slight changes in the geometrical dimensions, improving the afterpulse rate and the quantum efficiency, etc.

The PMT capacitance of the anode has the biggest impact on the readout electronics, since it defines, together with the load resistor, the analogue output bandwidth of the PMT and hence the signal decay time (see section 4.3.1).

2.2.3 Photodiode as an alternative photo-detector

Although most IACT cameras are assembled and work well with PMTs, efforts are ongoing towards using photodiodes as photo-detectors. The First G-APD Cherenkov Telescope (FACT) camera project on La Palma [55] [56] is a technical demonstrator camera with 1440 semiconductor pixels, mounted on the refurbished HEGRA CT3 telescope [57]. Such a multi-pixel photon counter (MPPC) has a rather small active area, on the order of some mm^2 and hosts up to 14000 single Geiger-mode avalanche photodiodes (GAPD) connected in parallel. A MPPC has the nice advantage that it easily survives bright light exposure yet being sensitive to single photon events. The single GAPD is operated as a reverse biased p-n junction with bias voltages of nearly 100 V. This bias voltage is above the breakdown threshold voltage to reach the Geiger-mode. A bias voltage below the breakdown voltage fully depletes a region within the p-n junction from all free charges and holes through its electric field.

A photon striking the fully depleted zone might create an electron-hole pair. The electron and hole are accelerated by the means of the electric field in opposite directions and create on their way further electron-hole pairs by ionization. This process generates an avalanche which is stopped by a quenching resistor, producing a signal which is somehow proportional to the number of incident photons. Operating the avalanche photodiode in Geiger-mode means increasing the electric field even further (over-depletion) and hence increasing the gain, making the diode sensitive to single photons. The pulse amplitude of the output current of a single GAPD with such high gains (10^5 to 10^6) remains the same, regardless of the number of detected photons. Adding up the output pulses of all GAPDs in an MMPC produces an almost discrete spectrum with nicely distinguishable photon-counts in Geiger-mode. This photon-counting ability and the robustness against excessive light exposure gives these detectors a big advantage over a PMT. Currently, a large effort is being put into the development of larger and more efficient MPPCs. More information can be found in [58].

2.3 Analogue signal path, buffering and signal processing

A Cherenkov flash provides up to several thousand photons imaged in only a few pixels, as discussed in section 1.5. However, it is reasonable to limit the detectable dynamic range of a single pixel to light pulses with <10000 photons at a time[4], since higher counts are extremely rare. This corresponds to about 4000 photoelectrons, assuming a PMT quantum efficiency of 40%. The resulting electric charge of the PMT is generally converted into a voltage pulse via a load resistor with usually <100 Ω. The PMT pulse can be amplified and shaped if needed, before it is digitized with the ADCs.

The large dynamic range of the signals and the necessity to resolve almost down to single photon events requires ADCs with likewise large dynamic ranges. Experience has shown that it is desirable to have between 10 and 20 least significant bits (LSB) per photoelectron for a good single pe resolution. Hence, an ADC with 16 bits (65536 LSBs) resolution would be needed to resolve signals with up to 4000 pe. Such ADCs are still rare on the market and are in any case expensive, very power hungry, and need a large pin-count of the subsequent processor.

Reducing the ADC's resolution to lets say 12 bits would result in a single pe resolution of only 1.3 LSBs. This is certainly not enough since electronics noise already contributs 1 to 2 LSBs. One solution to overcome this problem is to split the PMT signal into two signal paths and choose the amplification and the ADCs accordingly to achieve an overlapping dynamic ranges of the two paths (figure 2.5). A large overlap of the dynamic ranges allows intercalibration of the two signal paths. Since high photon-count events are more rare it makes sense to split the dynamic range asymetrically, resolving the small amplitude signals better than the large ones. A possible breakdown could then be up to 200 pe for one ADC and 20 to 4000 pe for the second ADC.

---

[4] A shower as seen by a single pixel lasts several tens to hundreds of nanoseconds. However, the largest portion of the Cherenkov pulse is concentrated within just a few nanoseconds and produces a PMT output signal that looks like a slightly broadened single photon PMT pulse.

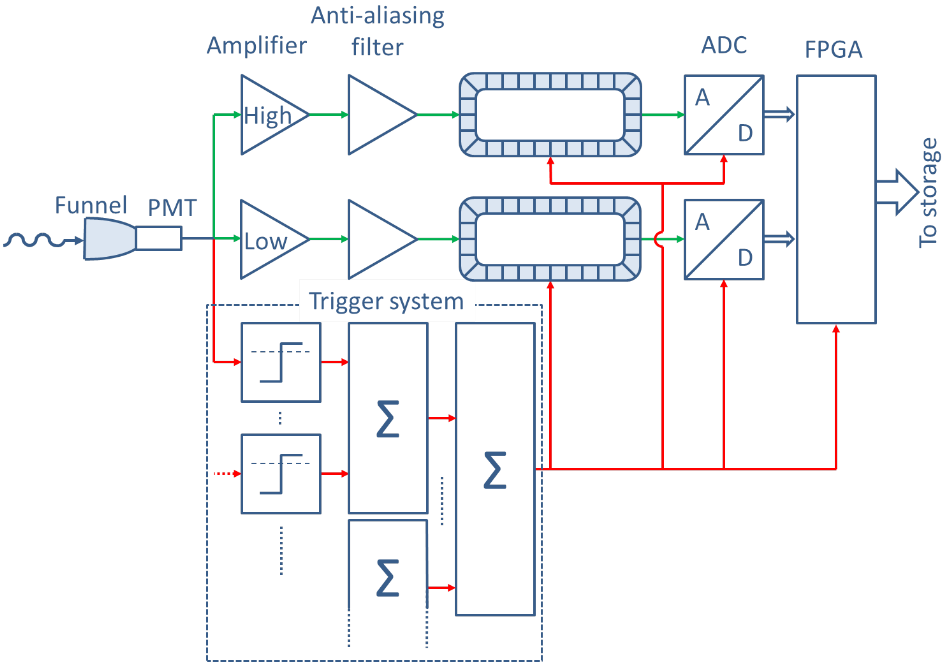

Figure 2.5: Possible design of the electronics of an IACT camera. The sketch shows a single pixel channel with all subsequent electronics stages. Green arrows indicate the analogue signal flow, red arrows indicate the trigger system and blue arrows indicate the digital data flow.

The small amplitude pulses need to be amplified to cover the whole input range of the ADC and hence this path is called high gain path. The large amplitudes in the second path often need to be attenuated to cover the ADC input range and the signal path is thus called the low gain signal path. With the signal split into two paths, the Cherenkov signal resolution can be maintained over the desired dynamic range and well available ADCs can be used for the signal digitization. A third branch of the PMT signal feeds the trigger unit, which is discussed in section 2.4.

Two more components are needed to complete the analogue signal path. That is, a anti-aliasing filter to limit the signal's bandwidth and the previously discussed buffer. The anti-aliasing filter can be realized with a low-pass filter and should cut off frequencies to meet the Nyquist requirement which relates the sampling rate of the ADC to the maximal allowed input frequency ($f_{sampling} > 2 \cdot f_{max}$). The factor 2 is often increased 2.5-3 since a low-pass filter has a roll-off of the cut off frequencies. The signals are now buffered before a trigger event initiates the digitization of the signals. Such a buffer for analogue signals can be realized as a ring buffer, also called ring sampler. A ring buffer is built of a series of capacitors. The analogue signal is sampled with a set rate, and each sample is stored separately in one of the capacitors. The sampling speed can reach up to several giga samples per second (GSps). A common ring sampler like the Domino Ring Sampler (DRS) from PSI [59] has sampling speeds of 0.2 to 6 GSps and 1024 sampling cells. Hence, a signal length of about 1 µs can be stored with a resolution of 1 ns. The DRS chip has 9 differential inputs and thus can serve up to four pixels or put in cascade serve one pixel with a buffer depth of 4096 sampling cells. A trigger event will stop the ring buffer writing and allow the sequential readout of the cells with a slow ADC $\mathcal{O}(30\,\mathrm{MSps})$. Such a system is used for example in the MAGIC-II telescope [60]. The H.E.S.S. telescopes also make use of ring sampler [61]. The drawback of having to stop the buffer during the readout is the introduction of dead time of a few microseconds resulting in a blind camera.

The digitized signals are fed to FPGAs for data compression and/or for grouping of the single pixel data to a complete data stream. This data stream is then sent via a fast link to the storage farm and there written to disc. The data stream for a camera trigger rate of $T = 10\,\mathrm{kHz} = 10\,\mu\mathrm{s}^{-1}$, $N = 2000$ pixels with a digitization rate of $S = 2\,\mathrm{GSps}$ at $R = 12\,\mathrm{bit}$ resolution per signal path and a readout window of $t = 80$ nanoseconds (corresponding to 160 samples) amounts to $2 \cdot T \cdot N \cdot S \cdot t \cdot R = 76.8\,\mathrm{Gbit/s} = 9.6\,\mathrm{GByte/s}$.

2.4 Camera trigger system

Gamma-ray events produce camera images with a certain shape, time and amplitude structure. This structure is not always clear enough, so images from non-gamma-ray events (background) may be mistaken as gamma-ray events. The trigger system of an IACT camera should be able to identify the image structure of a gamma-ray event (figure 1.23) and hence reject as many background events as possible. The time to analyze the image and make a trigger decision must fit the timing of the Cherenkov flash which is on the order of a few nanoseconds. The fast events thus exclude computational intensive pattern recognition algorithms, as for example used in compact digital cameras. Instead, smaller parts of the camera image are analyzed separately but simultaneously and the results are merged to a trigger decision. More precise analysis of the images, where also parameters like shower energy and direction are extracted, are done off line on computer farms using better and more sophisticated algorithms. For the

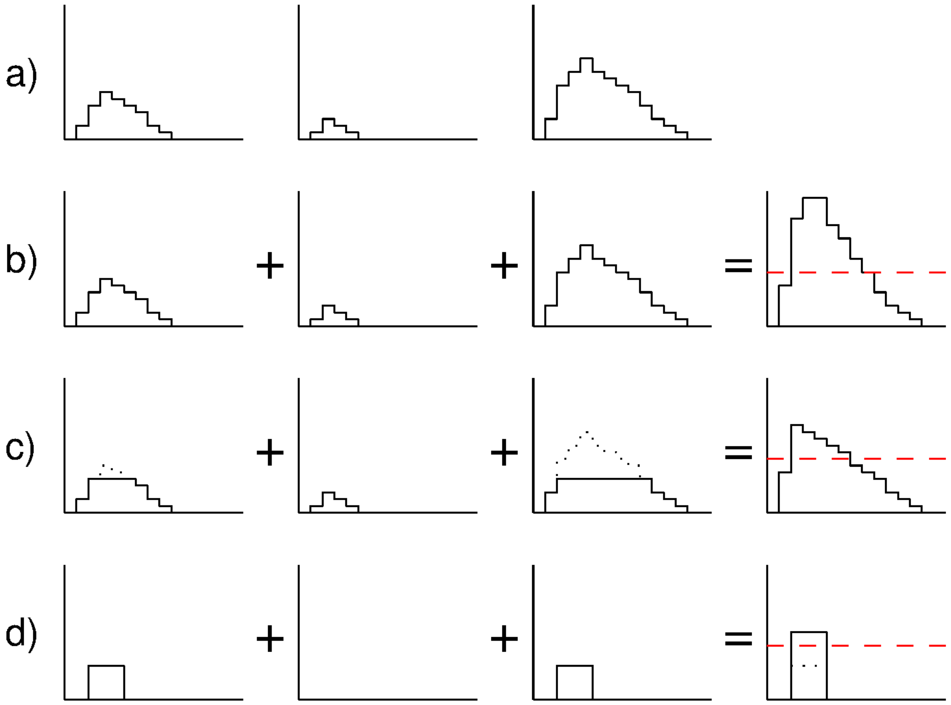

Figure 2.6: Principle of trigger classes shown with three digitized signals (a). b) sum of the three signals with following discriminator. c) The signals are clipped first before summed up. d) The logical majority class converts the signals into a logical state before summing up. The dashed red line on the right summed signal represents the discriminator and trigger threshold.

camera trigger, two main strategies (trigger classes) are used in current designs and are discussed in the following section.

2.4.1 Trigger classes

A trigger class represents a group of similar trigger algorithms. There are essentially three such classes used in current IACT cameras:

- sum and clipped sum
- logical majority.

The working principle of the trigger classes can be explained with three, analogue or digital, signals as shown in figure 2.6(a). The first trigger class, the sum (b), simply adds up all three signals (a). A discriminator produces a trigger signal as soon as the sum reaches a given threshold (red dashed line). The slightly modified clipped sum version, shown in (c), limits the

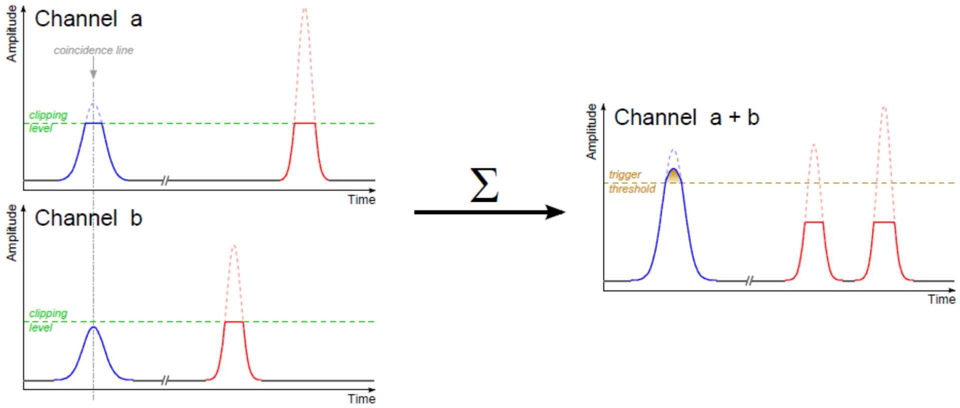

Figure 2.7: Two PMT output signals (blue) with afterpulses (red) running through a clipping sum trigger class. The signals are clipped first at the clipping level (green dashed line). The afterpulses do not reach the trigger threshold after the summing of the two signals a and b, since they are not correlated in time. Picture taken from [62].

signals first before adding them up and discriminating the result. The second class, the logical majority class shown in (d), converts each signal first into a logical state according to a given threshold before adding up the logical signals and discriminating them again. Both classes have their advantages and disadvantages.

The sum class is very sensitive to noise and outliers with large amplitudes (e.g. a star shining in a pixel). PMT afterpulses (section 2.2.1) in particular can spoil the performance of this class and force an increase of the discriminator's threshold. Trigger events due to afterpulses can be reduced by applying a short coincidence time window for the analyzed signals, since afterpulses appear long $\mathcal{O}(\mu s)$ after the main PMT pulses (figure 2.7). The clipped sum prevents large amplitudes to dominate the trigger decision and hence manages outliers and afterpulses much better. However, it is still sensitive to noise. The logical majority class is not very sensitive to noise and not as sensitive to outliers and afterpulses as the other two classes.

2.4.2 Single telescope trigger

The trigger classes described before can combine an arbitrary number of individual pixels in patches to generate a trigger event. The number of combined pixels in a patch, as well as the shape of the patch, have an influence on the performance of the trigger. Patches may also overlap to create a more homogeneous picture for the trigger. The combinations and possibilities are huge and mostly restricted by the trigger system hardware. Current IACTs like H.E.S.S., MAGIC, and VERITAS feed directly the analogue PMT signals into their trigger system as sketched before in figure 2.5. They have clipped sum (H.E.S.S.) and logical majority classes (MAGIC, VERITAS) implemented. These trigger systems are hard-wired and hence face the problematic of maintaining the timing of the signals and not being very flexible to changes of a class. A better solution would be to implement the trigger system after the digitization of the PMT signals, allowing for trigger classes being implemented in software and dealing with digitized data, as described later in chapter 4. The thresholds of the trigger should be adjusted such that the maximum trigger rate does not exceed the readout rate of the whole camera and storage system. This is usually in the order of 1-4 kHz.

2.4.3 Multi-telescope trigger

Trigger events of individual telescopes may also be combined to produce an inter-telescope trigger. This is useful if several telescopes observe the same source and possibly detect the same shower. A multi-telescope trigger will for example reject most muon events. A muon creates a ring image (see section 1.5.1 figure 1.23) that is not spread over several telescopes and hence does not cause a trigger. Hadronic induced events can also be rejected better with a multi-telescope trigger since their Cherenkov light pool is more inhomogeneous and the arrival time spread of the photons is larger than for gamma ray induced events.

Chapter 3

Concept for a fully digital camera

Current IACT camera systems use discriminators and comparators in a separate analogue signal path for the trigger and the analogue PMT signals are only digitized and readout after a trigger event occurred. The idea for a fully digital camera is hence a continuous digitization of the analogue signals. The digitized signals can subsequently be pre-processed and then fed into the trigger system. Using digital data for the trigger processing has many advantages compared to purely analogue system. The distribution of the signals happens without any signal loss and without any interdependence of the trigger and the signal readout system, as it is the case in an analogue circuit. A fully digital concept introduces also more flexibility in the integration of trigger classes, allowing for more complex trigger classes. Adjustment of the trigger or even changing the trigger class can be done in real-time and during operation of the camera.

The first step towards a fully digital camera concept is the evaluation of the minimal digitization speed needed to accomplish the physics requirements. This is done with a dedicated MC simulation and subsequently verified with measurements.

3.1 Validating the MC simulations

The first simulations for a fully digital camera have been carried out for a single pixel, consisting of a PMT, an amplifier, an anti-aliasing filter to limit the analogue bandwidth, an ADC, and a post-processing algorithm for the determination of parameters like amplitude and time resolution, linearity of the system, etc. The processing chain is shown in figure 3.1.

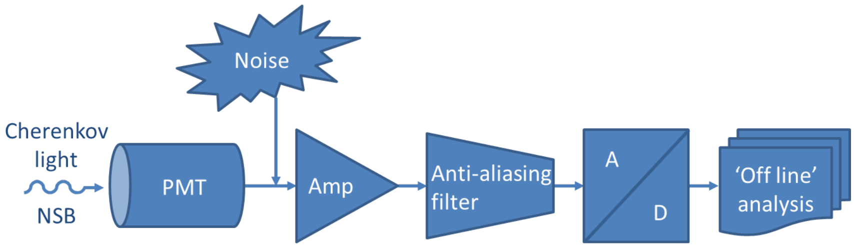

Figure 3.1: Simulation chain showing the individual components.

3.1.1 MC data production

Events (10^6 events) with NSB pulses and signal pulses are produced in a MC simulation designed and generated by T. Kihm at MPI-K Heidelberg [63]. This high resolution events can already be seen as an 'analogue' signal by the implemented functions. Each event is composed of a PMT signal, induced by a Cherenkov light pulse, superposed with NSB and electronics (white) noise as shown in figure 3.2.

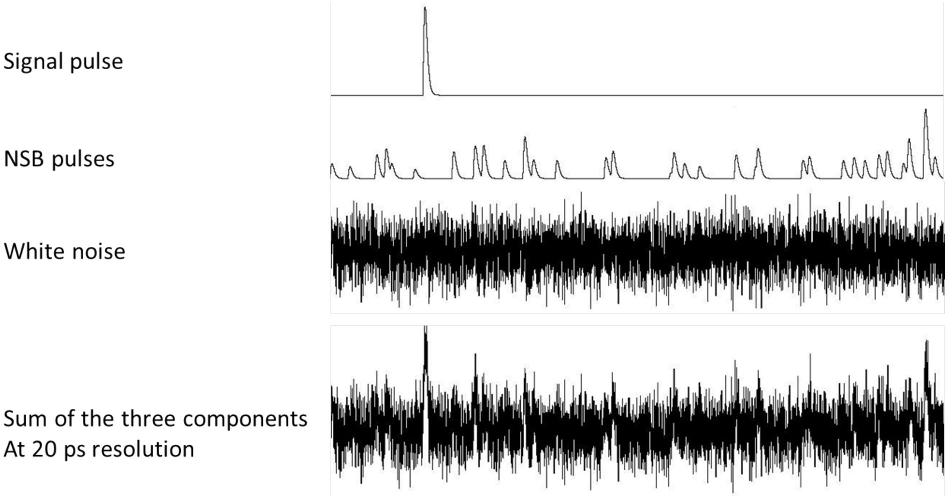

Figure 3.2: Composition of the PMT output signal for the design concept validation simulations. A single PMT pulse produced by N photons is used as signal. The night sky background is generated by uniformly distributed single photon events with a given rate (here 250 MHz). White noise, as produced by the electronics, is added last. The resolution of the simulated events is 20 ps, corresponding to a bandwidth of 50 GHz. The amplitude of the white noise decreases when the bandwidth is reduced to about a third of the sampling rate of 1 GSps and 250 MSps. Plot courtesy by T. Kihm, MPI-K Heidelberg.

The white noise appears to be very large in the figure, but is reduced substantially when the bandwidth of the whole signal is reduced.

Depending on the type of primary telescope mirror, the photons reaching the camera may or may not be isochronous. In the case of non-isochronicity, this is taken into account by smearing (convolve) the timing of the photons with a uniform distribution. A spherical mirror gives a good imaging ability but a non-isochronous timing. The time jitter introduced by the spherical mirror is about 1 ns for a mirror with 16 m focal length. A parabolic mirror is almost isochronous with a time jitter in the order of 50 ps for the same focal length but has a worse imaging ability. The current CTA mid-size telescope design tends to an intermediate setup with a time jitter of about 400 ps and an imaging ability between the spherical and the parabolic mirror.

The production of photoelectrons at the PMT photo-cathode is a statistical process [64] with an underlying Poisson distribution for the photons hitting the cathode and a purely binomial probability for the photoelectric effect to produce photoelectrons. The convolution of these two distributions results in a Poisson distribution with $\mu = QE \cdot N$ the mean number of produced photoelectrons defined as product of the quantum efficiency and the number, N, of photons hitting the cathode and $P_\mu(n)$ the probability for n photoelectrons emerging from the cathode (equation 3.1).

$$P_\mu(n) = \frac{\mu^n}{n!} e^{-\mu}. \tag{3.1}$$

A number of parameters are taken into account for the signal amplitude simulation. The production of secondary photons by secondary emission on the dynodes is a statistical process with underlying Poisson distribution. Experiences with PMTs for IACT telescopes have shown that a photoelectron produces in average six secondary electrons on the first dynode [65]. This is taken into account by the convolution of each photoelectron with a Poisson distribution of $\mu = 6$. The transit time spread (TTS) of the PMT is included with a Gaussian smearing of the PMT signal. The following values for the time parameters have been used in the simulation presented in this chapter: intermediate dish design with time jitter uniformly distributed with 1.4 ns, 1.5 ns rise time of the PMT signal and 0.5 ns TTS. The output signals convolved with the amplitude and time parameters described before are still delta-like pulses and have to be run through a 6-pole low pass filter with 6 dB/octave to simulate the output pulse shape of a real PMT.

The Night sky background (NSB) photons are added directly on the photocathode run through the 6-pole low pass filter. Next, electronics noise is added with 0.05 pe/ns, which is a bit less than the H.E.S.S. and MAGIC experience would suggest (~0.06 pe/ns). The white noise is bandwidth limited by the subsequent amplifier with an analogue bandwidth of 250 MHz. It is followed by an anti-aliasing filter, which reduces the bandwidth of the signal further to 10% of the sampling rate, or later for the comparison with measurements to about 1/3 of the sampling rate. This is realized with a 6-pole low pass filter with 6 dB/oct.

The analogue-to-digital conversion happens in two steps. The input signal is converted from a voltage to a digital value with respect to the input amplitude range of the ADC and its resolution by averaging the signal over half a clock cycle[1] and rounding the result to the nearest integer (quantization error) as shown in figure 3.3.

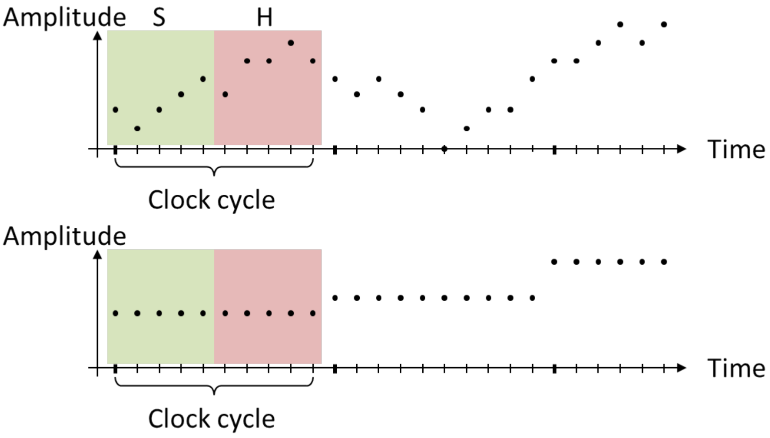

Figure 3.3: Resampling with a modeled ADC. The resolution of the data stays the same and only the signal bandwidth changes. The green region on the left denotes the sampling (S) time of the ADC, where the mean of the signal is build. All values in the hold (H) time are lost. The upper figure shows the data as simulated before running through the ADC and being resampled. The lower figure shows the data after the resampling and with the maintained step resolution.

This does not include the differential nonlinearities of the ADC, because they depend strongly on the used ADC and would have little effect for the presented simulations. A uniformly distributed phase shift between the ADC clock and the ’analogue’ signal is implemented instead of the ADC

---

[1] This value is chosen by experience, since most manufacturers do not publish this number. The number should lie between 30 and 50% of a clock cycle, where larger percentages give more accurate results of the digitized signals.

clock jitter. The program code allows the data to be digitized with different sampling rates to compare the performance.

3.1.2 Post-processing of the digitized data

The digitized data are post-processed before information such as amplitude and time of a signal are extracted. The optimal process for the most accurate information would be a fit of the discrete data to obtain an analogue-like signal. This, however, is not practical but can be approximated by shifting the discrete data into a higher frequency regime (up-sampling) and then smooth the data. This is done by interpolating and adding samples between two adjacent samples, hence increasing the resolution of the signal. The signal is subsequently smoothed with several simple moving average (SMA) filters, described as

$$\bar{x}_i = \frac{1}{w} \sum_{j=i-0.5w}^{w} x_j. \tag{3.2}$$

The mean value of the samples x_j in a window with width w is calculated for each sample x_i. Larger windows width create smoother curves then smaller widths. This post-processing improves the resolution of both the amplitude and the time as it mimics a fit to the sampled data. The up-sampled data is first smoothed with a SMA filter with a width of ± 3 samples. The resulting curve is referred to as 'adc samples average' in figure 3.4 and the time information is extracted from these data. An additional SMA filter with a width of ± 3 samples forms the 'shaped' signal. The 'deconvolved' signal includes an inverse low-pass filter, deconvolving the original PMT signal and the anti-aliasing filter. The figure shows all processing steps for a 1000 MSps ADC. One can see that the deconvolved signal fits the original signal fairly well.

3.1.3 Extraction of amplitude and time information

The post-processed data are analyzed and two main parameters, the amplitude of the Cherenkov signal and the arrival time of the photons, are extracted. A fast and efficient algorithm has been implemented for this purpose. Further improvements on the algorithm have been implemented in a later stage and will be discussed at the appropriate places. The amplitude of the Cherenkov signal can be extracted in many different ways. It can be the value at a fixed time with a constant offset to the trigger time or it is determined by looking for the maximum value in a time window

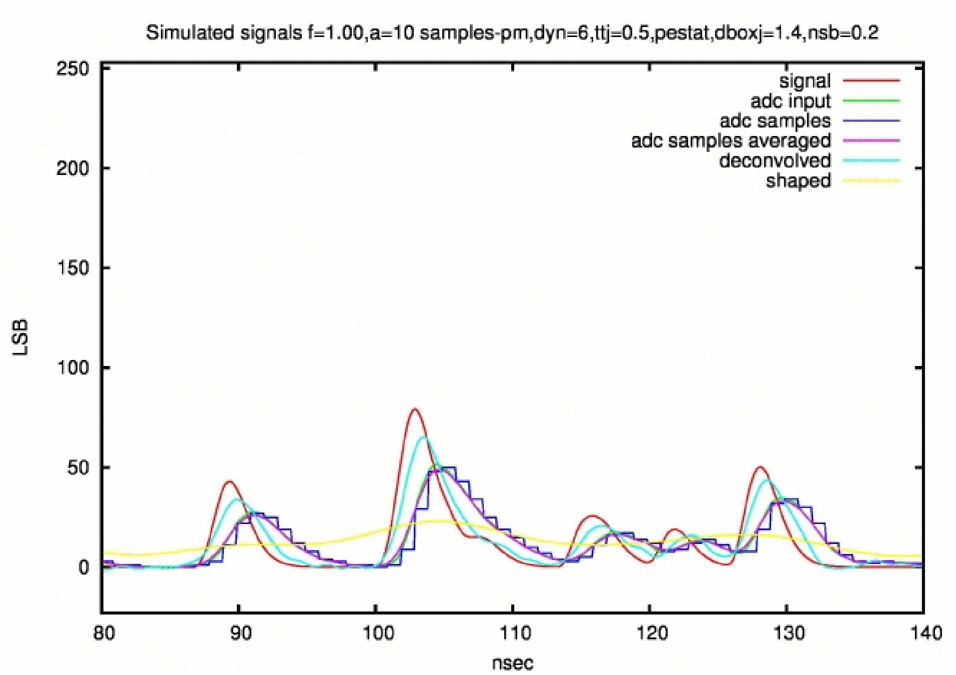

Figure 3.4: Post-processing steps of the 1000 MSps data. The shown event contains 200 MHz NSB only. The final result of the post-processing, the deconvolved (cyan) curve, deviates only marginally from the original data (red). Pictures courtesy by T. Kihm, taken from [63].

around the fixed time. A third option for the amplitude determination is the integrating around the maximum value found near the fixed time position. This integrated signal gives a better signal over noise behavior and reduces the impact of glitches and outliers. The arrival time is determined by the center of gravity (COG) of the integration window. The COG is calculated according to

$$COG = \frac{\langle \vec{w} \cdot \vec{y} \rangle}{\langle \vec{y} \rangle} \tag{3.3}$$

with $\vec{y}$ the amplitude values of the signal within the COG window and $\vec{w}$ the corresponding time position values. The $\langle\rangle$ brackets denote the arithmetic mean. The search window for the amplitude maximum used in the analysis presented in the next section is ±4 ns. The data have also been analyzed with a ±2 ns search window, but results were almost the same as with the fixed time amplitude determination. The signal noise is determined 50 ns before the signal pulse and its amplitude is calculated the same way as the signal amplitude. The absolute arrival time is of no relevance in a real system but should be referenced to a trigger time. For the simulation, the known arrival time of the Cherenkov photons is smeared with a Gaussian with $\sigma = 0.3$ ns to simulate the jitter of the photons hitting the PMT. This time is also used as the trigger moment.

3.1.4 First results

The first goal of the MC was to evaluate the lowest sampling rate for the ADCs that still allows a good performance of the camera. One figure of merit for a good camera performance is the instrumental resolution, which measures the overall resolution of a telescope involving the telescope mirror type and the light source statistics but assuming a perfect camera electronics (no PMT signal statistics, electronics noise, etc.). The results extracted from the MC simulation are shown in figure 3.5. The instrumental resolution is plotted against the sampling rate for a Davies Cotton telescope design. It shows the sampling-rate dependence for signals with amplitudes between 1 and 7 pe. The instrumental resolution between 250 and 1000 MSps is nearly flat, only worsening slightly below 250 MSps. A sampling rate of 250 MSps is hence a good choice for ADCs in a fully digital camera.

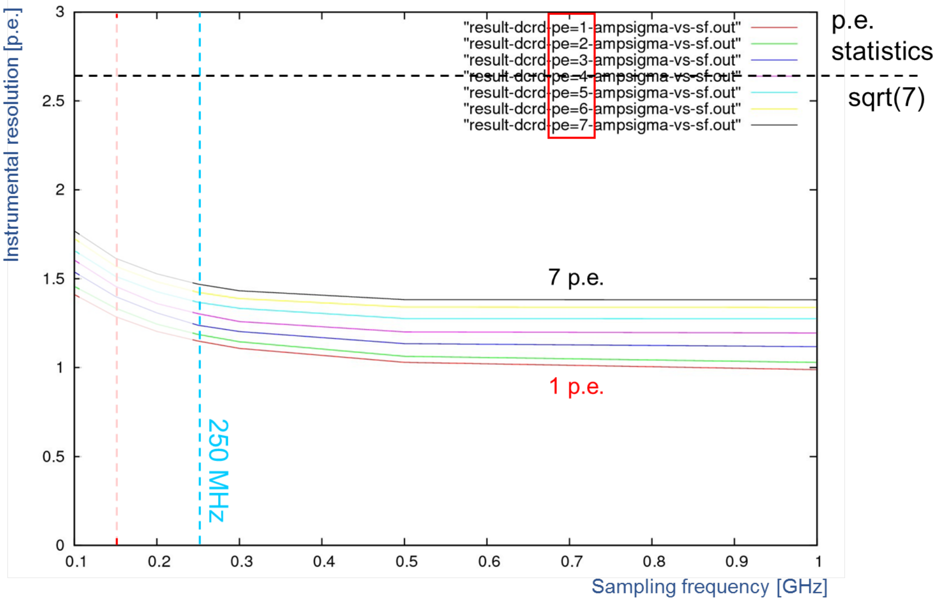

Figure 3.5: MC simulation for the instrumental resolution (no PMT statistics taken into account) of a Davies Cotton telescope for different sampling rates and fix PMT amplitudes of 1-7 pe. Plot courtesy by G. Hermann and T. Kihm, MPI-K Heidelberg.

The amplitude resolution ΔA, which takes the PMT statistics into account, is shown in figure 3.6 for the evaluation methods using deconvolution of the low-pass filter and signal shaping only for different sampling rates. ΔA is calculated as:

$$\Delta A[\%] = 100 \cdot \frac{\sqrt{\overline{s^2}}}{\bar{s} - \bar{b}} \tag{3.4}$$

with $\bar{s}$ and $\bar{b}$ the mean of the signal and background amplitudes and $\sqrt{\overline{s^2}}$ the root mean squared (RMS) of the signal. There is no significant difference between the evaluation with the deconvolved or the shaped data and between the different sampling rates. The determined time resolution shown in figure 3.7 performs better at lower light intensities for the deconvolved than for the shaped method. However, the time resolution is not significantly worse for the lower sampling rate of 250 MSps compared to the higher sampling rates shown in the plot.

3.1.5 Taking measurements

In order to verify the accuracy of the MC simulation, a series of measurements have been performed. The test setup for the measurements is shown

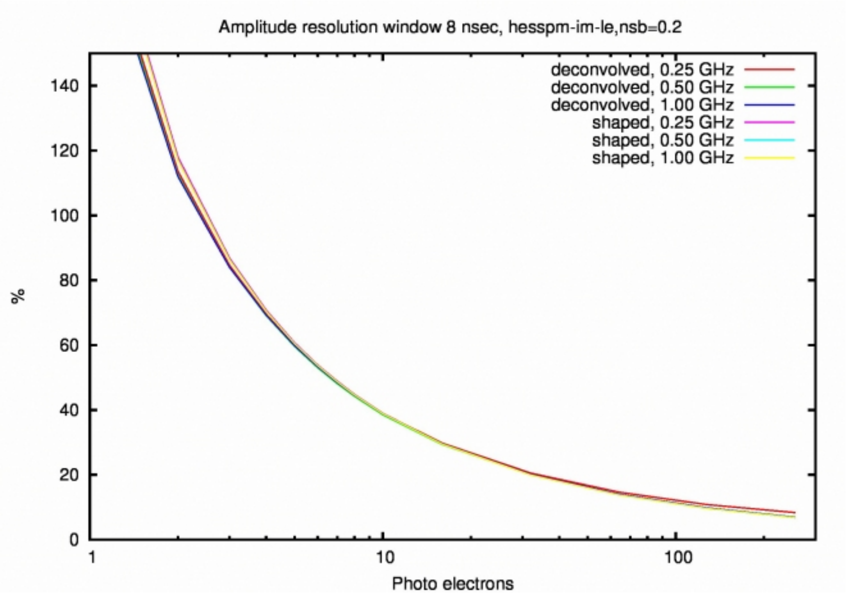

Figure 3.6: Amplitude resolution ΔA calculated with equation 3.4 for a H.E.S.S.-like PMT versus event signal amplitude with additional 200 MHz NSB. Shown are the two evaluation methods with deconvolved anti-aliasing filter and the shaped only. Additional results for 500 MSps sampling are also shown. Plot courtesy by T. Kihm.

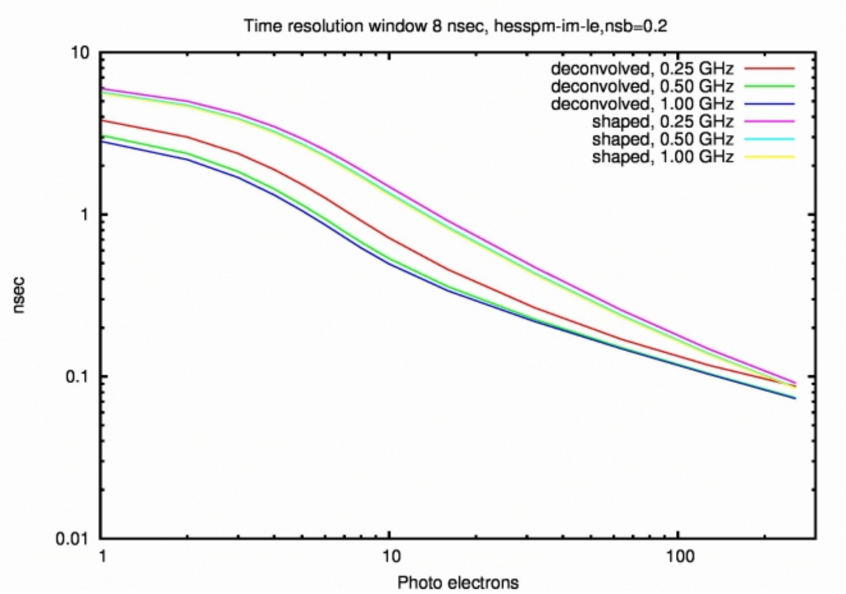

Figure 3.7: Time resolution for a H.E.S.S.-like PMT versus event signal amplitude with additional 200 MHz NSB. Shown are the two evaluation methods with deconvolved anti-aliasing filter and the shaped only. Additional results for 500 MSps sampling are also shown. Plot courtesy by T. Kihm.

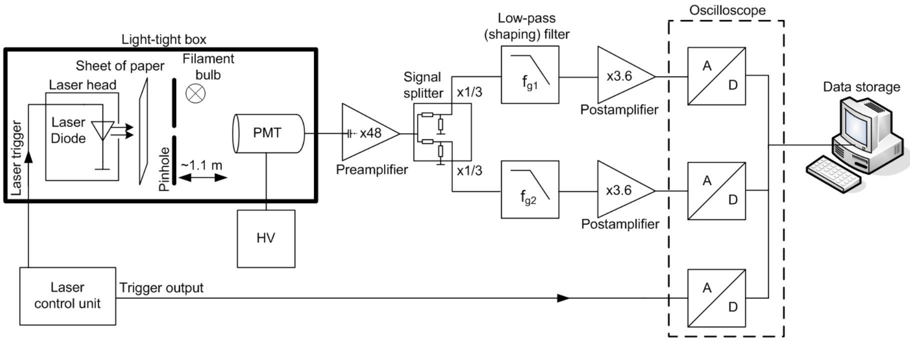

Figure 3.8: Setup for the measurement taking with a commercial oscilloscope for the signal digitization and a computer for data storage. The cutoff frequencies of the low pass filters are 80 and 230 MHz.

in figure 3.8. It consists of an adjustable blue laser diode simulating the Cherenkov light and a filament bulb[2] to produce NSB (see section 6.1). The single pixel chain starts with a Photonis XP2960 PMT, as used in the H.E.S.S. cameras, operated at -950 V, which corresponds to a PMT gain of about 10^5. The output pulse rise time of about 1.5 ns at -1400 V increases to roughly 2.2 ns at -950 V supply voltage (the applied PMT supply voltages for all presented measurements are always negative, even if not stated explicitely). The PMT is mounted inside a μ-metal shield in order to screen it from ambient magnetic fields. A pinhole of about 1 mm diameter is placed in front of the PMT to reduce the transit time differences due to photon-hits at different locations on the cathode[3]. The pinhole is removed for the later measurements since the influence of the transit time difference is almost not noticable. The intrinsic time jitter of the laser is on the order of a few hundreds of picoseconds.

The PMT is directly attached to a high gain, high speed RF amplifier stage to maintain a large bandwidth of the analogue signal. The stage uses a MMIC (Monolithic Microwave Integrated Circuit) amplifier with an analogue bandwidth of about 3 GHz at 16 dB gain and a subsequent ZFL-1000 amplifier from Mini-Circuits with 1 GHz analogue bandwidth at 18 dB gain resulting in a total gain of 48. Both amplifiers are AC-coupled and 50 Ω terminated. The amplified signal is split with a resistive Owen splitter [66]

---

[2] Later measurements with more than one PMT have revealed that a filament bulb is not suitable to be used for the NSB production since its spectrum lies in a regime where the quantum efficiency of the PMTs are very low and vary up to 100%. The method is acceptable for single PMT measurements.

[3] The transit time difference for photons hitting the photocathode in the center and 18 mm off-center is about 0.8 ns.

with 10 dB power attenuation and 19 dB channel isolation. Subsequent anti-aliasing low pass filters in each signal path with cutoff frequencies of ~1/3 of the sampling rates under examination (250 and 1000 MSps) are built as LCLCL Bessel 5th order filters (appendix A.1). The bandwidth-limited signals of the low-pass filters are amplified a last time with a NIM ORTEC AN302/N amplifier with a gain of four, to allow for a higher sensitivity setting at the oscilloscope and hence reducing the scope's noise contribution.
A LeCroy Wavepro 950 scope with integrated GPIB interface is used for digitization and data acquisition. Its analogue bandwidth is 1 GHz and the sampling rate for all channels is chosen to be 2 GSps. The waveforms are read out via GPIB with a MATLAB [67] program, which also sets all scope settings each time a new run is started. The data of 1000 measurements of the trigger signal, coming from the laser control unit (see section 6.1.1), and the two PMT signals are saved in a single file in MATLAB's binary format.

Signals coming from the PMT have rather small amplitudes of a few mV compared to the large trigger signal of the laser control unit (slope times of 380 ps and 1.1 V amplitude). A crosstalk of the trigger signal to the PMT signal could occur and introduce unwanted noise. The crosstalk behavior was double-checked by summing up 1000 measurements and analyzing the resulting curve for features. Figure 3.9(b) shows the sum of one run of measurements of a 5 pe pulse event from the 80 MHz low pass channel. A possible trigger crosstalk would appear as a bump on the left side of the signal peak, since the two signals are delayed in time. No crosstalk is visible, but an oscillation, which is not visible in a single measurement (figure 3.9(a)), appears right after the signal peak. This oscillation comes from a miss-termination of the 80 MHz low pass filter to 50 Ω due to the chosen component values. It does not appear in the 230 MHz channel, which filter component values are closer to the calculated ones and hence meet the 50 Ω termination.

3.1.6 Analysis of the measurements

The measured data with a resolution of 500 ps is resampled off line down to 1 GSps and 250 MSps. The same analysis algorithms, as described in section 3.1.2 and 3.1.3 are used thereafter with slightly adapted parameters for the simple moving average filter widths and the amplitude search window width to analyze and compare the measured data with the MC data.

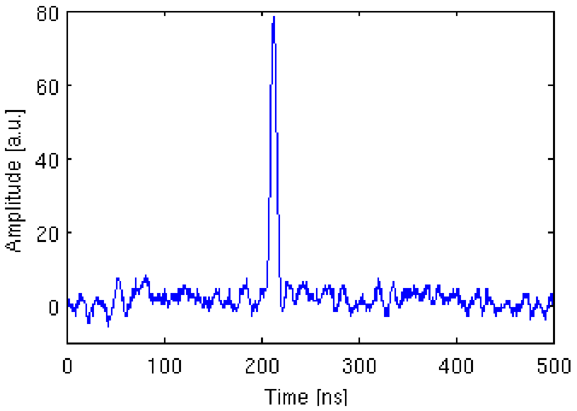

(a) A single 5 pe event measured at the 80 MHz low pass filter channel.

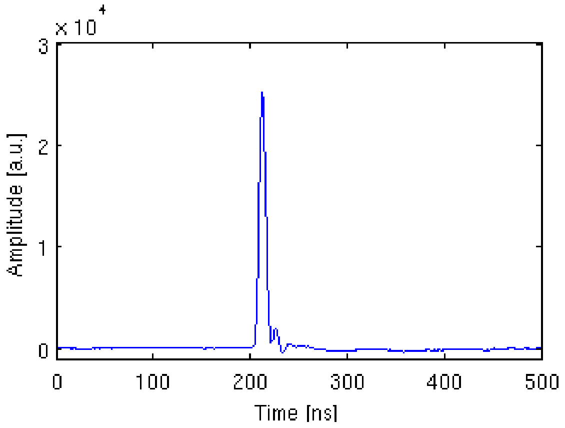

(b) Sum of 1000 5 pe events measured at the 80 MHz channel. No evidence for trigger signal crosstalk at the left side of the signal peak is visible. The oscillation right after the signal peak comes from a badly terminated low pass filter.

Figure 3.9: Trigger crosstalk check.

The first SMA filter width is changed to 8 samples of the 500 ps resolution for the 250 MSps and 2 samples for the 1 GSps data. The other SMA filter widths are changed to 16 and 4 samples. The overall smoothing of a 250 MSps signal without amplitude correction is shown in figure 3.10(a).

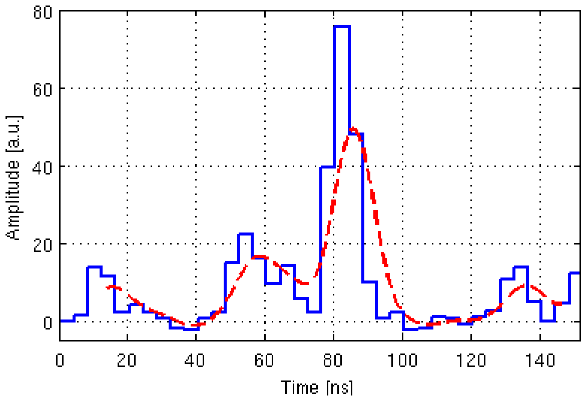

(a) Example of a digitized event before (blue solid line) and after (red dashed line) passing the post-processing.

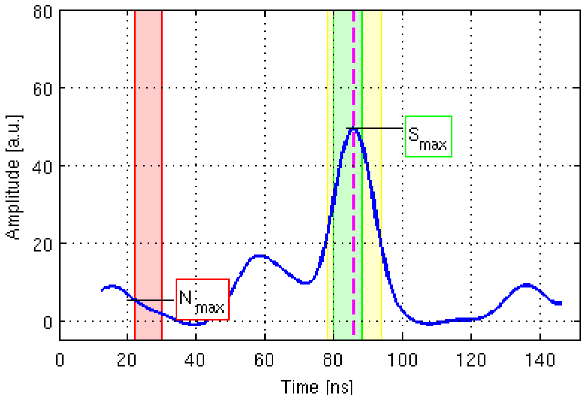

(b) Search windows of ±4 ns width for signal S_{max} (green, right) and noise N_{max} (red, left) amplitude determination and the wider ±8 ns window (yellow, right) centered around the signal maximum for the COG calculation. The magenta dashed line shows the computed time position of the maximum of the signal.

Figure 3.10: Signal smoothing with subsequent amplitude and time determination.

The amplitude of the signal is obtained by the maximum in a ±4 ns window around the trigger time. No amplitude integration is applied for this analysis. The time information is extracted by the COG of the signal region with a window width of ±8 ns centered around the maximum (see figure 3.10(b)). The noise and NSB amplitude (not the baseline amplitude) is calculated with the same method as the signal amplitude (maximum in a ±4 ns window in a region on the left side of the signal).

3.1.7 Adaptation of MC parameters

The MC simulations discussed in section 3.1.1 are adapted to the measurements by taking into account some the measured parameters for the NSB or the PMT characteristics. Some of the parameters could not be measured and are estimated by experience. The main parameters are shown in table 3.1. The PMT (Photonis XP2960) and the load resistor define the bandwidth of the measured pulses and the bandwidth is determined by the measured pulse rise time of about 2 ns at 950 V. The PMT transit time difference, not to be mistaken with the TTS, is the difference in timing for photons hitting the photo-cathode in the center or 18 mm off-center and is estimated by assuming a uniform distribution with 3 ns width resulting in a deviation with the square root of the variance $\sigma_{TTS} = 3\,\text{ns}/\sqrt{12}$ (datasheet: 800 ps).

Parameter	Source	Value
PMT + load resistor bandwidth	Measured	70 MHz
PMT transit time difference	Estimated	870 ps
Electronics noise	Measured	0.05 pe/ns
Time jitter between light pulses	Estimated	0.5 ns
Mean photon pulse amplitude	Measured	4.8 pe
NSB rate	Measured	0-455 MHz ±5-8%

Table 3.1: Main parameters determined by measurements or estimated entering the MC simulation. Detailed explanation of each parameter can be found in the text.

The noise contribution is determined by adjusting the simulated noise such that it fits the measured noise distribution. This value is used for both the 250 and 1000 MSps data. The time jitter between laser-light pulses is estimated assuming a Gauss distribution. The mean photon pulse amplitude is determined with histograms of single photoelectron measurements and 5 pe measurements.

A good method to estimate the NSB rate is to measure the DC voltage with a µV-meter directly at the PMT output, since the charge of the PMT, integrated over a given time interval, is linearly proportional to the NSB rate. This is true as long as no nonlinearities of the PMT come into play, which is certainly true for such low light yields. A Keithley 2001 multimeter with a measurement speed (integration time) of 20 ms and an integrated moving average over 10 measurements is used. The DC values shown in table 3.2 are obtained by the mean of the two DC values before and after each run of 1000 measurements.

DC value [μV]	NSB frequency [MHz]
1.6 ± 0.2	0
-6.2 ± 1.9	10
-35.0 ± 1.5	50
-80.6 ± 1.0	110
-332.0 ± 22.0	455

Table 3.2: Measured PMT DC values at different NSB frequencies.

The corresponding NSB rates are difficult to estimate and hence need two independent steps. The DC level of a completely darkened PMT gives the first measurement in figure 3.11.

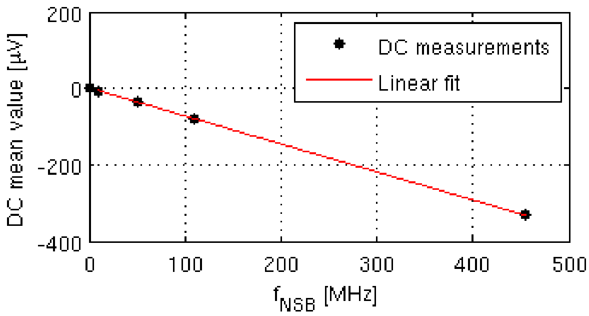

Figure 3.11: The figure shows the expected linear dependency of the PMT's DC voltage and the NSB frequency.

The filament bulb is then adjusted such that the rate can estimated by counting the events on the scope's screen. This produces the measurements at ~10 and ~50 MHz NSB. A forth measurement with higher rates is taken and compared to the results of the simulation with the NSB rate parameter changed for matching the measurement (455 MHz NSB). A linear fit (fit: $-0.73 \cdot f_{NSB} + 1.45$) through the four points is performed. To crosscheck the fit, a NSB rate is chosen from the fit (110 MHz NSB) and the bulb adjusted to produce the according DC value. The measurement is again double-checked with the simulation, now adjusted to 110 MHz NSB. The comparison of the measurements with the simulation shows a good agreement with a discrepancy of 5-8%. The first two measurements of 10 and 50 MHz NSB have also been double-checked and confirmed with the simulation.

3.1.8 Comparison of measurements with MC simulations

Four data sets are available for the comparison of the MC and the measured data. The MC data sets have a resolution of 20 ps and bandwidths of 80 and 250 MHz for sampling rates of 250 MSps and 1 GSps, respectively. The measured data have 500 ps resolution at 80 and 230 MHz[4] bandwidth. The bandwidths are ~1/3 of the sampling rates of 250 and 1000 MSps, as required to avoid Nyquist aliasing. The data sets are processed with the same algorithm shown in figure 3.12.

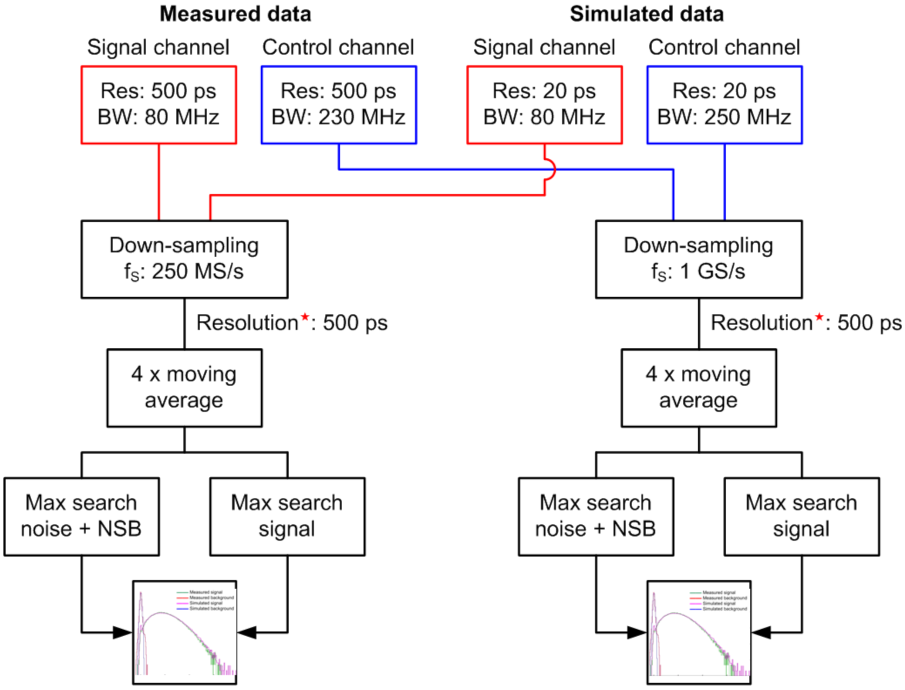

Figure 3.12: Flow chart of the algorithm to convert the high-resolution signals into 250 MSps and 1 GSps signals and to analyze the signal and noise amplitudes of the events. The output of the analyzed events is plotted in histograms for a comparison of measurements and simulation. The term signal channel corresponds to the 250 MSps ADC path and the control channel to the 1 GSps ADC path.

---

[4] The available components for the Bessel low pass filter lead to an actual bandwidth of 230 MHz. However, the effect on the comparison with the simulated 250 MHz bandwidth is negligible.

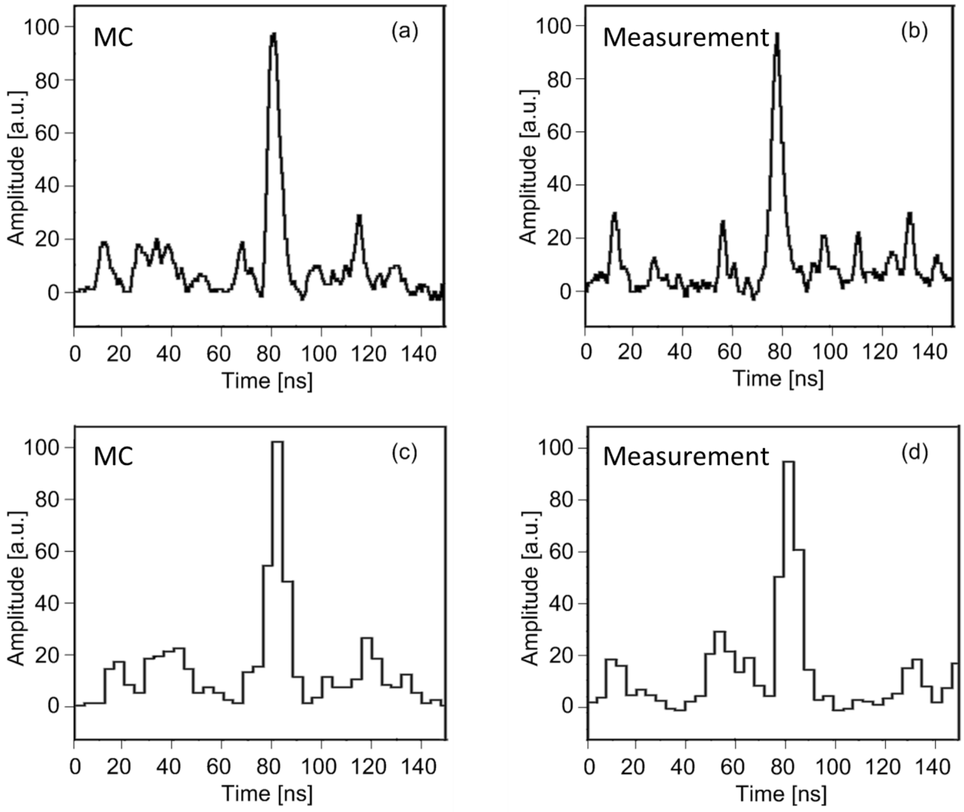

Figure 3.13: Example of a generic simulated and measured event with a 4.8 pe signal peak and 115 MHz NSB. The simulated (a) and measured (b) event at 2 GSps are shown on top. Bottom plots show the resampled events at 250 MSps for the simulated (c) and the measured (d) event.

For computational reasons, the MC data resolution of 20 ps is reduced to 500 ps after the resampling with the ADC. Figure 3.13 shows a generic simulated and measured event before and after the resampling down to 250 MSps.

Reconstruction analysis

The amplitude information for the noise and the signal extracted with the algorithms described above are plotted in a histogram for both simulated and measured data. The comparison of the histograms reveals possible differences between the simulations and the measurements. Figure 3.14 shows this comparison for signal and noise amplitudes of events with no NSB and a 4.8 pe signal at 250 MSps sampling rate. The two noise peaks on the left side (also called background) in the histogram show the amplitudes

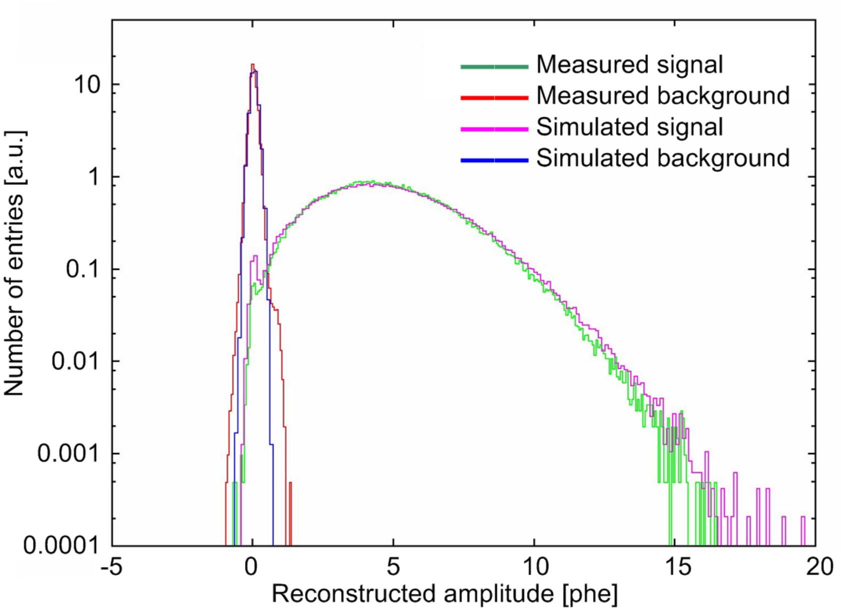

Figure 3.14: Histogram showing the amplitudes of the signal and of the noise determined in the search windows. The ADC sampling rate is 250 MSps. The measured and simulated data contain a signal pulse of about 4.8 pe, but no NSB. The wider noise peak of the measurement is due to pick-up noise.

determined in the noise window. Noise, which is probably picked-up over the PMT leads, broadens the noise peak of the measured events. The wide signal bump shows the signal amplitudes with a mean of 4.8 pe. The width of the signal bump at FWHM corresponds to the amplitude resolution and results the same for measured and simulated data. The amplitude resolution and the instrumental resolution, mention at the beginning of this chapter, describe different resolutions. The figures 3.15 to 3.22 show the comparison of the amplitude determination for simulated and measured data with a 4.8 pe signal pulse, 0, 50, 115, and 455 MHz NSB, and sampling rates of 250 MSps and 1 GSps.

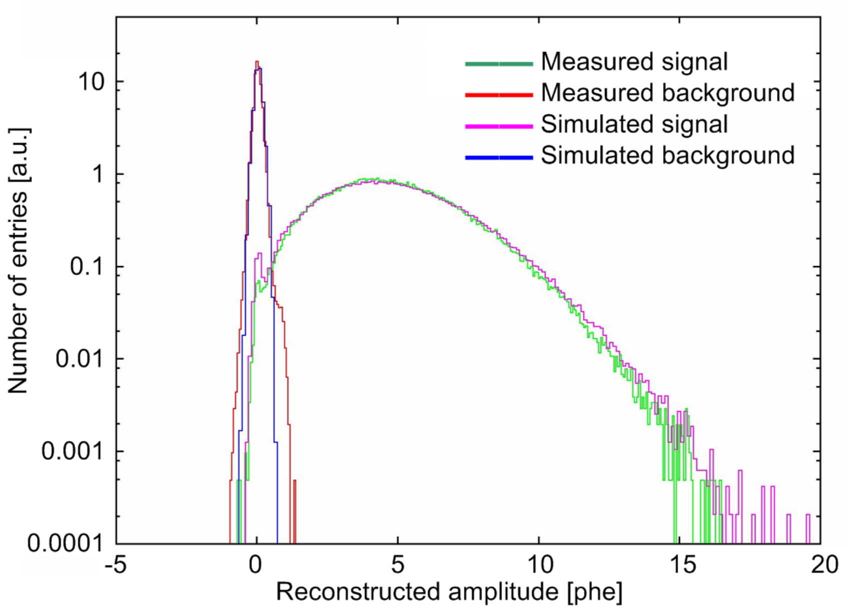

Figure 3.15: Amplitude histogram for a 4.8 pe signal and 0 MHz NSB at 250 MSps.

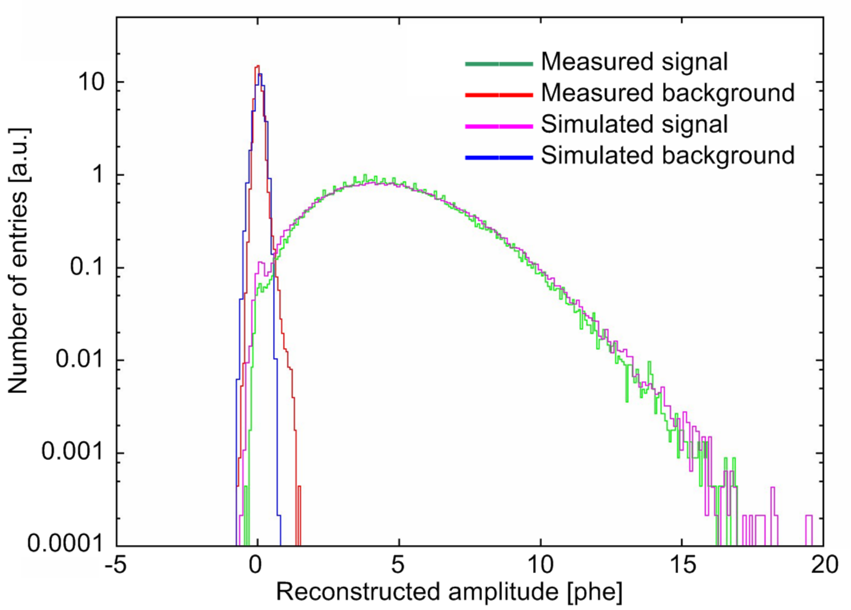

Figure 3.16: Amplitude histogram for a 4.8 pe signal and 0 MHz NSB at 1 GSps.

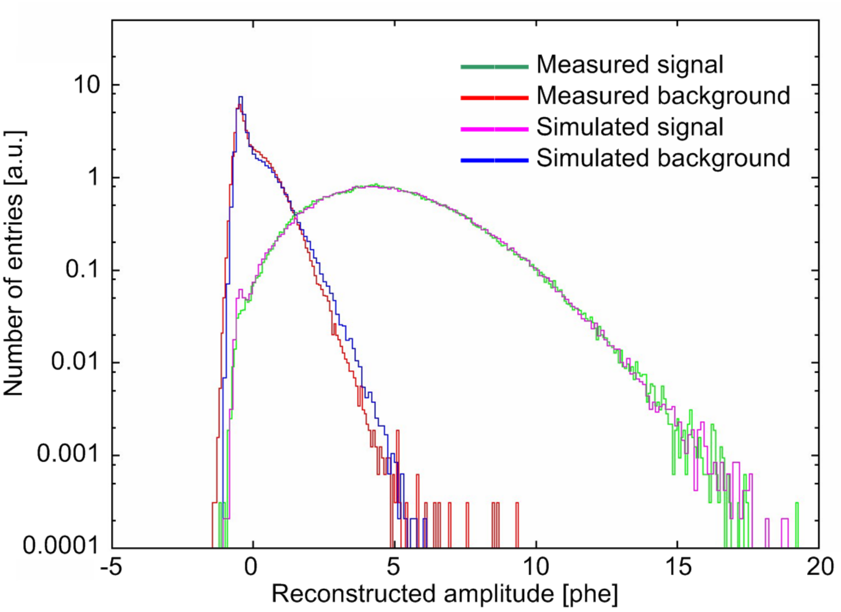

Figure 3.17: Amplitude histogram for a 4.8 pe signal and 50 MHz NSB at 250 MSps.

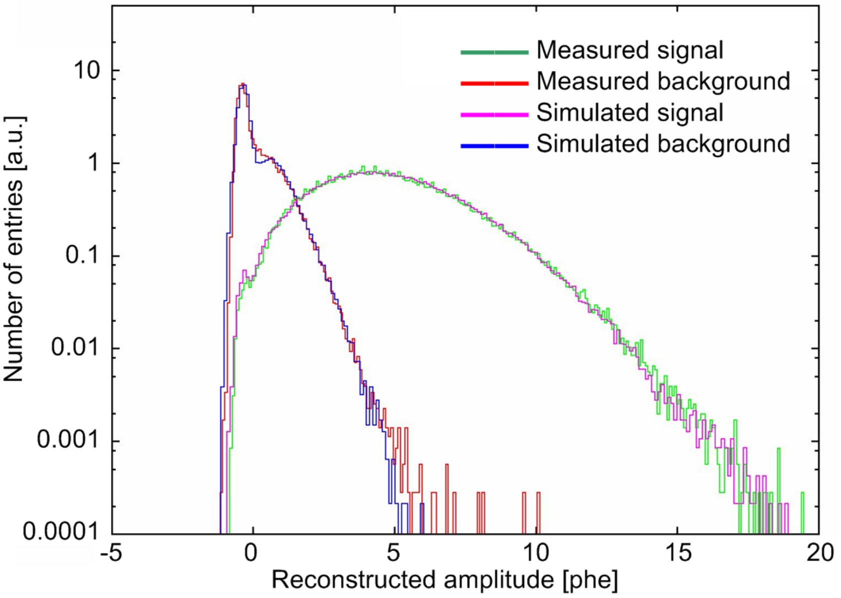

Figure 3.18: Amplitude histogram for a 4.8 pe signal and 50 MHz NSB at 1 GSps.

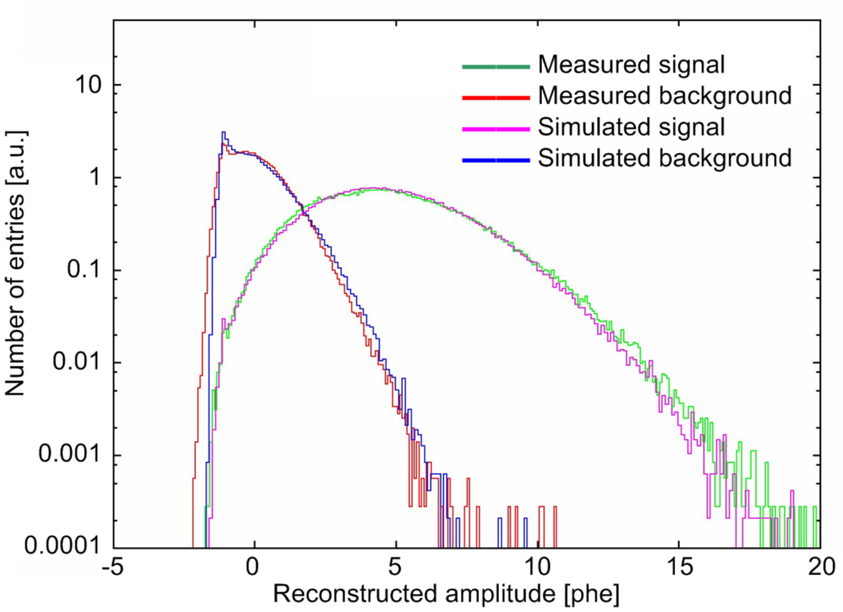

Figure 3.19: Amplitude histogram for a 4.8 pe signal and 115 MHz NSB at 250 MSps.

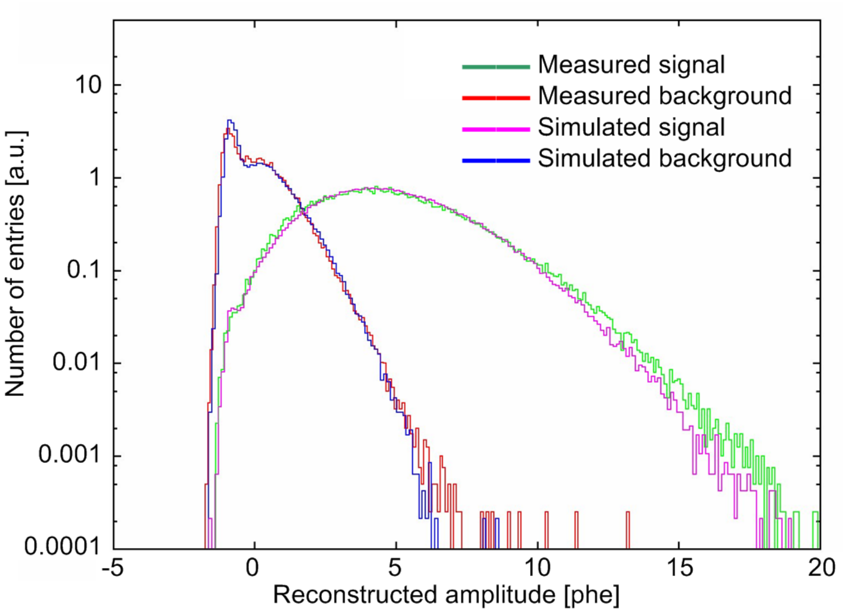

Figure 3.20: Amplitude histogram for a 4.8 pe signal and 115 MHz NSB at 1 GSps.

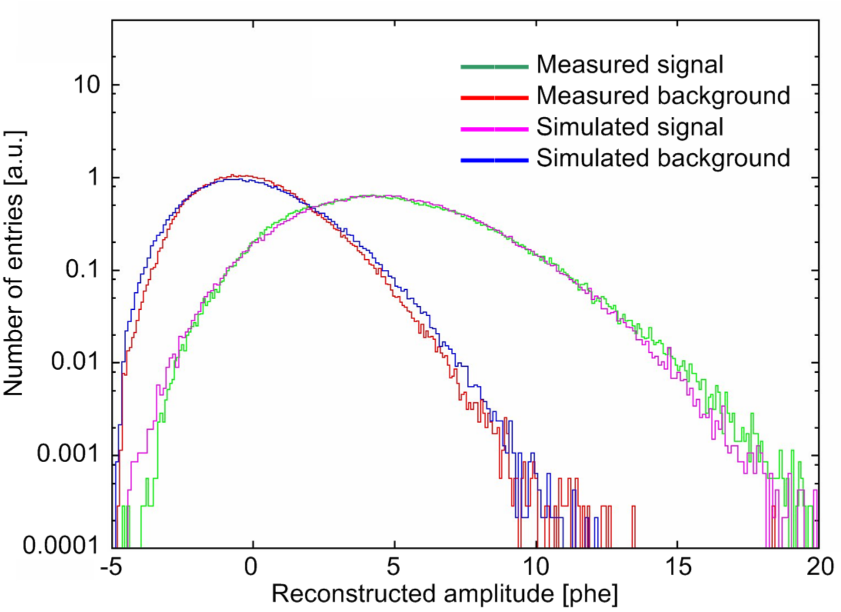

Figure 3.21: Amplitude histogram for a 4.8 pe signal and 455 MHz NSB at 250 MSps.

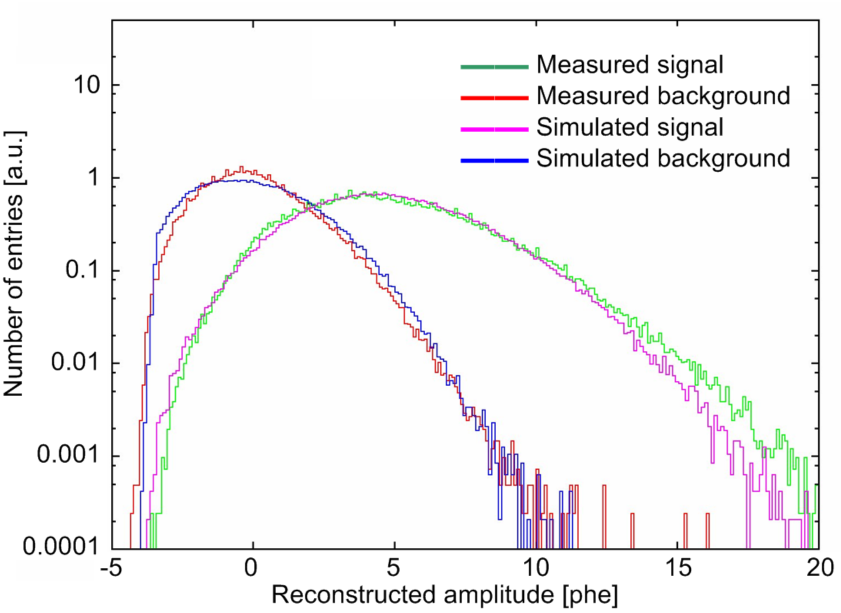

Figure 3.22: Amplitude histogram for a 4.8 pe signal and 455 MHz NSB at 1 GSps.

3.2 Conclusion for the fully digital camera concept

The comparison of the simulated and measured data has revealed no show stoppers for a fully digital camera with a sampling rate ADC of 250 MSps. Amplitude and time accuracy differ in the worst case by few percent for the amplitude resolution and ~15% for the time resolution when compared with the fast ADCs. The comparison also shows that the simulations are understood and reflect the reality very well. These conclusions have lead to the decision of building a first demonstrator board with the ADCs and FPGA described previously. The next chapters describe the hardware, developed to test the concept, and discuss measurements taken with this hardware.

Chapter 4

Implementation of FlashCam

The simulations of section 3.1 show that it is possible to use ADCs with sampling rates of 250 MSps, and to achieve almost to same performance in the reconstruction of the amplitude and time information of a Cherenkov light pulse as a system with faster ADCs. The continuous digitization of the signals, together with a mechanically separated and modular design of the photo-detector electronics form the basic concept of the FlashCam project, the first fully digital IACT camera [68].

4.1 FlashCam: the basic concept

The concept of FlashCam introduces, besides the continuous signal digitization, a single signal path concept per pixel, as indicated in figure 4.1.
The single signal path replaces the dual signal path used to cover the large dynamic range of the PMT signals. This is made possible by using analogue circuits with nonlinear transfer characteristics. Such circuits are very difficult to calibrate, especially when used in large numbers. This is certainly a good reason why there are no such circuits implemented in IACT cameras and why the dual signal path with a split dynamic range is still the favorite of the designs. FlashCam introduces a combined signal transfer characteristics with a linear regime for low amplitude signals up to about 10% of the full range and a nonlinear regime for the high amplitude signals, where the resolution specifications are a bit looser. How such a circuit can be designed and how the analogue signals are transfered to the digitization electronics is topic of the next sections. The analogue signals arrive at the digitization electronics and are run through anti-aliasing filters to reduce their bandwidth. ADCs sample the signal with 250 MSps and send the data to the FPGA. The digitized data is stored in ring buffers in the FPGA memory, and

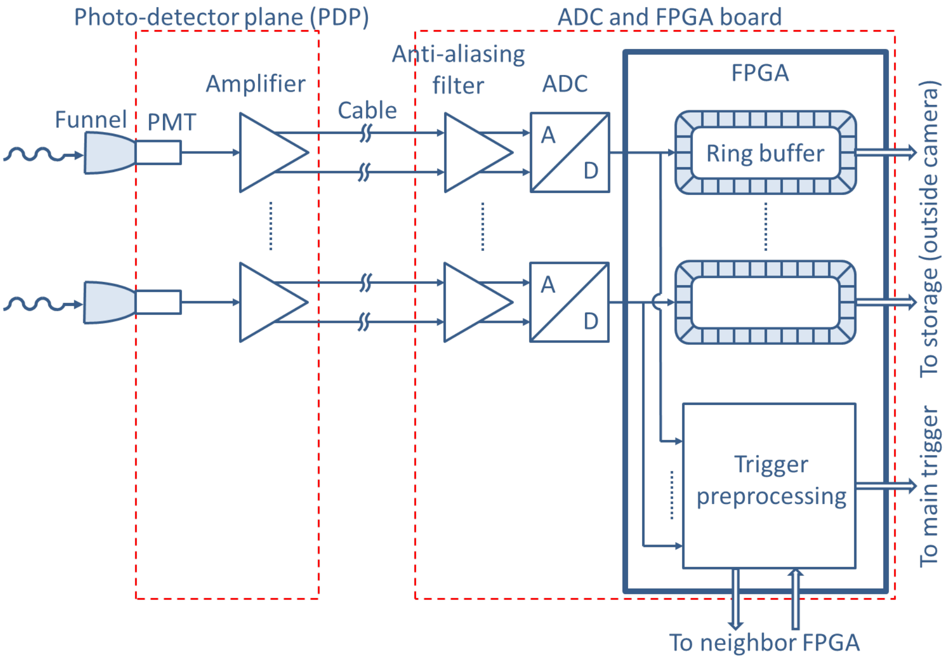

Figure 4.1: Sketch of the FlashCam camera concept showing the photo-detector plane on the left and a digitization board on the right. The photo-detector plane contains the photo-detector and the nonlinear signal amplifiers. The analogue signals are transfered with CAT5/6 cables to the ADCs and the digitized data are split in the FPGA and fed into a storage ring and into a trigger pre-processing unit for bandwidth reduction. The trigger data are subsequently sent to the main trigger system.

simultaneously branched to a preprocessing trigger unit inside the FPGA. This unit makes the implementation of trigger classes very flexible, since the trigger classes are implemented in software and can hence be changed at any time almost on the fly. The implemented trigger class can make use of the whole pixel information, setting several thresholds, applying different integration windows simultaneously, combine almost every number of pixels in any patch shape etc. New trigger ideas may be implemented later on without the need of changing any hardware of the camera, simply by changing software.
The amount of data fed with 250 MSps to a trigger system is large and hence should be reduced for a fast calculation of a trigger decision. The data stream of the trigger path is processed in the FPGA to reduce the bandwidth of the data, before the data are sent to the trigger system.

Figure 4.2 shows a sketch of the overall concept of FlashCam.

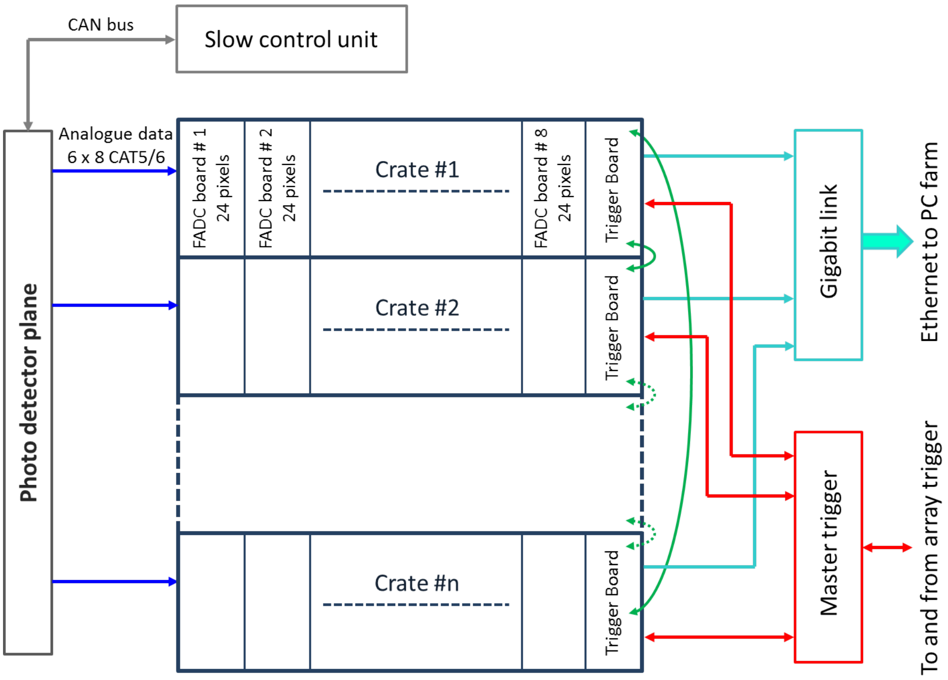

Figure 4.2: Sketch of the FlashCam concept with the photo-detector plane attached to the digitization electronics via CAT5/6 cables (blue arrows) and the digitization electronics mounted in crates. The PDP boards are slow-controlled via CAN bus (gray arrows). Each crate shares the trigger data for adjacent pixels with the neighboring crate (green arrows). The compressed and patched trigger data are sent to the master trigger, which also delivers the clock and a trigger event signal to all boards (red arrows). The triggered pixel data are sent via Gigabit-link to the computer farm (light blue).

The photo-detector plane (PDP) is physically separated from the digitization electronics. It hosts the PMTs, the amplifiers, the high voltage (HV) generation for the PMTs and the slow control for the amplifier gain and HV settings. The analogue signals are transfered over CAT5/6 cables, each cable transferring the signals of four pixels pseudo-differentially[1] over the

---

[1] A signal can be transfered over two wires in three different ways: the single-ended signaling uses one wire for the ground and the other for the signal. The differential transmission, also called symmetric transmission, transfers the signal and an inverted copy of it each over one wire. Noise that is picked up by the two wires hence cancels itself in the receiver. The intermediate signal transmission, called pseudo-differential, has no inverted signal but instead sends a virtual ground, for example a 50Ω resistor connected between ground and the wire, allowing both wire potentials to change simultaneously while picking up noise.

four twisted pairs (more on cable types and lengths is discussed in section 4.6), to digitization boards. Each board hosts 24 ADCs connected to a single FPGA. Up to eight of such boards are used in a crate together with a trigger card. A FPGA combines a number of pixels into patches according to the implemented class (for example sum of clipped signals), reduces the bandwidth of the signal and sends the patch information to the trigger card. A number of patches may be combined there to possibly generate a positive trigger event. Trigger boards in different crates share information via a high-speed bus. The trigger states of all trigger cards are sent and collected with a master trigger card. The master trigger card evaluates the collected trigger states, including a possible array trigger, and distributes the main trigger as well as the main clock to all boards for a synchronous working of all camera parts. The trigger state is also sent to the array trigger for an intertelescope operation. A master trigger card can handle up to 12 trigger boards/crates.

20 samples (80 ns) per pixel are sent to the computer farm in case of a trigger event. Hence, the ring buffer capacity of 4000 samples (16 μs) allows pre- and post-trigger data to be sent and more important that the writing of the ring buffer has not to be stopped while reading these data. With a maximal trigger rate of 10 kHz, the data amounts to 700 MByte/s (5.6 Gbit/s) that has to be sent over the Gigabit-link (10 Gbit Ethernet link). Hence, a nearly dead time free system is possible with FlashCam[2]. Finally, the stored data will be analyzed off line, event by event.

The implementation of FlashCam has happened in several steps. Each step proved a piece of the concept towards a fully digital camera. This chapter discusses the most relevant hardware and software parts of FlashCam, like the implementation of the nonlinear amplifier, the transmission of analogue signals over commercial network cables and so on. Measurements showing the performance of the camera electronics are presented in chapter 5.

---

[2] The system is dead time free as long as the data can be written down to the computer farm without waiting time and the overall trigger rate is $\lesssim$ 10kHz.

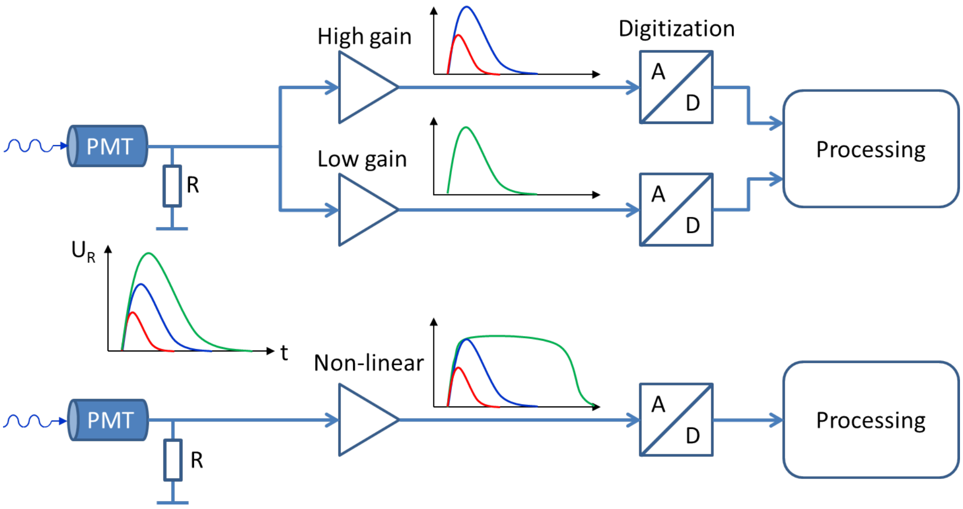

Figure 4.3: Comparison of the linear dual (top) and linear-nonlinear single (bottom) signal path concept. The signal shape before and after the amplification stage is shown for three amplitudes.

4.2 The nonlinear amplifier

A number of approaches exist for a single signal path solution to cover a large dynamic range. However, most suffer from non-reproducibility through component variations and temperature changes, complicated nonlinear transfer characteristics which need complicated unfolding algorithms etc. Thus, a simple and reproducible approach with a linear-nonlinear amplifier that changes between these two transfer characteristics according to the input pulse amplitude with an adjustable transition between the two regimes has been studied. In the linear regime, where the pulse amplitudes are small (for example $\lesssim$200 pe), the pulses are transfered proportionally and undistorted to the output of the amplifier. The amplifier transfer function becomes nonlinear with the input signals exceeding the transition threshold and transforms the pulses into clipped and stretched pulses (figure 4.3). These new pulses contain the original amplitude information in their area rather than in their amplitude, thus extending the dynamic range. A dedicated algorithm, described in 4.5, processes both signal types and extracts the amplitude and timing information of the pulses with high precision.
A current-feedback amplifier (CFA) shows this linear-nonlinear behavior and the working principle is described next to better understand the concept of the approach.

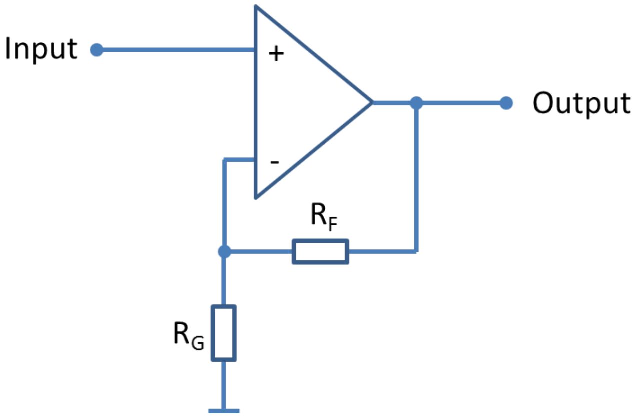

Figure 4.4: Operational amplifier wired in a non-inverting circuit.

4.2.1 Current-feedback amplifier

Figure 4.4 shows a typical non-inverting circuit with an operational amplifier (op amp). The voltage gain of the amplifier is defined through the resistors as $AV = (R_G + R_F)/R_G$. The voltage output of the op amp is fed back to the amplifier's inverting input over the feedback resistor R_F. Depending on the internal impedance of the amplifier, a voltage (for high impedance) or a current (low impedance) is fed into the negative input. The input impedance is highly dependent on the internal construction of the op amp. A voltage-feedback amplifier has a high, and a current-feedback amplifier a low negative-input impedance and the two amplifier types work slightly different [69]. The more commonly used voltage-feedback amplifier (VFA) is internally organized in three stages: a differential input amplifier, a gain stage and an output stage (figure 4.5). The differential input amplifier provides symmetrical input impedances for the non-inverting (+In) and the inverting (-In) input. The feedback from the op amp output is fed back as a voltage to the inverting input. Figure 4.7 (left) shows the frequency-gain dependence for two different gain settings $AV1$ and $AV2$ of the op amp circuit, set with R_F and R_G, and the open-loop gain AOL of a VFA. The open-loop gain is the gain of the op amp without any feedback to the input. It is infinite for an ideal op amp and drops with increasing frequency. The AOL of a VFA is independent of the set gain and the gain-bandwidth product is constant. Hence, the actual op amp gain rolls off earlier for the higher set gain $AV2$. This gain-dependent roll off can be compensated with an additional external circuit (frequency compensation) but with the drawback that the op amp's cutoff frequency decreases or is limited to low values [70].

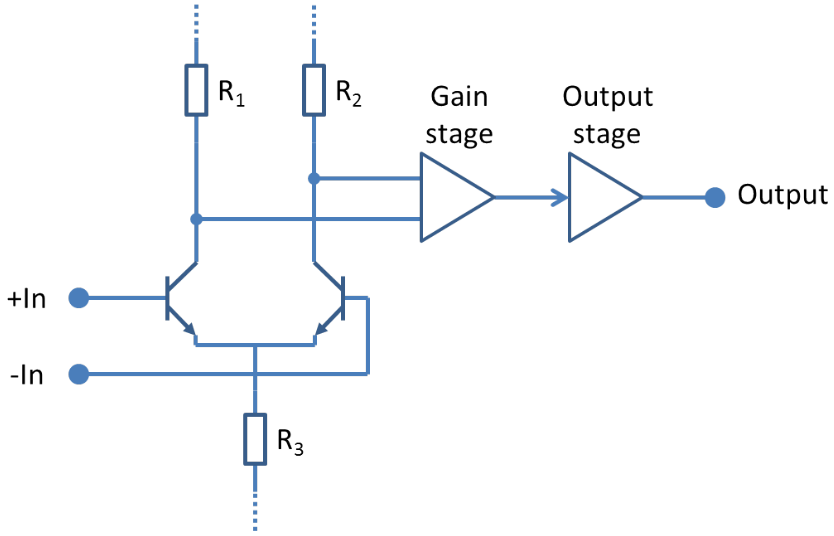

Figure 4.5: Simplified sketch of the internal circuit of a voltage-feedback op amp with a differential input, a gain and output stage.

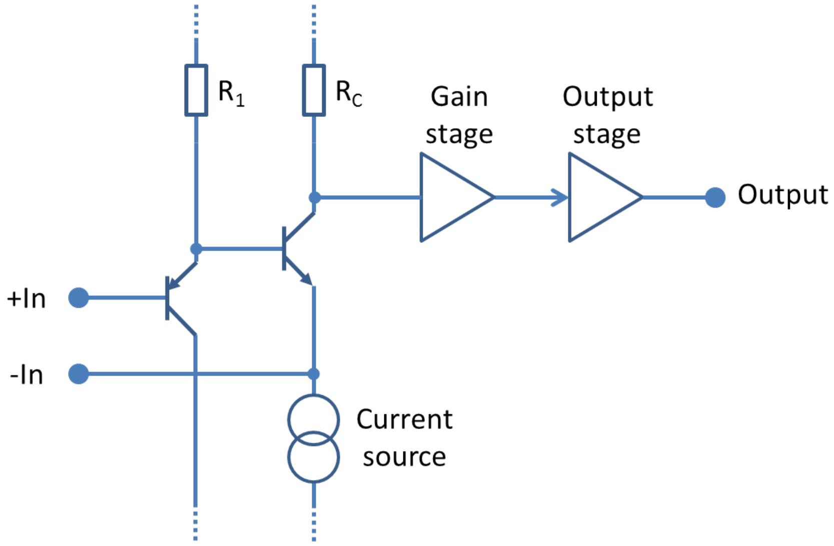

Figure 4.6: Simplified sketch of the internal circuit of a current-feedback op amp with an emitter follower input stage, a gain and output stage.

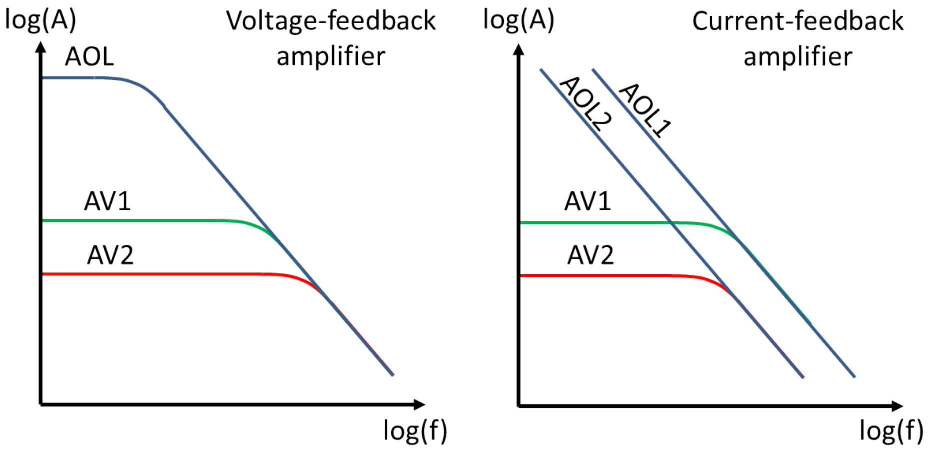

Figure 4.7: Left: Voltage-feedback amplifier: the open-loop gain, AOL, is independent of the set gain, AV. A higher gain setting results thus in an earlier roll off of the amplification for high frequencies.
Right: Current-feedback amplifier: the open-loop gain, AOL, depends on the set gain, AV. The amplification roll off is independent of the gain setting and the frequency.

The current-feedback amplifier (CFA) has three stages as well, but the input stage is designed as an emitter follower instead of a differential amplifier (figure 4.6). Thus, the op amp inputs $+In$ and $-In$ are no longer symmetric in their impedances. The inverting input is now a low-impedance input (e.g. 50 Ω), where the feedback signal is fed in as a current. The non-inverting input has some tenth of mega ohm impedance, like the VFA. The analogue bandwidth of a CFA is almost independent of the set gain, due to its internal construction. The actual gain roll off is hence independent of the set gain AV (figure 4.7, right). The open-loop gain changes with the set gain AV according to

$$A_{OL} = \frac{R_C}{R_G \cdot R_F / (R_G + R_F)} \cdot A_1 \tag{4.1}$$

with A_1 the constant open-loop gain of the gain and output stages. The gain of the emitter follower stage is described by the first factor in the equation with the internal collector resistor R_C, the feedback resistor R_F and the gain setting resistor R_G. The set gain AV of the CFA is set by the ratio of R_F and R_G. The described behavior is only valid for ideal op amps and shows no frequency dependency. Looking at the output-to-input ratio of an actual voltage (eq. 4.2) and current-feedback amplifier (eq. 4.3) shows the frequency dependency.

$$\frac{u_{out}}{u_{in}} = \frac{R_F + R_G}{R_G} \cdot \frac{1}{1 + \frac{1}{A_{OL}(j\omega)} \cdot \frac{R_F + R_G}{R_G}} \qquad (VFA) \tag{4.2}$$

$$\frac{u_{out}}{u_{in}} = \frac{R_F + R_G}{R_G} \cdot \frac{1}{1 + \frac{1}{Z_{TR}(j\omega)} \cdot R_F} \qquad (CFA) \tag{4.3}$$

The VFA shows a frequency-dependent open-loop gain $A_{OL}(j\omega)$ in its transfer function, while the CFA only has a frequency-dependent factor $Z_{TR}(j\omega)$ of the internal transimpedance (a transimpedance converts a current into a voltage, see e.g. [71] for more details). Thus, there is no need for frequency compensation for a CFA and the gain is only set by R_G.

A feature of some CFA is their behavior when the input signal applied to the op amp is exceeding the maximal allowed value (input overdriving) or when the output of the op amp is driven into saturation (output overdriving). Input overdriving is visible in a distorted output signal with clipping and dipping of the signal and should clearly be avoided to protect the op amp from being damaged. The output of the op amp will overdrive as soon as the output amplitude reaches the maximum output voltage swing. Since the op amp is not able to increase its output voltage further it loses the feedback to the inverting input to compensate the voltage difference at the non-inverting and inverting input, as it usually does. However, the input signal appears not just clipped at the op amp's output but is also extended due to the decreasing of the bandwidth of the first two stages and hence a decreasing of the open-loop gain. This change in bandwidth can be compared to the response of a low pass filter to a delta-like pulse, as seen in figure 4.8: the leading edge is transfered to the output almost one-to-one, but, the output is only slowly decreasing while the input signal is already gone. The energy is thus transfered to the capacitor of the low-pass filter and then released with a the capacitor's time constant. Same happens inside the amplifier with the internal capacitors. This results in the nonlinear transfer function for the overdriving output. The op amp output overdrives as long as the overdrive condition remains and will eventually recover and return to linear operation as the input drops below the overdrive condition threshold. However, leaving the overdrive state does not happen instantly inside the amplifier. The amplifier recovers slowly while increasing its bandwidth and so returning to normal operation. The recovery time depends on the chosen amplifier and on the amplitude of the input signal. The signal shape has a rather minor effect on the recovery time.

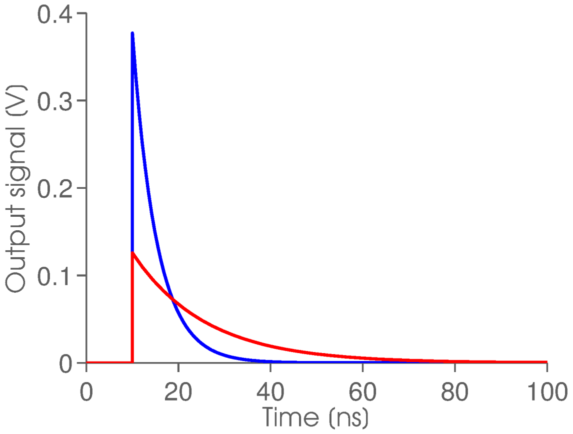

Figure 4.8: Simulation to show the principle of decreasing the analogue bandwidth of a signal with a low-pass filter. A delta pulse is fed into the RC circuit and the capacity is changed to simulate 30 MHz (blue) and 10 MHz (red) bandwidth.

A circuit simulation with the LTSpice [72] software shows the expected amplification versus frequency diagrams for the VFA and the CFA (figure 4.9).

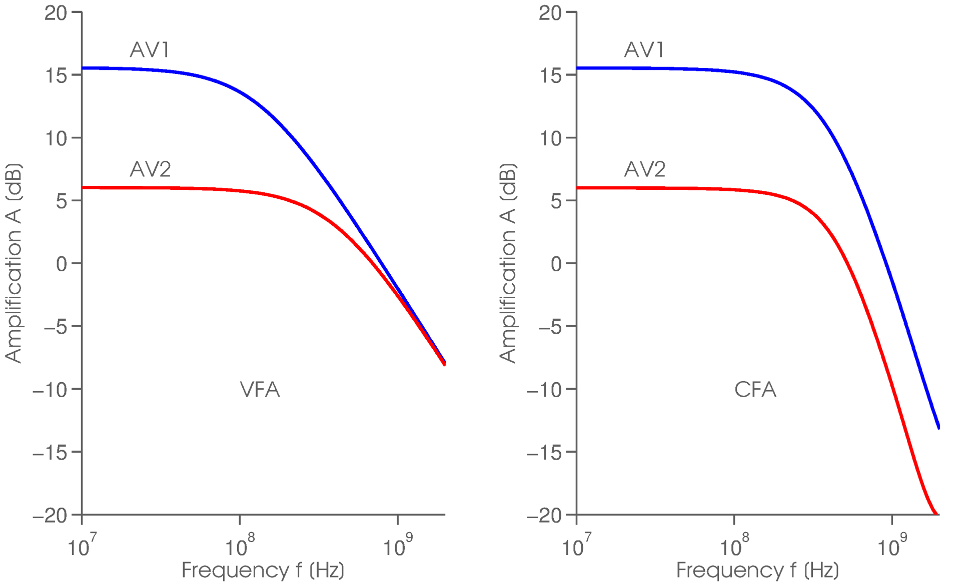

Figure 4.9: Simulated Bode diagrams of a VFA (single-pole amplifier *opamp* with $AOL = 10^5$ and a gain-bandwidth product $GBW = 800\,\mathrm{MHz}$) and a CFA (AD8001A) at gains $AV1 = 6$ and $AV2 = 2$ ($R_F = 1000\,\Omega$, $R_G = 200$ and $1000\,\Omega$). Simulation performed with LTSpice.

The clipping threshold is influenced by two parameters: the gain of the amplifier and the voltage supply. Both parameters might be used separately or in combination to change the threshold, but one should keep in mind that changing the power supply also changes the output voltage range of the amplifier. However, if the supply voltage is change and the input signals are delivered from a PMT, it is sufficient to change the negative supply only, since the PMT signals are negative and will only be clipped at the negative output swing.

Very important to note for a correct working of the saturation concept is that the anti-aliasing filter for the signal bandwidth reduction for the ADC has to be place after the amplifier. A reduction of the analogue bandwidth before the amplifier will cause the amplifier output to rise very fast under a saturation condition. The new pulse will thus have a larger analogue bandwidth violating the Nyquist requirement. This fast edge is subsequently sampled by the ADC with only a single sample and hence a correct time reconstruction will not be possible.

Understanding the correlation between input and output signal over the whole dynamic range allows the use of the current-feedback amplifier as a linear-nonlinear amplifier. More details about current-feedback amplifiers can be found in [69], [73], [74] or [70].

4.2.2 CFA AD8001

First tests have been performed with the current-feedback operational amplifier AD8000 (135 mW, 1.5 GHz bandwidth) from Analog Devices, which has been replaced by the less power-hungry AD8001 (50 mW, 800 MHz bandwidth). Its maximum output voltage swing is ±3.1 V at ±5 V voltage supply. Exceeding this output voltage limit will cause the amplifier to clip the signal as described before. The amplifier will return to normal operation after a clipping condition occurred with an output overdrive recovery time of 20-70 ns.

4.3 The amplifier circuit

The amplifier circuit is realized with the CFA AD8001 wired in a non-inverting circuit as shown in figure 4.10. The non-inverting input of the amplifier is connected directly to the anode of the PMT. A short connection to the anode lead of $\lesssim 30\,\text{mm}$ will prevent signal ringing due to the high

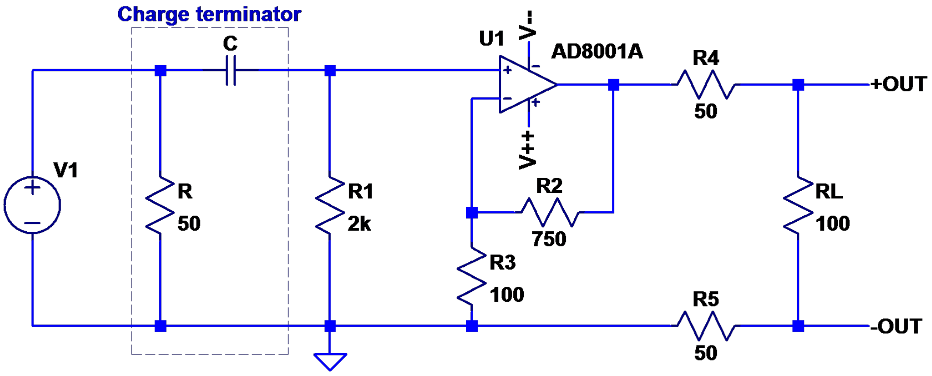

Figure 4.10: LTSpice circuit of the amplifier with fixed gain of 2. A charge terminator circuit (R and C) is connected at the input to simulate the output pulse shape of a PMT. The resistors R_4 and R_5 are used for a pseudo-differential signal transmission to the digitization electronics and the load resistor R_L is the input resistor of the digitization electronics.

impedance of the load resistor $R_1 = 2\,\mathrm{k}\Omega$. The gain of the amplifier is set with the two resistors R_2 (value taken from data sheet of AD8001) and R_3 to a fixed gain of $G = 1 + R_2/R_3$. Replacing R_3 with a voltage controllable resistor as shown in section 4.3.2, allows to change the gain with the slow control. The output signal of the amplifier circuit is transmitted pseudo-differentially (R_4 and R_5) to the digitization electronics (termination resistor R_L). A charge terminator (R and C) with a capacitor simulating the PMT capacitance (4.5 pF for the Hamamatsu R11920, 10.2 pF for the Photonis XP2960 PMT) has been used instead of a PMT for several tests, since the output amplitudes can be controlled much better (see section 6.2).
A simulation of the amplifier circuit with a fix R_3 is shown in figure 4.11. The long tail of the input signal comes from the large value of R_1, which results in a time constant $\tau = R_1 C = 2\,\mathrm{k}\Omega \cdot 4.5\,\mathrm{pF} = 9\,\mathrm{ns}$ and a duration of $t \approx 5\tau = 45\,\mathrm{ns}$. The pulse leading edge in contrast is very fast as expected. For the real case with a PMT it is essentially only depending on the arrival time of the secondary electrons at the anode. The broadening of the output signal due to clipping and recovery of the amplifier is nicely visible.

4.3.1 PMT load resistor

The load resistor R_1 in figure 4.10 transforms the charge accumulated by the charge terminator or the PMT anode into a voltage. Moreover, it affects the trailing slope of the created pulse since the slope is defined by the decay

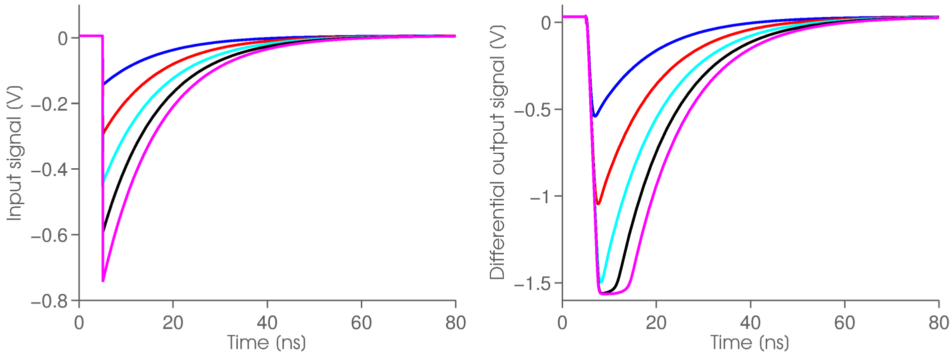

Figure 4.11: LTSpice simulation of the amplifier circuit. The charge terminator capacitor is $C = 4.5\,\mathrm{pF}$, the gain resistor R_3 is 100 Ω for a gain of 8.5 and the voltages are measured over R_1 (left) and differentially over R_L (right). The input pulse to the charge terminator is a step function with 100 ps fall time and amplitudes of -200 mV to -1 V in 200 mV steps. The amplifier is powered with ±5 V.

time $\tau_{trailing} = R_1 C$. τ specifies the time of the slope-amplitude-change of about ~36% (~$1/e^1$). The trailing slope can hence be extended by increasing R_1, without influencing the leading slope. The latter is very important to keep, since it provides a good measure for the arrival time of the Cherenkov photons. Furthermore, increasing the load resistance increases the pulse amplitude for the same charge ($Q = t \cdot U/R$). The larger pulse allows a lower gain of the subsequent amplifier, which in turn minimizes the noise contribution of the subsequent amplifier. A PMT has typically an output capacitance of C = 5-10 pF and is loaded with a ≤50 Ω resistor.

A PMT would collect the secondary electrons at the anode in about 2.5 ns without a load resistor. Connecting the load resistor R to the charged anode will discharge it and convert the charge into a voltage with a decay time $\tau = RC$ of ~250-500 ps. The leading edge of the PMT output signal, being before 2.5 ns, shortens with connected load resistor as the resistor discharges the anode with a much faster time constant then it is charged by the secondary electrons. This leads to an output amplitude reduction of approximately the ratio of the charge and discharge times 2.5 ns/0.5 ns. The amplitude of a single photoelectron of a PMT with gain 50000 is about

$$U \approx \frac{\tau_{discharge}}{\tau_{charge}} \cdot \frac{50000 \cdot e}{C} = 160\ \mu\mathrm{V} \tag{4.4}$$

for typical PMT capacitance C of 10 pF. Hence, the output signal needs to be amplified significantly (~x15) to get a reasonable resolution of about 10 LSB per photoelectron with an ADC with input range of 1 V and 12 bit resolution. Using a larger load resistor of 1 kΩ for instance, will give a single photoelectron amplitude of ~3.2 mV, which already corresponds to about 13 LSB for the same ADC without prior amplification.

The drawback of a large load resistor seems to be the long trailing edge ($\tau \approx 10$ ns for $C = 10$ pF and $R = 1$ kΩ), which can be eliminated on the digitized signal in a post-process. The post-process differentiates the signal, hence getting rid of the long trailing edge and reducing under- or overshoots introduced by the differentiation by applying a pole-zero cancellation to the signal (see section 4.5.1). The analogue bandwidth of the PMT changes with the load resistor according to equation 6.1. The changing of the load resistor from 50 to 2000 Ω changes the bandwidth of the PMT from ~700 MHz to ~17 MHz and hence allows the use of amplifiers with rather low analogue bandwidths, compared to the analogue ring samplers mentioned previously.

4.3.2 Gain setting

Being able to change the gain of the AD8001 has several advantages, as for example the adaptation of the dynamic range for different PMT gains or even different photo-detectors like MPPCs, changing the output clipping threshold, etc.

Figure 4.12 shows the replacement circuit for R_3 of the first attempt to use the electronic switch ADG711 from Analogue Device with four internal CMOS switches. The switches are attached to four resistors, which could replace R_3 in any possible combination of the switches, resulting in a large range of discrete gain settings. The large ON capacitance of the switches (~22 pF per switch) influences the high frequency transmission behavior of the op amp AD8001 and hence distorts the output signal, making these switches useless for our purpose. Hence, the resistor R_3 has been replaced by the field effect transistor (FET) circuit, shown in figure 4.13.

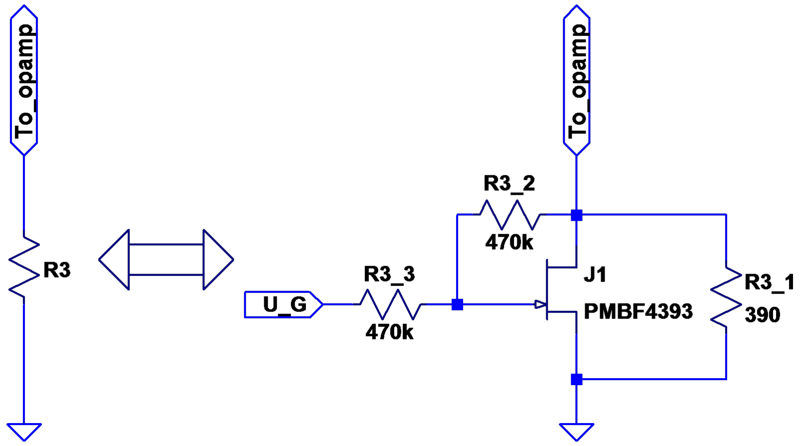

Figure 4.13: Replacement of the gain resistor R_3 with a FET circuit working in its ohmic regime for a variable gain setting of the AD8001. U_G is a negative voltage to control the resistivity of the FET.

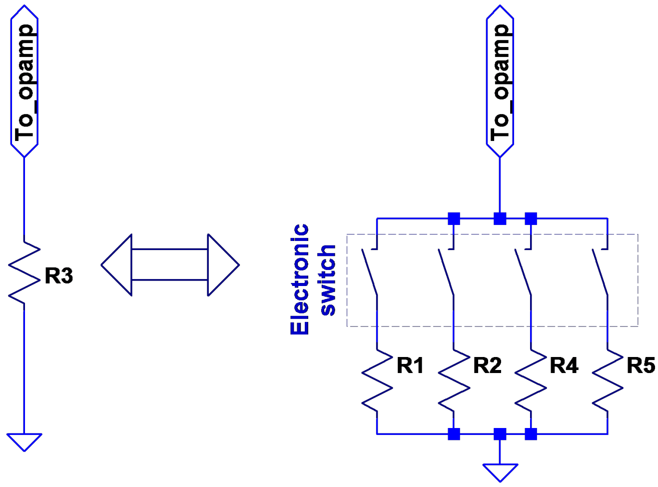

Figure 4.12: Replacement of the gain resistor R_3 with an electronic switch circuit attached to a series of resistors for a variable gain setting of the AD8001. The electronic switches are set by applying logical signals to the chip.

A FET acts like a voltage controlled resistor (VCR) while being operated at very low gate-source voltages V_{GS} in the so called ohmic or linear region (figure 4.14).

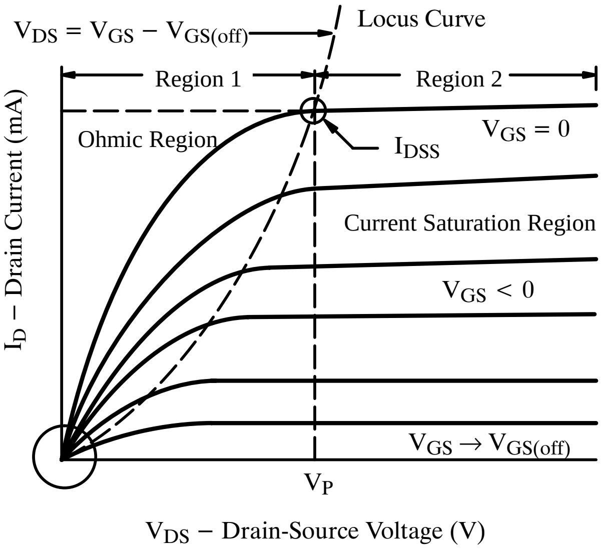

Figure 4.14: Output plot of a typical n-channel FET. The FET behaves linearly ohmic in region 1 at low drain-source voltages and for low drain currents for all gate-source voltages. This can be used to built a voltage controlled resistor with a FET. Picture taken from application note Siliconix AN105.

The relation between the drain current I_D and the drain-source voltage V_{DS} is linear over a large range for $V_{GS} \approx 0$. The drain source resistance r_{DS} reaches values in the range of 90 to 4000 Ω for gate control voltages U_G of -1.9 to 0 V for the chosen FET PMBF4393. Many other types of FETs have been tested and simulated, but no one, not even other types of the 4393 had such a large linear region. This corresponds to a gain of 3 to 11 with the parallel resistor R_{3_1}. The resistor R_{3_1} defines the largest resistance possible (FET not conductive) and hence the lowest gain and protects the amplifier of going into an instable stage while the FET has a very high impedance. Figure 4.15 shows the gate control voltage versus the amplifier gain, measured with a charge terminator (10.2 pF) and the FC250 digitization board (section 4.4) and superposed with a simulation done with LTSpice. The resistors R_{3_2} and R_{3_3} are used as voltage divider reducing the gate control voltage sensitivity by a factor of two and linearizing the resistivity of the drain-source path r_{DS} by adding a small portion of the input signal to the gate (see application note Siliconix AN105). High values for the resistors are recommended as they shunt r_{DS}. The drawback of using a FET is its temperature dependency. It introduces a negative temperature dependency of the amplifier gain of about 0.35% per kelvin (0.04% per kelvin for a fix resistor R_3). The temperature dependency results are shown in the

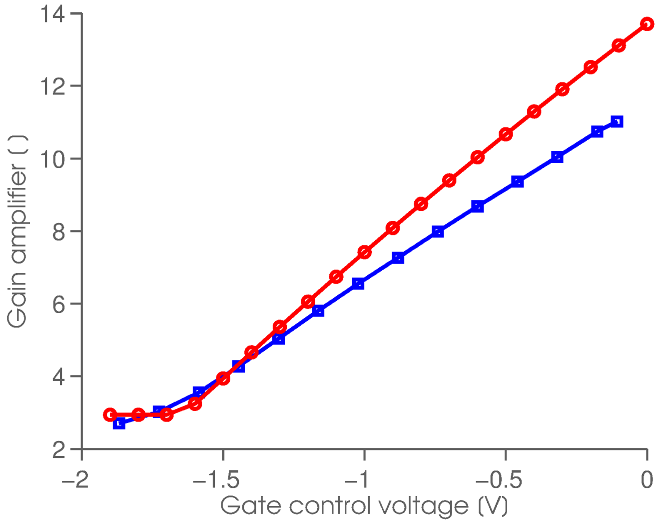

Figure 4.15: Amplifier gain versus FET adjusting gate voltage measured (blue, squares) and simulated (red, circles). The different slopes are due to component tolerances. The flattening at low gate control voltages shows that the resistance of the FET is too high to change the overall resistance: the remaining resistor R_{3_1} dominates the gain setting.

next section 4.3.3.

Figures 4.16 and 4.17 show measurements of the output of the AD8001 amplifier used with the electronic switch or the FET circuit. A charge terminator (10.2 pF) is used to generate the input pulses to the op amp and the output of the AD8001 is directly measured and stored with a scope and analyzed off line with MATLAB. Distortions appear as a prolonged tail (no nice exponential tail anymore) while using the switch for the gain control due to the ON capacitance changing the transfer characteristics of the amplifier.

4.3.3 Temperature behavior

The temperature dependence of the amplifier with the FET circuit and with a single resistor for gain setting, is tested in a temperature box with a built-in thermoelectric (Peltier) element. The temperature is regulated between 16 to 40°C. A single PMT base with the integrated amplifier circuit set at a gain of 4.3 has been used for the tests. The amplifier with the FET circuit was measured first and then the FET circuit replaced by an equivalent single resistor R_3 for comparison of the temperature stability. A fixed pulse corresponding to ~126 pe is fed over a charge terminator (C = 10.2 pF) into

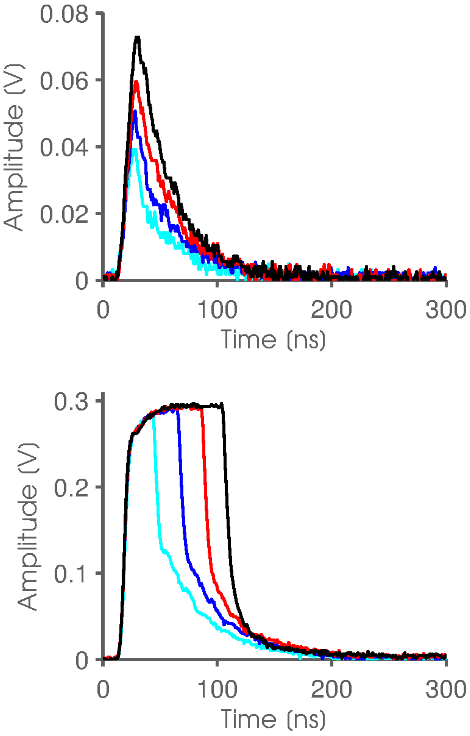

Figure 4.16: Each plot shows the output of the AD8001 with four different gains set by the electronic switch (figure 4.12). The different plots show different input signal amplitudes (note the different y-axes). The output signal of the amplifier is slightly distorted in the trailing tail due to the capacitance of the switch's ON state, compared to the op amp output when using the FET circuit (figure 4.17).

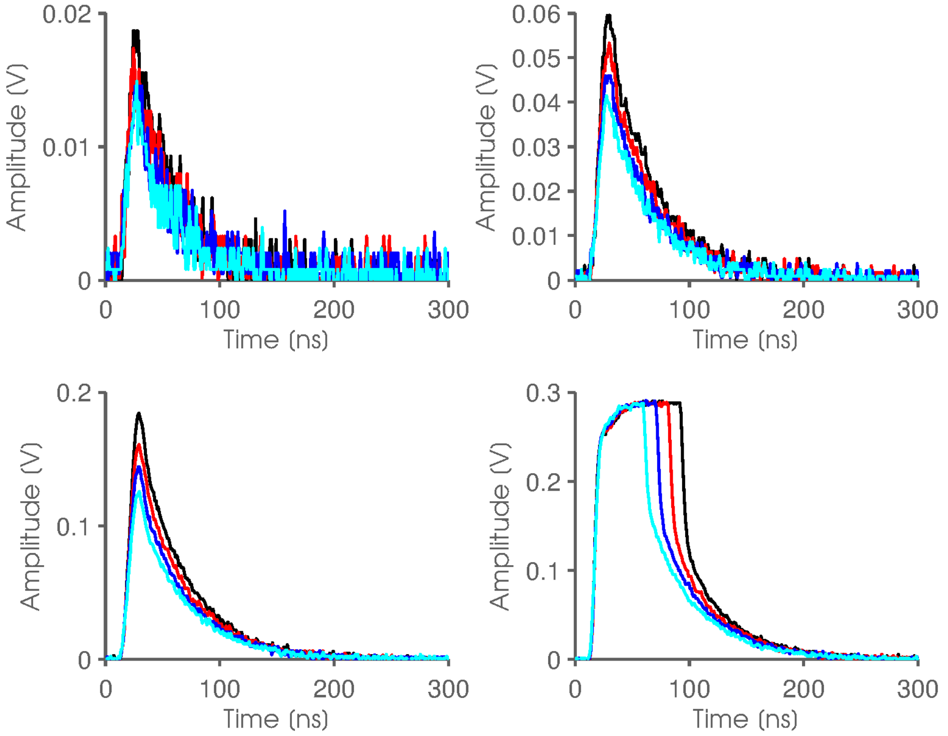

Figure 4.17: Each plot shows the output of the AD8001 with four different gains set by the FET circuit (figure 4.13). The different plots show different input signal amplitudes (note the different y-axes). The distortion of the output signal seen with the electronic switch circuit has disappeared. The settable gain range is smaller with the FET circuit than with the electronic switch circuit.

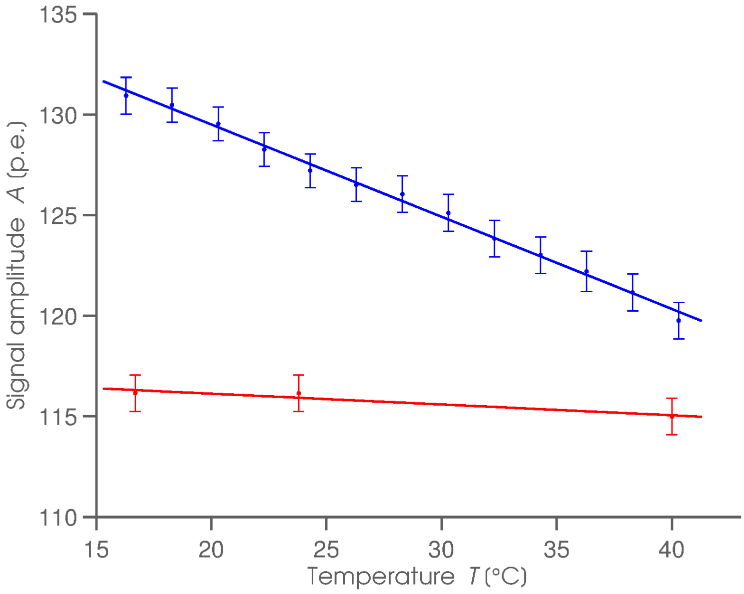

Figure 4.18: Temperature dependence of the amplifier circuit wired with a FET circuit (blue curve) and a single resistor (red curve) for gain setting. Shown are the measurements as dots and linear fits. Uncertainties of the temperature measurement are ±0.1 °C. The decrease of the gain is mainly due to the temperature dependent conductivity drift of the FET. Replacing the FET by a resistor minimizes the temperature dependence of the whole circuit.

the amplifier. The output of the amplifier is connected over a CAT5 cable to the scope, which is terminated with $50\,\Omega$. Figure 4.18 shows the temperature behavior of the two different gain circuits. The FET circuit shows a gradient of $m = 0.46\,\mathrm{pe/K}$, while the gradient almost disappears when replacing the FET by the resistor. The behavior is expected due to the positive-temperature-coefficient-like behavior of field effect transistors (increasing temperature decreases conductivity). The data sheet of the PMBF4393 FET does not state a number for its temperature coefficient. A compensation of the FET temperature dependence per pixel could be performed for example in real time in the FPGA, since the dependence is linear.

4.4 The demo board FC250

In order to test the FlashCam concept, a demonstrator board was developed and built at MPI-K, Heidelberg. The FC250 hosts the ADC-driver AD8132 (schematics of the input stage with the ADC-driver is shown in the appendix A.4), eight 250 MSps 12 bit ADCs (Analog Devices AD9230BCPZ-250) and four 80 MSps 14 bit dual ADCs (AD9251BCPZ-80). The 80 MSps ADCs were intended to be used for a dual-signal path solution, which has been rejected in favor of the single-signal path solution, prior to the development of the linear-nonlinear amplifier of the previous section. The 80 MSps ADC path has actually not been used for any measurements. The ADCs are connected to a SPARTAN 3A FPGA from Xilinx (XC3SD3400A-4FGG676C), which is used as data ring buffer and as micro controller (a 32Bit RISC processor called microblaze is emulated inside the FPGA). The board can be triggered by an external logical signal fed into a separate trigger input. In these tests, a laser is used to test the system. The control unit for the laser also supplies a trigger output, which is fed to the FC250 trigger input. The trigger signal from the laser control unit is delayed by about 190 ns before being fed into the FC250 to prevent pile-up with the measured PMT laser signal in case of electronics cross-talk. The digitized data is sent with each trigger via Ethernet to a computer for storage and off line analysis.

Two FC250 boards are connected for synchronous readout of up to 16 pixels. A single board is powered by 24 V, 0.7 A (spike of up to 2 A at power on). The FC250 can be controlled and read out via Ethernet with the special software *fc250*, coded by T. Kihm. The most important commands used with the software are listed in the appendix A.5.

4.4.1 Synchronizing multiple FC250

Figure 4.19 shows a photograph of a master and a slave FC250 working in a synchronous mode. The clock of 250 MHz and the trigger signals are delivered by the master board over a CAT5 connection. The length of the cable should be chosen such that the clock shift is a multiple of 4 ns. The clock phase can be delayed slightly inside the master FPGA to match the two clocks. A 1 pps (pulse per second) signal is sent from the master to the slave to synchronize the internal slave clocks. Both boards are connected via Ethernet to a computer and read out with two instances of the *fc250* software. The procedure and commands used for synchronizing two FC250 boards are described in appendix A.5.1.

4.4.2 FC250 input calibration

The analogue inputs of the FC250 board need to be calibrated in order to know the conversion factor from the input voltage to the digitized value.

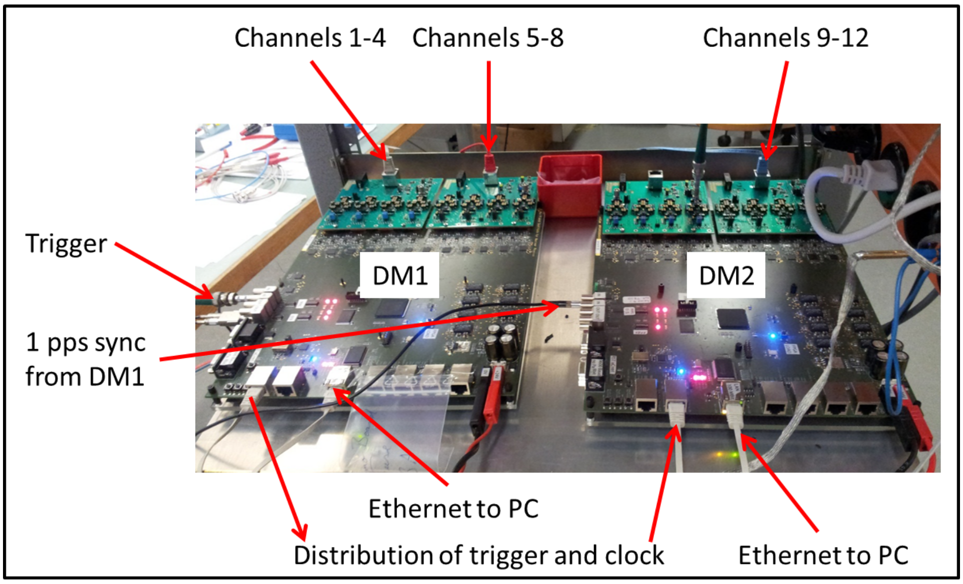

Figure 4.19: Two FC250 demo boards set in master (DM1) and slave (DM2) mode for synchronous operation.

Figure 4.20 shows the circuit of the input stage with the ADC driver of one channel of the FC250, connected over a CATx cable to the two resistors of the AD8001 amplifier for the pseudo-differential transmission.

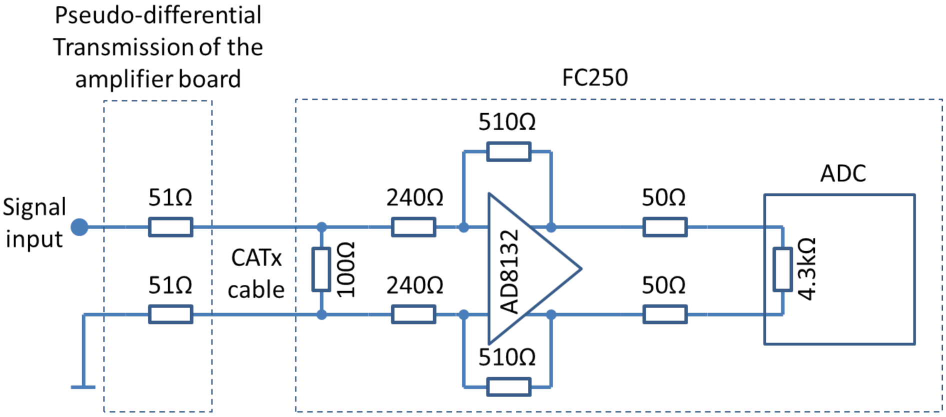

Figure 4.20: Schematics of the pseudo-differential transmission located on the amplifier circuit board, connected to the ADC driver circuit with the ADC, both located on the digitization electronics board FC250.

These two 51 Ω resistors are wired to the amplifier circuit of the AD8001 or to a signal generator and the oscilloscope for the calibration, respectively.

The gain factor of the circuit can be split into three parts: the voltage divider with the pseudo-differential resistors and the termination resistor of 100 Ω, the ADC driver amplifier and finally the voltage divider with the internal ADC resistor. The gain factor G of the whole electronics chain is calculated as

$$G = \frac{100\Omega}{51\Omega + 100\Omega + 51\Omega} \cdot \frac{510\Omega}{240\Omega} \cdot \frac{4300\Omega}{50\Omega + 4300\Omega + 50\Omega} = 1.028 \qquad (4.5)$$

A pulse generator is connected to the scope and to the input of the circuit to measure and verify the gain factor of the electronics chain. The peak of the digitized pulse is converted into a voltage by dividing the peak value by the resolution of the ADC (12 bit = 4096 LSBs) and multiplying it by the voltage input range of the ADC (1.25V). The factor G is then calculated as the ratio of this voltage and the measured scope peak voltage. The base line is subtracted for both values beforehand. Table 4.1 shows the values of the 12 channels, distributed over the two FC250 DM1 (channels 1-8) and DM2 (channels 9-12), used to later readout the photo-detector plane board (section 4.7). The calculated and measured gain factors are in good agreement, deviating only by about 3-6%.

Channel	FC250	Gain
1	DM1	0.9729
2	DM1	0.9728
3	DM1	0.9724
4	DM1	0.9783
5	DM1	0.9659
6	DM1	0.9734
7	DM1	0.9681
8	DM1	0.9643
9	DM2	0.9729
10	DM2	0.9924
11	DM2	0.9702
12	DM2	0.9958

Table 4.1: Gain of channels 1-8 of FC250 DM1 (master) and 9-12 of FC250 DM2 (slave).

4.5 Improved post-processing algorithm

The algorithm for post-processing of the digitized signals described in section 3.1.2 has been adapted in order to gain in time and amplitude resolution and to process the clipped signals as well.

4.5.1 Signal shaping and Reconstruction

The digitized data are first up-sampled from 250 MSps to 1 GSps by interpolation between the samples, as described in section 3.1.2 and smoothed with a SMA filter of 4 samples. Figure 4.21(b) shows the up-sampling and the smoothing, applied to a digitized signal (a).

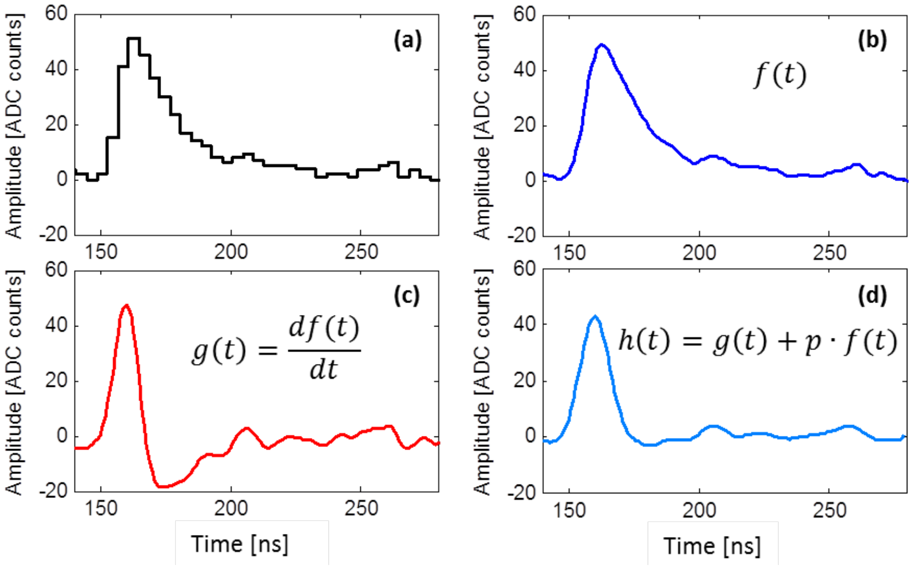

Figure 4.21: Post-processing of the off line data. (a) digitized signal with 4 ns resolution. (b) increased resolution by up-sampling, smoothing added. (c) Differentiated signal for time extraction. (d) undershoot corrected signal for amplitude extraction.

The subsequent differentiation of the signal (b) yields a signal (c) with a fast leading and trailing edge, eliminating the long tail which is introduced by the large PMT load resistor. The signal is best suited to determine the arrival time of the pulse by calculating the center of gravity of the area between the pulse maximum and the full width at half maximum, as already described in section 3.1.3. The undershoot, introduced by the differentiation, becomes a problem the moment a second signal piles-up at around that position. The amplitude of this second signal would be reduced artificially by the undershoot. A pole-zero cancellation, described in more detail in appendix A.6, adds a portion of the original signal to the differentiated signal. Since the original and the differentiated signal have tails with the same timescale but opposite polarity, the adding up of the two signals can remove the undershoot of the differentiated signal (d). The analytic implementation of the differentiation with pole-zero cancellation is given as

$$g(t) = \frac{d}{dt} f(t) + p \cdot f(t) \tag{4.6}$$

with $f(t)$ the input signal, $0 < p < 1$ defines the portion of the input signal to be added to the differentiated signal and $g(t)$ is the undershoot-free output signal. A 'wrong' value of p results in an under or over compensation of the undershoot. Finally, the amplitude information of the pulse is determined from the data in (d), after applying additional SMA filters as mention in previous sections.

Signals that are clipped by the amplifier and are processed with the algorithm described, will give a good time resolution but wrong amplitude information. Figure 4.22(a) shows such a clipped signal after digitization.

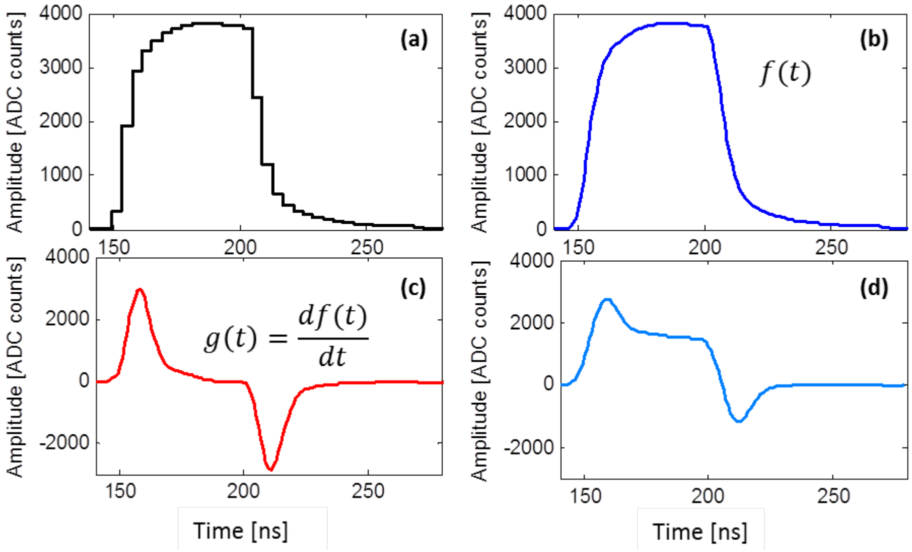

Figure 4.22: Post-processing of the off line data for a clipped input pulse. (a) digitized signal with 4 ns resolution. (b) increased resolution by up-sampling, smoothing added. The signal is integrated to get the amplitude information. (c) Differentiated signal for time extraction. (d) undershoot corrected signal, but not usable for amplitude extraction.

The up-sampling and smoothing (b) still works as expected but the differentiation leads to two peaks (c). The first peak is used for the time extraction, as described above. However, the pole-zero cancellation does not work properly anymore (d). Hence, the amplitude is extracted from an integration of signal (b) over a window of at most 200 ns. Signals causing the amplifier clipping are already so large (>200 pe) that NSB does not influence the signal to noise ratio.

Figure 4.23 shows a measurement using the AD8001 amplifier circuit connected to a charge terminator (10.2 pF).

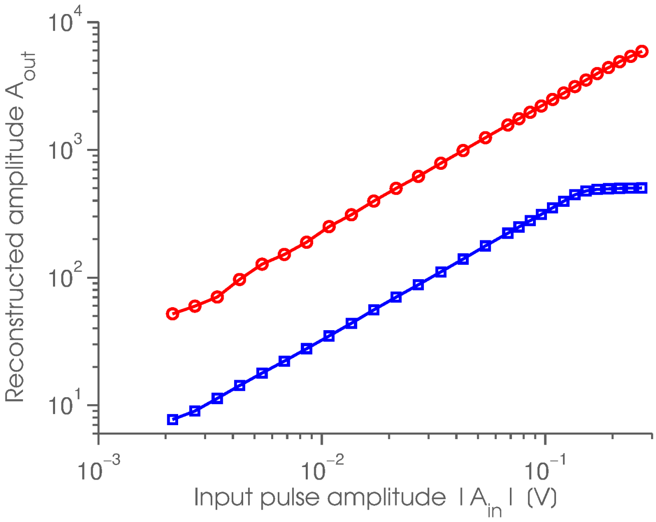

Figure 4.23: Analyzed and reconstructed output signal of the AD8001 circuit connected to the FC250. The amplitude maximum of the output signal delivers good results over the whole linear regime but flattens as the amplifier starts clipping at about 130 mV input amplitude (blue curve, squares). The area information (red curve, circles) is not as precise for low-input amplitudes, because the noise contribution is large, but becomes linear and stable from about 10 mV input up to 300 mV.

The load resistor was reduced to 50 Ω to be able to measure the input amplitude with the scope. This makes the signal again, without having the long tail introduced by the 2 kΩ resistor. The measurement was originally done to calibrate the electronics chain, but the results can also be used to prove the effectiveness of the algorithm (since the differentiation gets anyway rid of the long tail). Comparing the input amplitude, measured with the scope, with the reconstructed pulse amplitude and the pulse area, shows the transfer characteristics of the whole electronics chain. The peak amplitude information flattens out and is useless when the amplifier starts to clip the input. The integrated area, however, keeps on being linear and delivers the original amplitude information.

4.6 Analogue signal transmission via CATx cables

The analogue signal is transmitted from the PMT amplifier board to the ADC board over category (CAT) 5 or 6 cables, commonly used in Ethernet. The category number specifies the cable properties like signal bandwidth and shielding. The cables contain four twisted wire pairs and RJ45 connectors on each end. The length of each cable pair twist is varied without changing the characteristic impedance (e.g. 100 Ω at 100 MHz) to reduce crosstalk between the cable pairs. The variations of the twist introduce different lengths of the single pairs and hence different transmission time delays (delay skew), which are in the range of 500 ps/m for a CAT5 cable and not a problem for networks. FlashCam may have to compensate for these delays in order to maintain the time structure of the whole Cherenkov shower (under investigation).
Various CATx cables are distinguished by their shielding options. There are unshielded twisted pair (UTP), shielded twisted pair (STP), screened twisted pair (F/TP) and screened shielded twisted pair (S/FTP) cables. Figure 4.24 shows the two types UTP and S/FTP, used for the transmission of analogue signals for FlashCam.

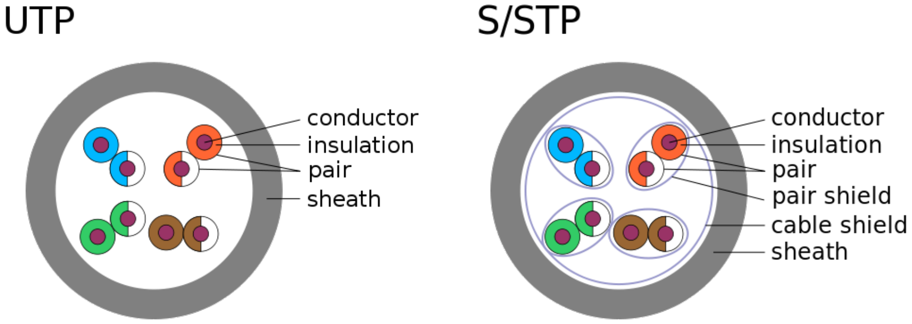

Figure 4.24: Sketch of a CATx unshielded twisted pair cable (UTP) and a screened shielded twisted pair cable (S/FTP) cable. Pictures taken from Wikipedia.

The UTP CAT6 cables are capable of transmitting bandwidths of 250 MHz, while the S/FTP can handle bandwidths of >500 MHz. Both types are suitable to use for the FlashCam electronics. The cable length for use of FlashCam in a camera housing will be about 2-3 m. Longer cables need to be installed if the digitization electronics are placed in a counting house or in the telescope tower.

4.6.1 Cable length and cable type

The cables listed in table 4.2 have been tested for their transmission quality and the crosstalk behavior (crosstalk results are presented in section 5.3.3). All UTP Wirewin cables are light-weight, so called slimpatch cables with a thickness of ~1/6 of the diameter of a common S/FTP cable. The tests with 2 and 3 m UTP Wirewin cables, which have been used for many measurements, are not shown here, but the results are comparable with the 5 m Wirewin cable.

Producer	Brack*	Shielding	Length [m]	Cable [CAT]	Connector [CAT]	AWG
Wirewin	114280	UTP	5	6	6	36
Wirewin	114258	UTP	15	6	6	36
Wirewin	135800	UTP	25	6	6	36
Wirewin	149838	S/FTP	15	6	6	27
Daetwyler	121551	S/FTP	15	6	6A	22
Daetwyler	121565	S/FTP	25	6	6A	22
R&M	-	S/FTP	8	6	6	26

Table 4.2: Tested CAT6 cables. *Part number of Brack Electronics AG (www.brack.ch).

The most important parameters for the analogue signal transmission over CATx cables are the wire diameter, quantified by the American wire gauge (AWG) category and the delay skew, which often is not given in the data sheet. A high AWG number means a high ohmic wire resistance and thus large signal loss. Table 4.3 shows the relevant AWG numbers and the equation

$$\text{wire diameter} = 0.127\,\text{mm} \cdot 92^{\frac{36-\text{AWG}}{39}} \tag{4.7}$$

gives the relation between AWG number and cable diameter.

AWG	Wire diameter [mm]	Wire area [mm^2]	Wire resistance [Ω/km]
22	0.644	0.326	53
26	0.405	0.129	134
27	0.361	0.102	169
36	0.127	0.0127	1361

Table 4.3: American wire gauges and corresponding wire parameters. Numbers from Wikipedia.

Figures 4.25,4.26 and 4.27 show the measured analogue PMT signal at the shunt resistor of 100 Ω at the input of the ADC driver AD8132 with a single ended probe (LeCroy HFP1000, 1 GHz bandwidth, 0.7 pF, 100 kΩ) connected to the scope. Each figure shows the results for a different laser intensity for the same cable types and cable lengths.

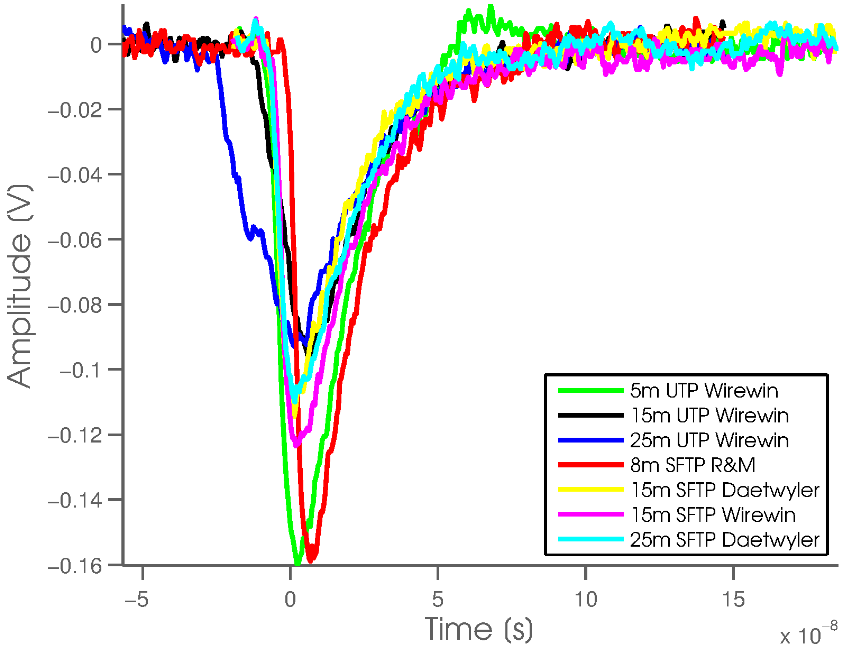

Figure 4.25: Measurement of the transmission characteristics of CAT6 cables with various lengths of different manufacturers. The light yield generates PMT pulses that are below the clipping threshold of the amplifier. The 5 m UTP Wirewin pulse can be taken as reference.

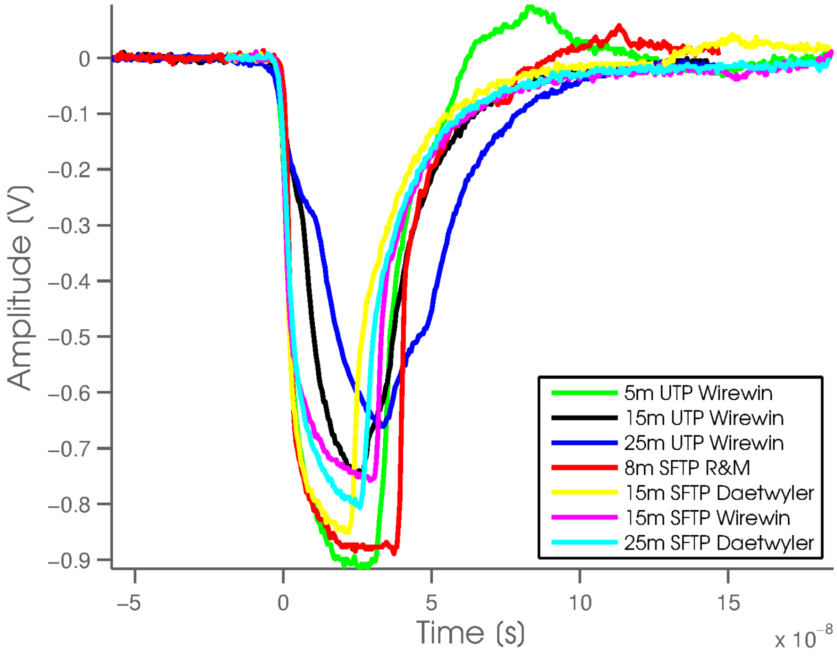

Figure 4.26: Same measurement as described in figure 4.25 with PMT pulses slightly above the clipping threshold. Reference is 5 m UTP Wirewin.

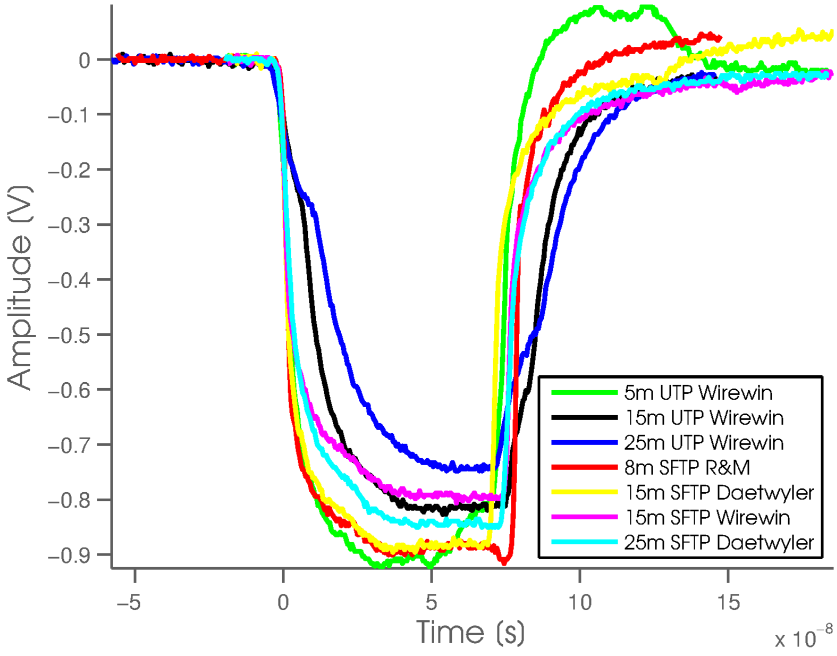

Figure 4.27: Same measurement as in figure 4.25 with PMT pulses well above the clipping threshold. Reference is 5 m UTP Wirewin.

The UTP Wirewin cables of 15 and 25 m length are clearly not suitable for the purpose of transmitting the analogue signals, since the dispersion of the signal flattens the leading edge and hence smears the timing information. Apart from slight differences in amplitude, which are partially due to the PMT statistics but also due to the wire resistance, all other cables could be used. Table 4.4 shows the leading and trailing edge timing (10-90%) for the different cables, measured and determined with the scope.

Producer	Shielding	Length [m]	L$_\searrow$ [ns]	M$_\searrow$ [ns]	H$_\searrow$ [ns]	L$_\nearrow$ [ns]	M$_\nearrow$ [ns]	H$_\nearrow$ [ns]
Wirewin	UTP	5	7.4	11.6	14.1	41.0	24.8	16.1
Wirewin	UTP	15	12.9	17.2	24.4	41.2	37.6	29.3
Wirewin	UTP	25	19.6	23.7	34.5	47.4	49.2	41.4
Wirewin	S/FTP	15	5.1	*11.9	*21.5	43.0	32.5	20.1
Daetwyler	S/FTP	15	5.4	9.3	14.7	43.1	35.8	22.2
Daetwyler	S/FTP	25	6.0	*12.9	*20.8	42.5	33.6	21.5

Table 4.4: Leading ($\searrow$) and trailing ($\nearrow$) edge times (10-90%) for low (L), mid (M) and high (H) intensity signals. * The signal starts to roll off after about 60% of the leading edge time. A good time resolution should still be possible, since the edge is steep enough beforehand.

The measurements suggest that using long cables for the transmission of the analogue signals is possible, but this would need more thorough studies to check, for example, differences between cable batches, etc. The slimpatch cables, as produced by Wirewin, are preferred due to their low weight and the small space consumption, but there might be the need to use the shielded version of the slimpatch cables.

4.7 The photo-detector-plane (PDP) board

The photo-detector-plane includes the photo-detector, in this case PMTs, the signal amplifier circuit, the high-voltage generation and some slow control. The first PDP board is a single pixel board including the PMT, the amplifier circuit and the passive PMT base. The HV is supplied externally to allow a quick adjustment and to minimize the complexity of the single pixel board. Two versions of such single-pixel boards have been developed to host a Photonis XP2960 and a Hamamatsu R11920 PMT, respectively. A larger board with 12 pixels has been developed by A. Vollhardt at the University of Zurich, following the validation of the single pixel PDP board.

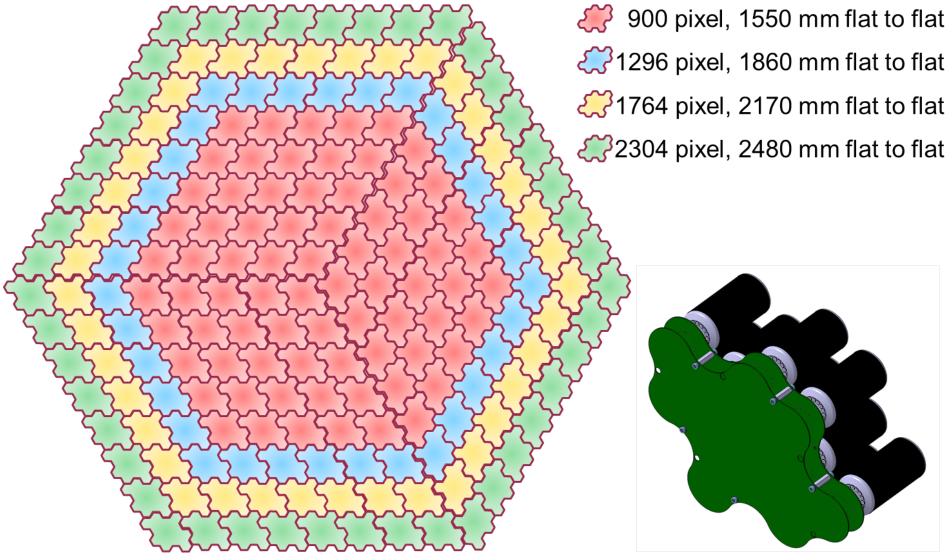

Figure 4.28: Sketch of a PDP board with assembled PMTs (bottom right) and the geometrical configuration of rotated PDP boards to a hexagonal camera with three sectors.

This board has been stress tested and, after some improvements, been redesigned to the final PDP board.

4.7.1 The photo-detector plane geometry

The geometry of the PDP board is such that it can host 12 PMTs and be arranged in a modular way, allowing the size of the camera to be changed to the needs of the telescope design. T. Kihm introduced the shape shown in figure 4.28. Assembling such boards, rotated by 0, 120 and 240°, as shown in the figure, results in a hexagonal camera with three sectors. A fully assembled PDP board including PMTs, weighs about 1.1 kg and has dimensions of about 250 mm width, 180 mm height and 130 mm depth.

4.7.2 The photo-detector plane design

Figure 4.29 shows the first version of the 12-pixel PDP module. The 12 PMT pixels are grouped in four to feed one CAT5 or CAT6 cable each. The high voltage and the preamplifier gain can be adjusted for each PMT individually. The negative power supply voltage for the preamplifier can commonly be adjusted to set the clipping level and the voltage range of the amplifier output. All parameters can be read out and controlled via a CAN

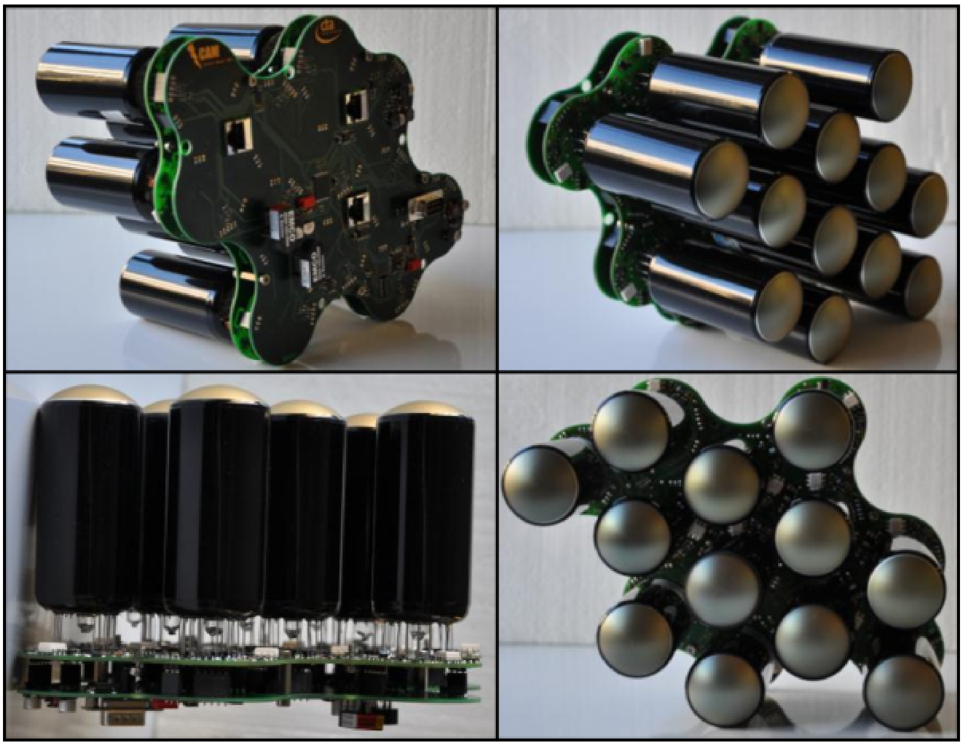

Figure 4.29: Photo of the photo-detector plane assembled with 12 Hamamatsu PMTs. The three RJ45 plugs to connect the CAT6 cables are visible on the top, left photo. The DSUB-9 connector on the bottom edge of the PDP is used as CAN bus interface and for the 24 V power supply.

bus interface. The slow control measures and reads out the implemented temperature and humidity sensor, as well as the HV and the PMT (anode) current. A Labview program enables the reading and setting of the slow control values.

The high voltage is generated with two EMCO modules of 500 V (A05N-24) and 1500 V (A15N-24). The former serves the last three dynodes and the latter the cathode and the first five dynodes. This splitting of the voltages has the advantage of reducing the power consumption compared to a single power supply, which would have to feed the whole passive resistor divider. A new design by D. Florin with Royer oscillators could reduce the costs of the HV generation and decrease the high frequency noise introduced by internal oscillators of the EMCO modules. The PDP is designed as a sandwich with two boards, one being connected to the PMTs, integrating the active voltage divider (the circuit is shown in appendix A.3, the high voltage control and the amplifier circuit with the RJ45 connectors. The second board hosts the slow control with ADCs and DACs to set and measure the amplifier gain, PMT current and voltage, temperature and humidity. A micro controller is used for the slow control and a special CAN bus control chip handles the communication.

The mechanical separation of the digitization electronics and the PDP modules has several advantages. The main advantage is surely that the same digitization electronics can be used with different photo-detectors and photo-detector electronics. Even a mixture of several different front-end systems is possible, as long as the mechanical and electronic interfaces fit. Another very important aspect is the cooling and temperature stabilization of the PDP electronics. Most designs with a mechanically combined photo-detector and digitization electronics are rather awkwardly shaped and the dissipation of heat is difficult. In the FlashCam concept, the power hungry digitization electronics can be placed in crates, being temperature stabilized with commercial cooling systems. Another advantage of separating the heavy digitization electronics from the more light-weight PDP is the possibility of distributing the weight inside the camera housing or to even place the heavy crates outside the camera, in the telescope's tower for instance.

4.8 The 144-pixel camera

The idea of the 144-pixel camera is to demonstrate of concept of FlashCam with a larger number of channels connected to the digitization electronics. The 12 PDP boards are already assembled, tested on their basic functions and mounted in an aluminum frame (figure 4.30). The costs haven been reduced by using only 36 Hamamatsu PMTs and 108 B-rated Photonis PMTs, kindly provided by G. Hermann and the MPI-K in Heidelberg. The digitization electronics to readout all pixels simultaneously are not yet tested completely and hence not available.

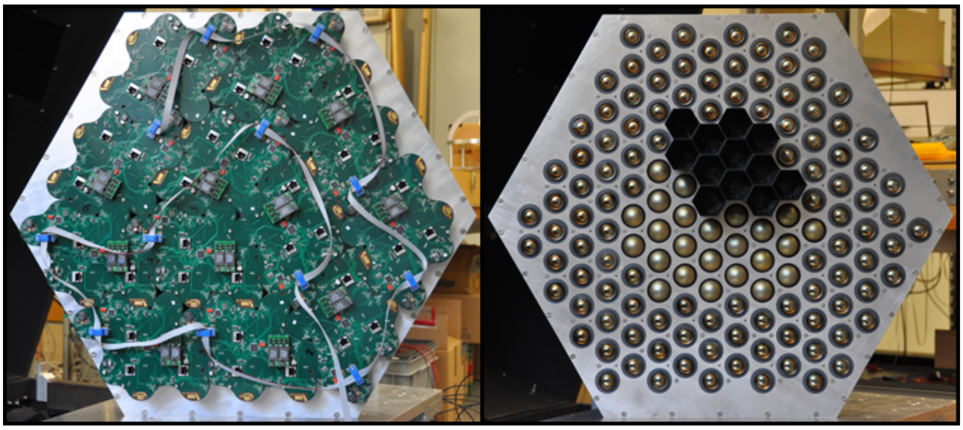

Figure 4.30: 144 pixel camera from the back and from the front with two types of PMTs (inner 36 are Hamamatsu, outer 108 are Photonis) and mounted light concentrator prototype without reflecting foil (right). The CAN bus cable connects all 12 modules.

Chapter 5

Performance of FlashCam

This chapter discusses the calibration and the performance of the FC250 demo board and the amplifier circuit. Two methods to calibrate the PMT gain and performance curves for the whole FlashCam electronics are presented.

5.1 Calibration of the signal path

Calibrating the amplifier circuit and the PMTs is the next step to a fully calibrated signal chain. The calibration of the single FC250 inputs is discussed in section 4.4.2. The temperature calibration is discussed in section 4.3.3.

5.1.1 Amplifier circuit calibration

The amplifier circuit has to be calibrated for different gains and temperatures. The gain of the amplifier is defined as the ratio of the output and the input amplitude of a signal. The external signal is varied while the temperature and the gain are kept constant. This delivers the transfer characteristics of the amplifier that should be linear until it begins to clip the output. Keeping the external signal constant and varying the amplifier gain returns the gain curve of the amplifier circuit. For those measurements, a charge terminator (10.2 pF) is used as input source and the load resistor of 2 kΩ is replaced by a 50 Ω resistor to allow for the connection of the scope with 50 Ω termination. The lower impedance changes the duration of the tail of the signal fed into the amplifier. However, this does not have a big influence on the measurements for gain and signal transfer behavior. The output of the amplifier circuit is connected to the calibrated FC250 board. Figure 5.1 shows the measured amplifier gain as a function of the set gain

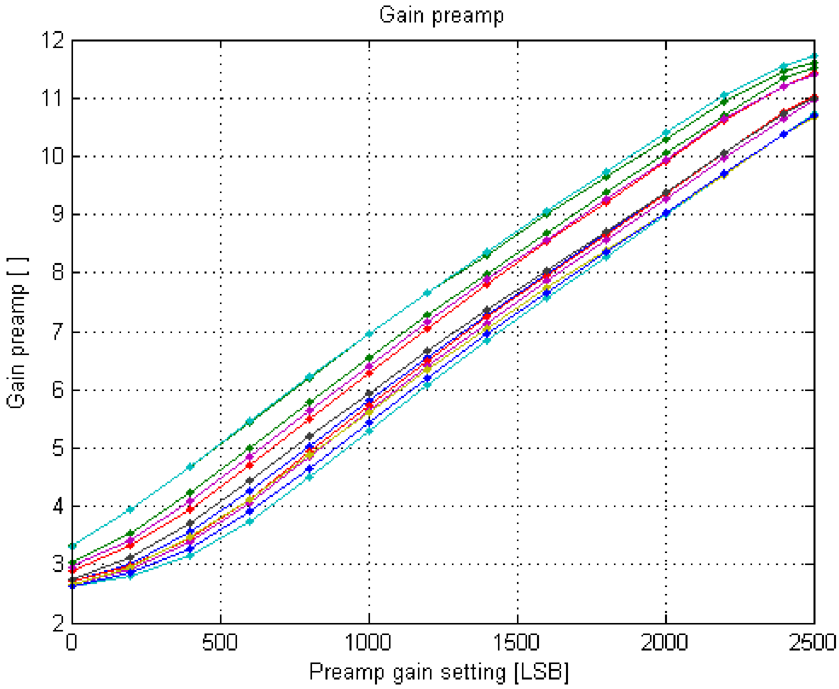

Figure 5.1: Gain of AD8001 circuits of the twelve PDP channels versus amplifier gain setting measured with a fixed input pulse amplitude and gain changed with the FET circuit.

of all twelve channels of the prototype PDP board. The gain setting is done with the Labview tool (0 LSB = low gain, 2500 LSB = highest gain possible) and the values to set the FET circuit sent via CAN bus to the PDP board.
The flattening of some of the gain curves at low gains is due to the too high resistivity of the FET circuits. The FETs have a very high impedance in that region and hence almost do not change the gain resistor anymore (remember that there is a resistor shunting the FET for exactly this case). The flattening at high gains happens because of the amplifier that begins to clip the signal. A controllable and almost linear range of gains for all channels is found between gain 4 and 10.
After knowing the set gain of each amplifier, the transfer characteristic is measured with setting all amplifiers to a Labview value of 1500 LSB (~7.2-8.8 gain) and varying the input pulse amplitude by attenuating the output signal of the pulse generator. The reconstruction of the measured pulse amplitude with the post-processing algorithms described in section 4.5 (pulse peak and pulse area) and the compensation of each channel by the calibration factors is shown in figure 5.2.

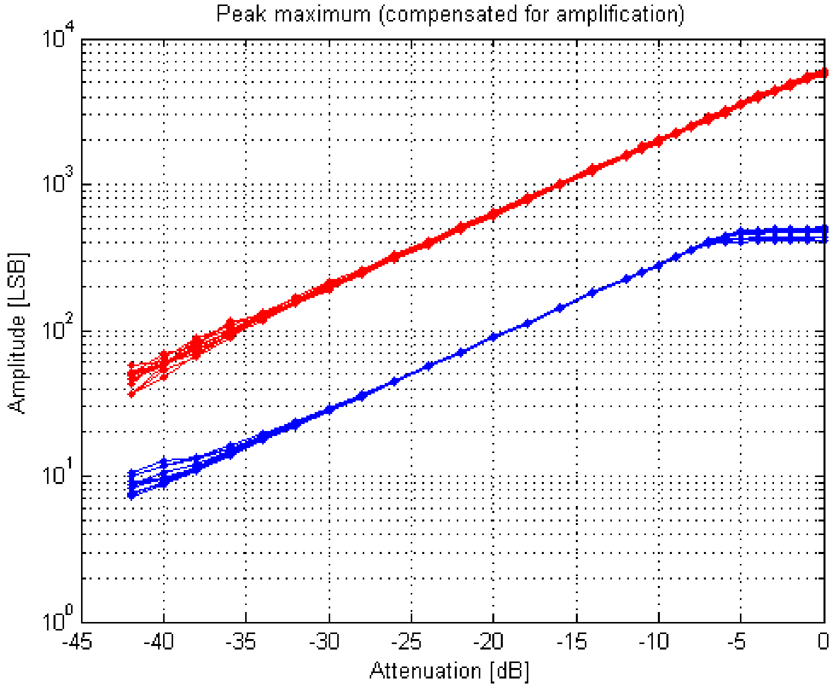

Figure 5.2: Amplifier gain set with Labview at 1500 LSB (~7.2-8.8 gain) and input pulse varied with an attenuator wired in front of the charge terminator (-2 dB per step). The measured and calculated amplitudes are compensated for the gain factors of the individual electronics channels. The upper red curves show the reconstructed pulse area and the lower blue curves the reconstructed pulse peak of the twelve PDP channels.

The deviations at high attenuation values (low pulse amplitudes) is due to difficulties of the amplitude reconstruction caused by large noise contributions. The amplifiers start to clip at slightly different input amplitudes, since they have different gains at 1500 LSB setting value.

5.1.2 PMT calibration

Single photoelectron response method

The gain of the PMT is needed to determine from the PMT's output pulse the number of initial photoelectrons. One way of determine the PMT gain is to measure the single photoelectron response (SER). This can be done with a pulsed light source which in average produces $\ll$1 pe per pulse. Binning the PMT output pulse amplitude or area gives a histogram spectrum with a sharp Gauss shaped peak for the electronics noise (pedestal peak),

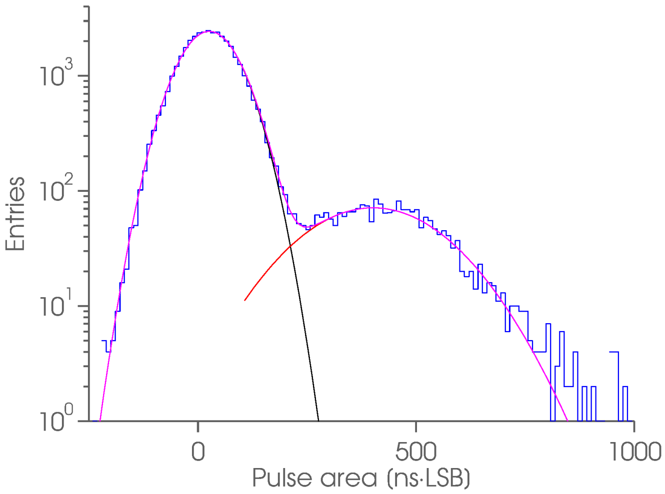

Figure 5.3: Single photo-electron spectrum of a Hamamatsu R11920-100-01 PMT at 885 V supply. The black curve is the fit of the noise area peak, the red curve the fit to the SER signal area and the pink curve the sum of the two fits.

i.e. photon pulses that produce no signal, and a broader peak for the SER and possible multi-photoelectron responses. The mean of the SER Gauss denotes the amplitude of the single photoelectron. This method of SER determination puts all characteristics of the photo-cathode aside, since parameters like the quantum efficiency only affect multi-photon events. The gain of the PMT is given by the multiplication factors of each dynode or simply by the mean SER as

$$\mu_{SER} = Ge \tag{5.1}$$

where μ_{SER} is the mean pulse height of the SER, G the PMT gain and e the elementary charge. The number of photons of a laser pulse is Poisson-distributed and hence a low intensity is necessary to minimize the probability of double, triple, and more photon events in the spectrum. A low light intensity can be reached by attenuating the laser so far that a light pulse contains only about 0.05-0.1 photons or in other words, every 20th pulse emits on average one photon. However, a small contribution of multi-photon events is almost always present due to the Poisson statistics. The probability for having a 1 pe event is about 4.9% and for having a 2 pe already only 0.12% for 95% noise pulses. Figure 5.3 shows a single photo-electron spectrum of a Hamamatsu R11920-100-01 PMT at 885 V (PMT gain corresponds to 3.95x10^4). The noise peak is fitted by a normal Gauss curve and the signal peak by a truncated Gauss T [75] [76]

$$T(A, \mu, \sigma; x) = \theta(x) A e^{-\frac{(x-\mu)^2}{2\sigma^2}} \tag{5.2}$$

with A the normalization factor (amplitude), μ the position of the peak of the truncated Gauss, σ the standard deviation of the normal Gauss, x the bin center (pulse area) and $\theta(x)$ the Heaviside step function.

An event selection is first performed before determining the pulse peak or areas and histogram them. The selection is necessary because the measured events contain pick-up noise and glitches originating from unknown external sources. Neighboring labs in the same building report also the presence of similar noise. This noise contribution broadens slightly the noise peak and makes the determination of the SER difficult without selecting 'noise free' events. The cleaning ejects all events with large negative peaks below the baseline.

A comparison of the mean baseline in a window before and after the signal pulse eliminates events with unstable baseline. The baseline offset is determined after the event selection by calculating the mean of the baseline before the signal pulse of each event. The offset is subtracted from the whole event to eliminate the DC content. The signal and noise amplitude is calculated either by taking the amplitude at a fixed time position referenced to the trigger time, or by calculating the area within a fixed window around the fix time position. The noise is not taken from the same position as the signal but is always taken from data before the signal pulse to eliminate contributions of signal pick-up, ringing, etc. A maximum search, as described in section 3.1.3, is also used but results are not shown here since they do not differ much in comparison to the pulse area evaluation. The fitting of the parameters of the truncated Gauss is done iteratively by minimizing the χ^2 function in MATLAB with the provided function *fminsearch*. χ^2 for a function f is defined as

$$\chi^2(a) \approx \sum_{i=1}^{N} \frac{(n_i - f(x_i|a))^2}{n_i} \tag{5.3}$$

with N the number of bins, n_i the number of entries of the i^{th} bin, x_i the bin center, a the parameter(s) to be minimized and $f(x_i|a)$ the fitting function evaluated at position i. The peak position μ_T and the standard deviation σ_T of the truncated Gauss are not the same as for the normal Gauss and can be calculated as

$$\mu_T = \mu + \sigma\lambda \tag{5.4}$$

and

$$\sigma_T = \sigma \cdot \sqrt{1+\delta} \tag{5.5}$$

with

$$\lambda = \sqrt{\frac{2}{\pi}} \cdot e^{-\frac{\mu^2}{2\sigma^2}} \cdot \frac{1}{1-\mathrm{erf}\left(-\frac{\mu}{\sqrt{2}\sigma}\right)} \tag{5.6}$$

and

$$\delta = \lambda\left(\lambda + \frac{\mu}{\sigma}\right) \tag{5.7}$$

with erf being the error function. The numeric determination of μ_T is

$$\mu_T = \frac{\sum x_i \cdot T(A,\mu,\sigma;x_i)}{\sum T(A,\mu,\sigma;x_i)} \tag{5.8}$$

with the sums running over i. There are two methods used for fitting the data with the χ^2 function: fitting the noise peak first and subtracting the fit from the data, then fit the signal peak of the new data. The second method fits the noise and the signal simultaneously. Both methods give good results with well selected data (only few noisy events survived the selection). Double, triple and more photoelectron events, which contribute to the right side of the spectrum due to the Poisson statistics, can be fitted with additional Gauss curves with $\mu_n = n\mu_{1pe}$ with n being the number of photoelectrons. This relation can also be used to calculate the number of photoelectrons of a peak ($n = \mu_n/\mu_{1pe}$). The probability of measuring single or more photoelectrons in a signal event can be described by the Poisson distribution

$$P_\mu(k) = \frac{\mu^k}{k!}e^{-\mu} \tag{5.9}$$

with k the number of expected photoelectrons and μ the expectation value. μ can be determined by choosing $k = 0$ for having no photoelectrons in an event and hence

$$\mu = -\ln(P_\mu(0)). \tag{5.10}$$

with the probability to have no photoelectrons

$$P_\mu(0) = \frac{N_{\mathrm{Noise}}}{N_{\mathrm{Total}}}. \tag{5.11}$$

N_{Noise} and N_{Total} are the sum of the bin entries in the noise peak and the total number of bin entries, respectively.

Finally, the conversion of the determined pulse mean LSB value of the single photoelectron to the charge delivered by the PMT has to be done, considering the ADC and the whole electronics chain. The determined SER value is first converted into a voltage by dividing it through the resolution of the ADC, $r = 2^{12}$, and multiplying it with the voltage input range of the ADC $U_{ADC} = 1.25\,\mathrm{V}$. The resulting voltage value is divided by the gain factor of the individual FC250 input stages g_{FC250} and the gain of the amplifier circuit g_{amp}. This resulting voltage is the amplitude of the PMT pulse and the current is calculated by dividing the voltage by the load resistor R. The gain of the PMT is hence

$$G = \frac{Q}{e} = \frac{\mu_T \cdot U_{ADC}}{e \cdot r \cdot g_{FC250} \cdot g_{amp} \cdot R} \tag{5.12}$$

with e the elementary charge.

Scaling method

Another method to determine the gain of a PMT is the scaling method. The idea is to measure the SER and hence the gain of a PMT at a higher voltage than the foreseen operation voltage. The SER amplitude is larger and the resulting histogram signal peak can nicely be fitted to determine the mean value of the peak. Another measurement is taken with a higher light intensity (should result in an amplitude of about 10 pe) and the actual number of photoelectrons is determined by the ratio of the new pulse amplitude and the SER amplitude. Reducing the supply voltage to the foreseen operation voltage and taking a measurement with the same light intensity as before, which amplitude is known, leads to the SER amplitude at the new voltage and hence to the PMT gain. This method works well as the lin-log plots for measurements with the higher intensity laser pulse applied to the 12 PDP PMTs in figures 5.4 and 5.5 show.

The measurements have been taken for high voltages of 900 to 1200 V in 50 V steps and for a slightly higher laser intensity for 800 V to 1100 V in 10 V steps and the mean of the measured pulse amplitude (5000 events per voltage setting) is plotted. The difference in amplitude of the channels arise mainly from the different PMT gains but also from the different PMT quantum efficiencies. These differences have to be compensated in an IACT camera by adjusting the high voltages and hence the gains such that each PMT gives about the same pulse amplitude for the same light yield.

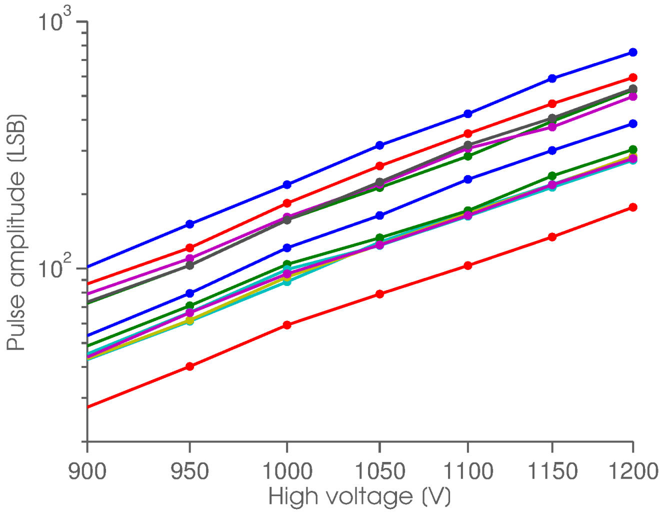

Figure 5.4: Lin-log plot of the mean pulse amplitude of the 12 PDP PMTs with different high voltages.

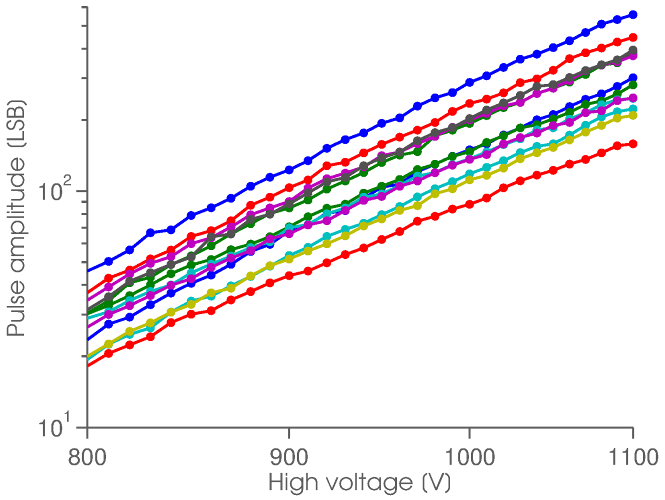

Figure 5.5: Lin-log plot of the mean pulse amplitude of the 12 PDP PMTs for the voltage range of 800 to 1100 V. Measured with a slightly higher light intensity to get a good signal at the low end of the voltage (low PMT gain).

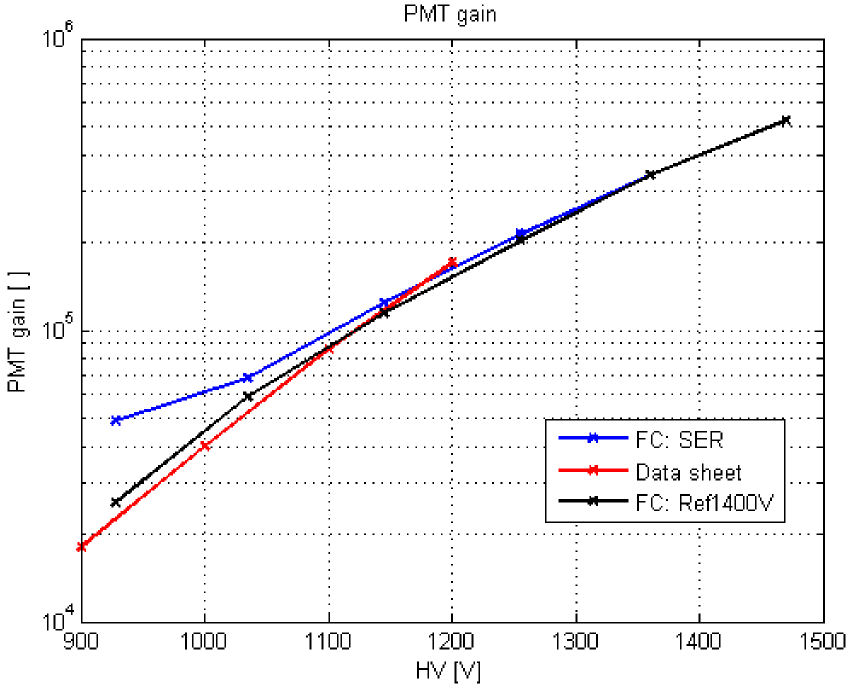

Figure 5.6: Measured PMT gain determined by the SER method (blue) and by the scaling method (black, SER calibration done for 1400 V). The red curve shows a typical curve of a Hamamatsu R11920 PMT.

Figure 5.6 shows the two methods used to determine the PMT gain. The gain determined by the SER determination is shown in blue. This method worsens towards low gains as the electronics noise starts to contribute significantly. The scaling method in black has been calibrated at 1400 V and shows a better performance for low PMT gains.

5.1.3 12 pixel photo-detector plane SER calibration

The twelve PMTs of the PDP are calibrated by the SER method, described at the beginning of the previous section. SER measurements are taken for various high voltages for each PMT and evaluated by the pulse area (search maximum in window and integrate signal over a window of -3 and +15 samples around maximum). The PMT gain is then calculated from the SER peak amplitude in function of the HV and a curve is fit to the data. The HV for a gain of 40000 is determined with the fit function. Figure 5.7 shows the SER histograms for a PMT gain of 40000 determined by the pulse area. Table 5.1 summarizes all important parameters of the PMTs calibration.

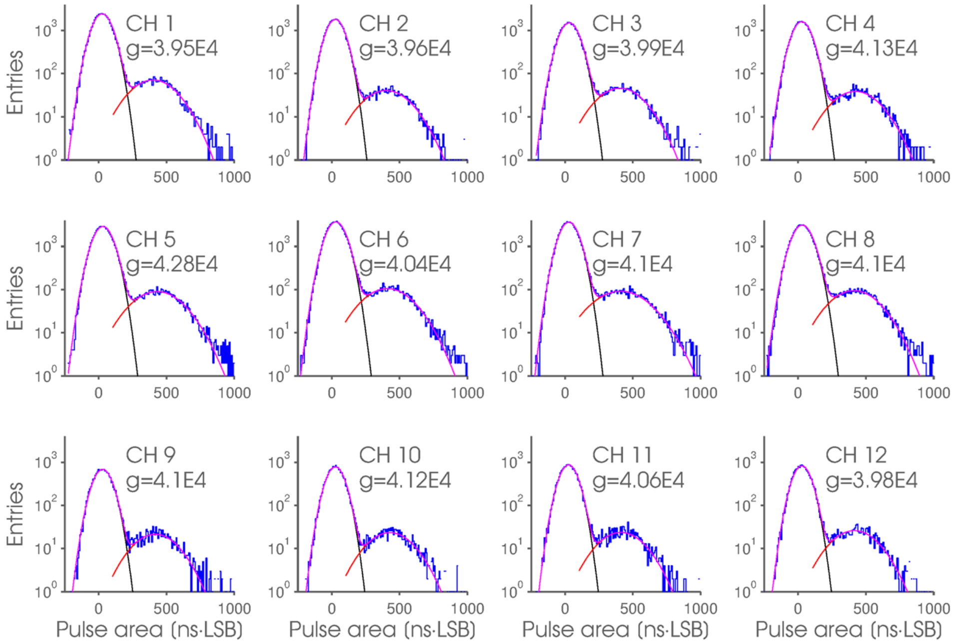

Figure 5.7: SER spectra of the Hamamatsu PDP PMTs with adjusted HV for an average gain of 40000. All amplifier gains are set to 10, which gives an average SER amplitude of about 18 LSB. The red curve indicates the fit of the truncated Gauss, the black curve is the Gauss fit to the noise and the pink curve is the sum of the two fits.

PMT	HV [V]	Amplifier gain [LSB]	Light yield	SER amplitude $\pm\sigma$ [LSB]	χ^2/ndf signal	PMT gain [10^4]
1	885	2266	1/18	18.5 ± 5.7	1.3	3.95
2	855	1998	1/21	18.1 ± 5.4	0.9	3.96
3	830	2266	1/17	17.8 ± 5.5	1.0	3.99
4	925	2358	1/19	19.1 ± 5.8	1.2	4.13
5	843	2316	1/15	17.6 ± 5.2	1.4	4.28
6	905	2375	1/17	17.1 ± 4.9	1.8	4.04
7	850	2290	1/17	18.5 ± 5.9	1.6	4.10
8	820	2400	1/17	17.2 ± 4.8	1.6	4.10
9	880	2074	1/15	18.2 ± 5.8	1.2	4.10
10	975	2048	1/15	19.2 ± 5.9	1.0	4.12
11	900	1973	1/16	18.3 ± 5.5	1.3	4.06
12	903	2032	1/15	18.4 ± 5.5	1.0	3.98

Table 5.1: Gain calibration of the PDP PMTs. The light yield is given in detected signals per triggered events. The amplifier gain settings correspond to a gain of 10. The σ of the SER amplitude gives the truncated Gauss width, mainly dominated by the statistics of the PMT and *ndf* is the number of degree of freedom (number of measurement points minus number of fit parameters) of the fitted truncated Gauss function.

5.2 Performance of a single pixel FlashCam

A single pixel board with an AD8001 amplifier connected via a 5 m CAT5 cable to a FC250 board is measured first with a charge terminator as input source (figure 5.8) and later with a real PMT. The output pulses are evaluated to determine the amplitude and time resolution, as well as the reconstructed amplitude and time accuracy that are achievable with the FlashCam electronics using the developed linear-nonlinear amplifier and the post-processing algorithm. The measurements with the charge terminator and the analysis have kindly been provided by T. Kihm. The measurements with the real PMT are presented at the end of this section.

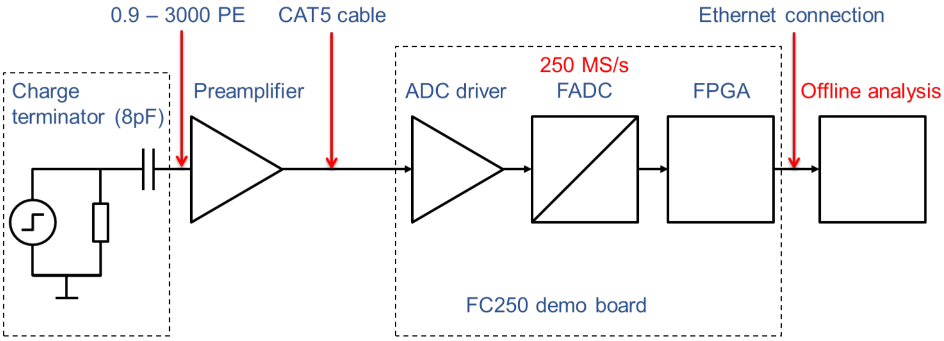

Figure 5.8: Setup for verification of the FC250 demo board at MPI-K Heidelberg. A pulse generator is used together with a charge terminator with the same capacity as a Photonis XP2960 PMT (~8 pF).

Figure 5.9 shows an up-sampled and smoothed 10 pe signal (black curve) with the post-processed curves for the time (red curve) and amplitude (blue curve) extraction. The curve for the pulse maximum determination is further smoothed with three moving average filters (pink curve) to increase the signal to noise ratio for low amplitude signals. The amplitude determination from the pink curve gives more precise results than the extraction of the amplitude from the blue curve since more signal is integrated and hence the signal to noise ratio increased. The better performance of the reconstructed amplitude from the integrated pulse can be seen over the whole linear range of the amplifier.

A measured signal of a ~1000 pe pulse is shown in figure 5.10 with the same post-processed curves as figure 5.9. The clipped amplitude curves (blue and pink) are however not used for the amplitude determination, as mentioned in section 4.5.1. The up-sampled and smoothed signal (black curve) is integrated over a window of 200 ns to get the pulse area, instead.

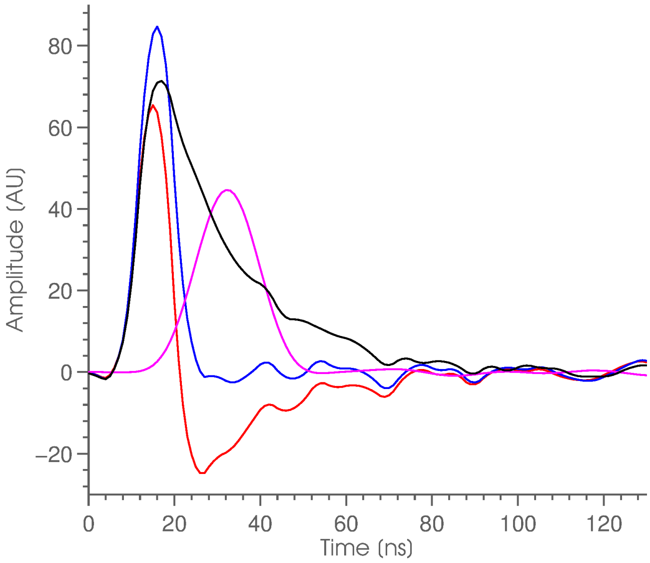

Figure 5.9: Example of a digitized, up-sampled and smoothed signal of about 10 pe amplitude (black). The differentiated signal is shown in red, the undershoot corrected signal for the amplitude extraction in blue and a further smoothed signal in pink. Plot kindly provided by T. Kihm.

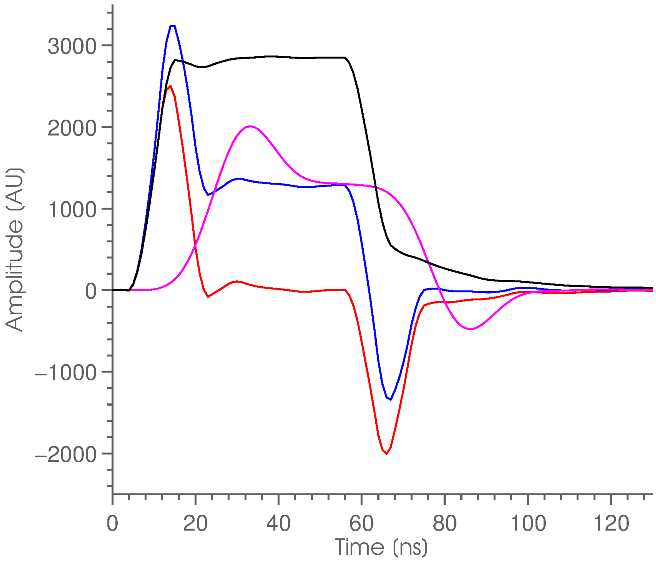

Figure 5.10: Example of a digitized, up-sampled and smoothed signal of about 1000 pe amplitude (black). The differentiated signal is shown in red, the undershoot corrected signal for the amplitude extraction in blue and a further smoothed signal in pink. Plot kindly provided by T. Kihm.

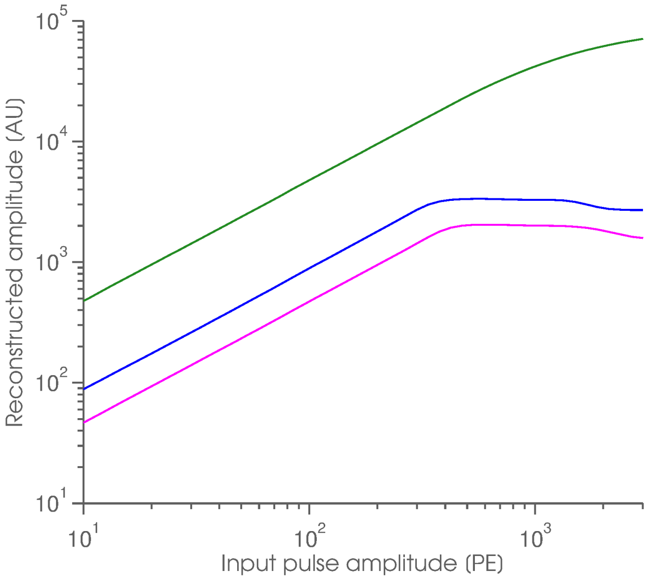

Figure 5.11: Reconstructed output amplitude versus input amplitude for the pulse maximum search (blue and pink) and the pulse integration (green). Plot kindly provided by T. Kihm.

The results of the amplitude determination of a measurement over the whole amplitude dynamic range of up to 3000 pe is shown in figure 5.11. The pulse maxima curves flatten as the amplifier begins to clip and drop even slightly at the end of the dynamic range due to input clipping of the amplifier (output signal dips a bit as the input stage saturates). The pulse area curve flattens also a bit at the end of the range due to the dipping of the signal. Figure 5.12 shows a zoom into the lower amplitude range up to 100 pe in a linear-linear plot. All three curves show a good linearity of the signal transmission and the signal reconstruction.

The amplitude resolution for the three amplitude extraction methods is shown in figure 5.13. The pulse area shows a resolution of about 0.3 pe for up to ~300 pe input pulses and worsens slightly towards higher input amplitudes. The resolution of the undershoot corrected signal (blue) starts already at about 20 pe to be worse than the pulse area reconstruction resolution. Integrating the signal further by applying more SMAs (pink) leads to a slightly better and stable resolution of about 0.12 pe for up to ~60 pe pulses. Both pulse maximum curves lose their resolution completely with the beginning of the amplifier clipping at ~300 pe.

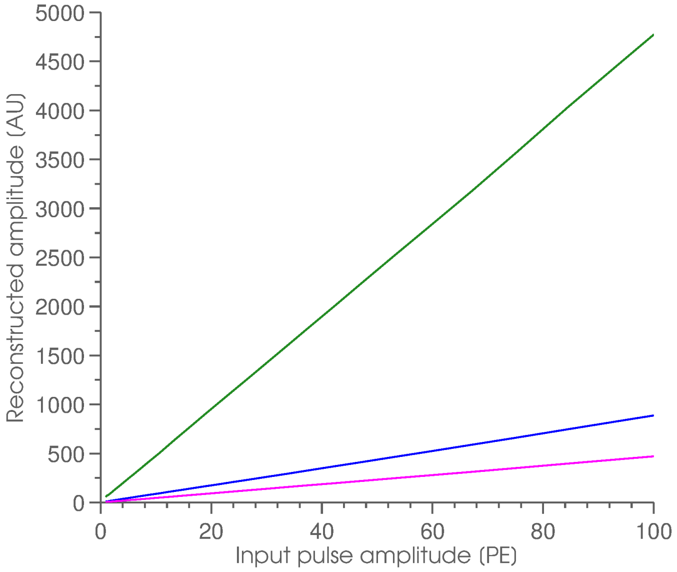

Figure 5.12: Zoom in of figure 5.11 with input amplitudes ≤100 pe in a linear plot. Plot kindly provided by T. Kihm.

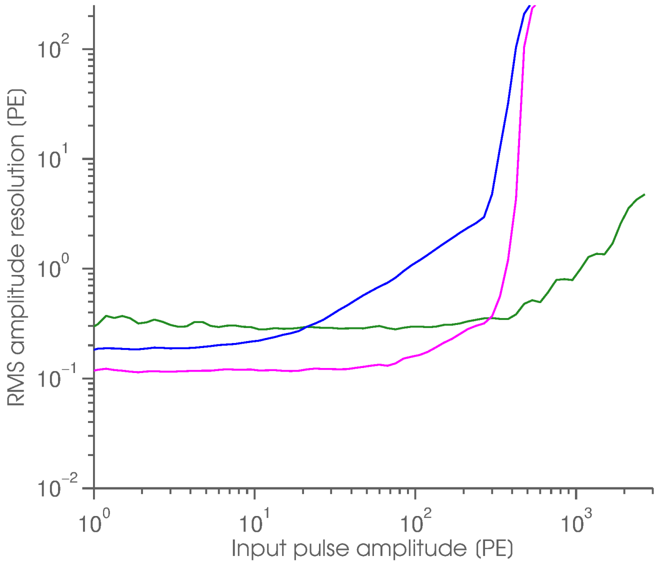

Figure 5.13: RMS resolution of the reconstructed amplitude for the three amplitude extraction methods of pulse area (green), pulse maximum of the undershoot corrected and the further smoothed signal (blue and pink). Plot kindly provided by T. Kihm.

Figure 5.14 shows the time resolution over the whole amplitude dynamic range. Resolutions in the subnanosecond regime down to about 700 ps are achievable. The time resolution is slightly better in reality, because the reference time, the trigger signal, already introduces a jitter of ±100 ps and hence worsens the measured time resolution.

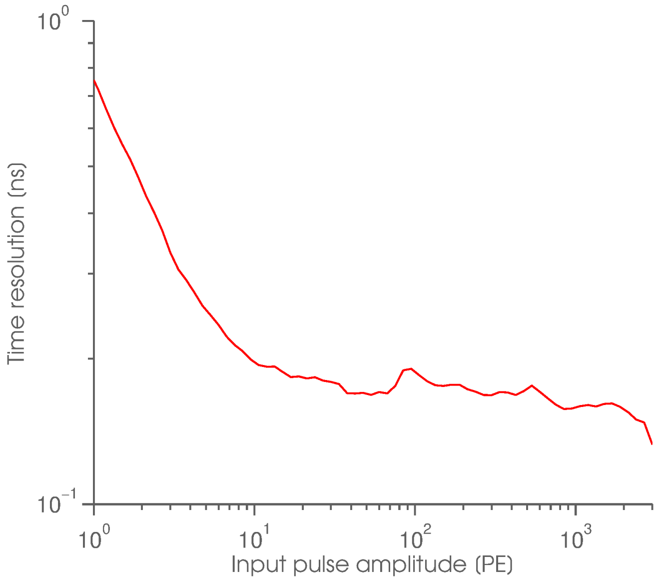

Figure 5.14: Time resolution of single pixel board together with FC250. Plot kindly provided by T. Kihm.

Figures 5.15 and 5.16 show the simulated and measured amplitude and time resolution, respectively. The measurements are done with a Hamamatsu R11920-100-01 PMT mounted on the PDP module and the FlashCam electronics. A laser with attenuator filters as described in section 6.1.1 is used as pulsed light source and a filament bulb is used for the NSB simulation. The largest systematic error contribution arises from the calibration of the attenuator filters (~10%) and is not shown in the first plot. The simulated time resolution (green) deviates for input amplitudes >10 pe. Adding the jitter of the trigger unit and the FC250 of about 250 ps makes the simulation converge to the measurements, but still not meet them. The slightly worse resolution of the measurements could be caused by a larger transit time of the PMT than simulated.

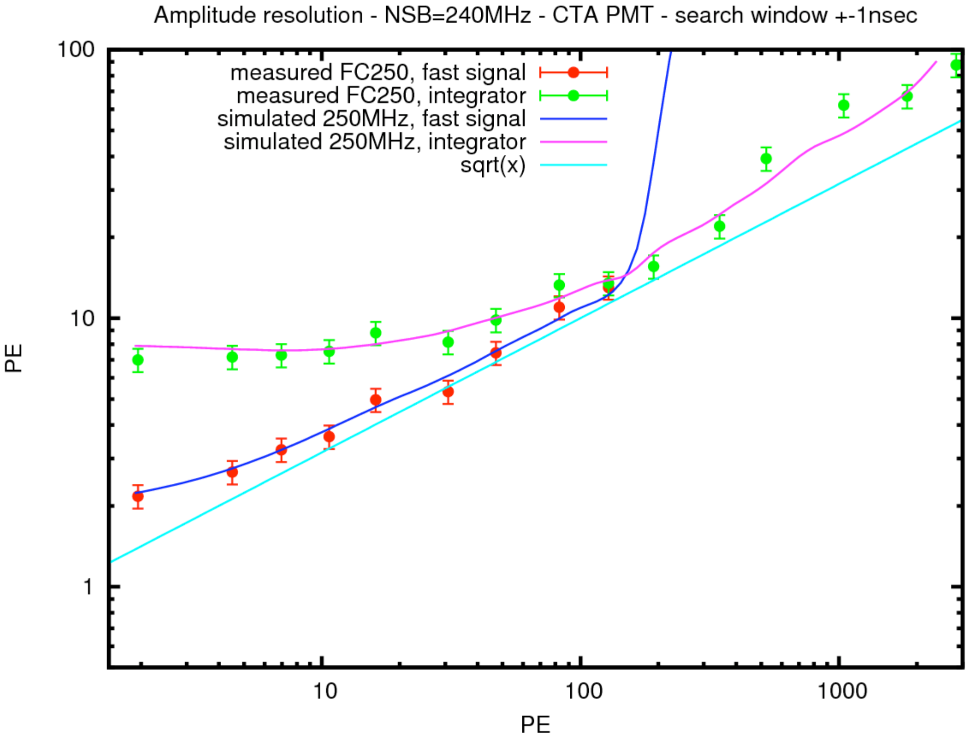

Figure 5.15: Amplitude resolution versus PMT output amplitude at 240 MHz NSB in a comparison of simulation (T. Kihm) and measurements (A. Gadola). The amplitude is determined by the pulse peak (red, blue) and by the pulse area (green, pink). The cyan curve shows the lowest possible resolution given by the Poisson statistics. Plot kindly provided by T. Kihm.

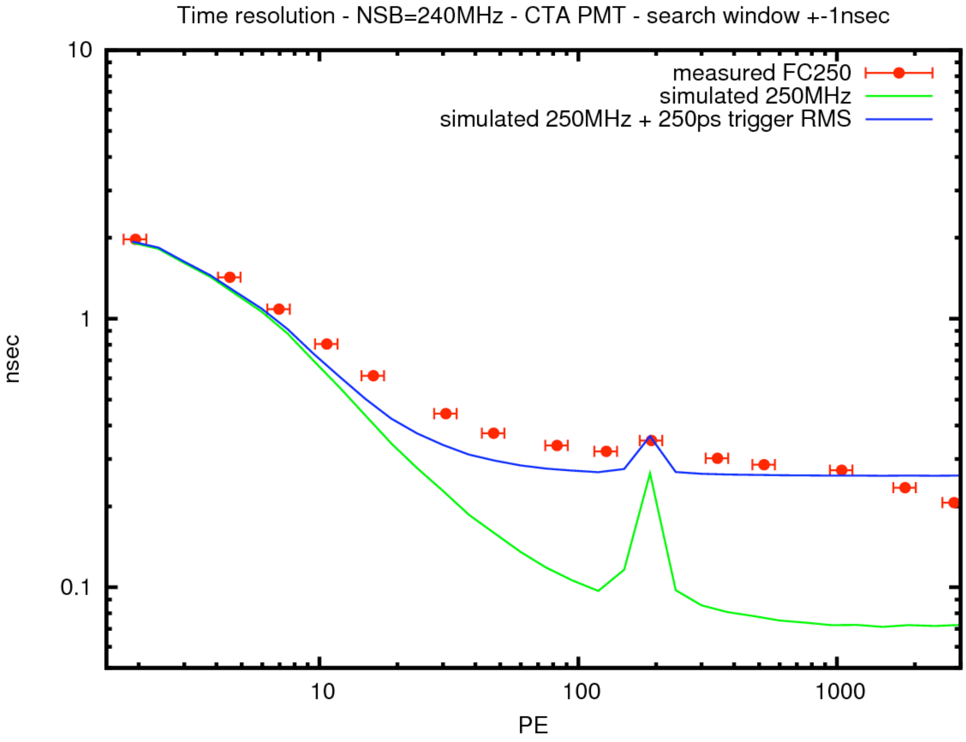

Figure 5.16: Time resolution versus PMT output amplitude at 240 MHz NSB in a comparison of simulation (T. Kihm) and measurements (A. Gadola). The simulation converges towards the measurements by adding a 250 ps jitter of the trigger to the simulation. The bump at about 200 pe indicates the beginning of the amplifier clipping. Plot kindly provided by T. Kihm.

5.3 Performance of the PDP board

The performance of the twelve-pixel PDP board over the whole amplitude dynamic range of up to 3000 pe has been measured with the laser and the Hamamatsu PMTs installed on the PDP board. The time and amplitude resolution of the system, as shown in section 5.2 for the single pixel, has not been determined for the 12-pixel PDP. The setup for the measurements is such that all PMTs are set at a gain of ~40000 and the amplifiers at a gain of 10 (see table 5.1 for actual settings). The measurements for the amplitude dynamic range are performed without NSB.

5.3.1 Amplitude dynamic range measurements

All twelve PDP channels have been measured after calibration of the PMT gain and the electronics chain one by one with the same laser-pulse intensities. The applied laser intensity is first measured with one channel, converted into photoelectron amplitude and is referred to as input amplitude for all measurements. It has an uncertainty of about 10% comming mainly from the determination of the attenuation filters. The measured pulses are analyzed either by their pulse amplitude or pulse area, as describe previously. For the plots, the pulse amplitude and area are converted into a photoelectron equivalent amplitude taken into account the actual PMT gain and electronics gain.

Figure 5.17 shows the measurement of all channels with the pulse amplitude determined by the pulse maximum of the undershoot-corrected signal. The linear-nonlinear amplifier starts to clip at about 200 pe. Figure 5.18 shows a log-log plot of the determined pulse amplitude by evaluating the pulse area for all twelve channels. A slight flattening of the curves above 800 pe is visible but the amplitude information can still be extracted, since this flattening is reproducible. A zoom into the lower-amplitude regime of $\lesssim$240 pe in a linear-linear presentation for all twelve channels and for both the pulse maximum and pulse area evaluation, are shown in figures 5.19 and 5.20. The pulse maximum curve of channel 1 starts already to flatten before the other channels, probably due to the higher QE of the PMT. Hence, larger pulse amplitudes for the same light yield drive the amplifier earlier into clipping. The drifting apart of the channels reflects the uncertainties in the PMT gain determination and the different quantum efficiencies of the PMTs. However, more important than the absolute amplitude is the linearity of the measured curves, since the amplitudes can always be adapted as long as the normalization factors are reproducible.

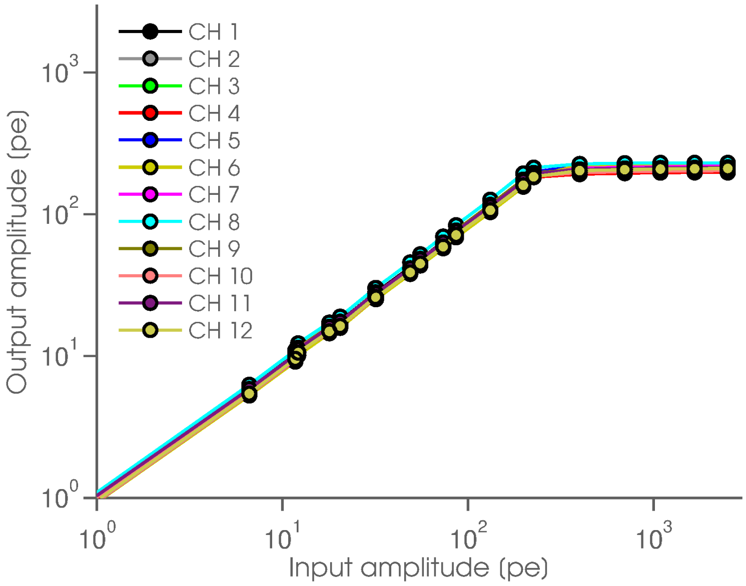

Figure 5.17: Log-log plot of the output amplitudes (dots) of the 12 PDP PMTs. The amplitude is determined by searching the maximum in a fixed window of 40 samples. The amplifiers start to clip at about 200 pe input amplitude.

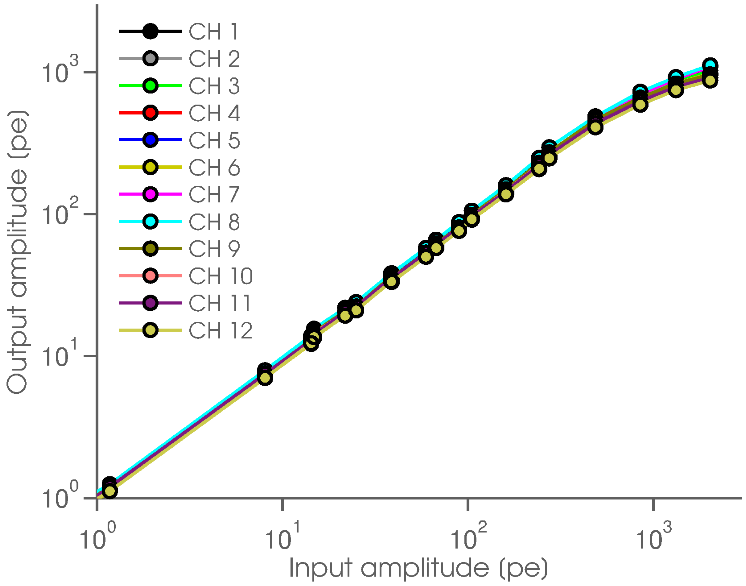

Figure 5.18: Log-log plot of the output amplitudes (dots) of the 12 PDP PMTs. The amplitude is determined by calculating the pulse area with an integration over a fix window of -3 and +15 samples around the found peak maximum. The amplifiers start to clip at about 200 pe input amplitude.

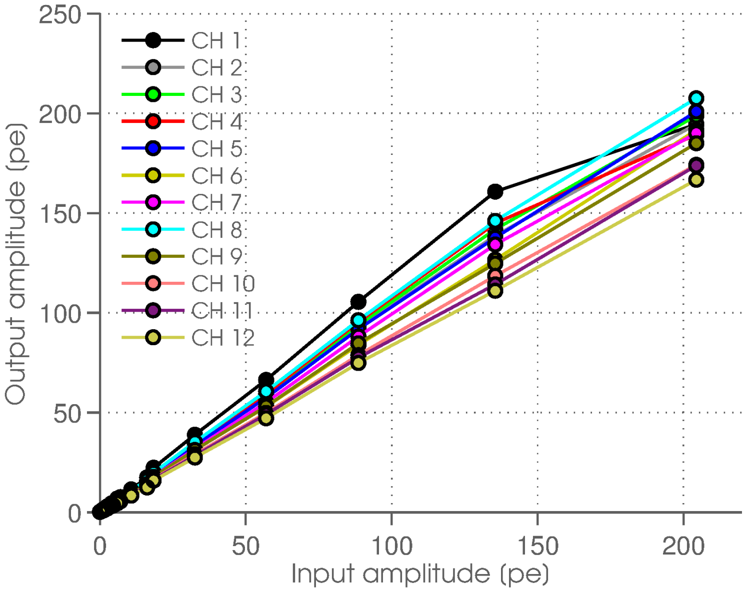

Figure 5.19: Zoom in of figure 5.17, plotted linear in both axes. The drifting apart of the data (dots) towards higher input amplitudes is mainly due to PMT gain uncertainties and the different QE of the PMTs. The amplifier of channel 1 saturates earlier probably due to a higher QE of the PMT than the other channels and hence flattens already before ~200 pe input amplitude.

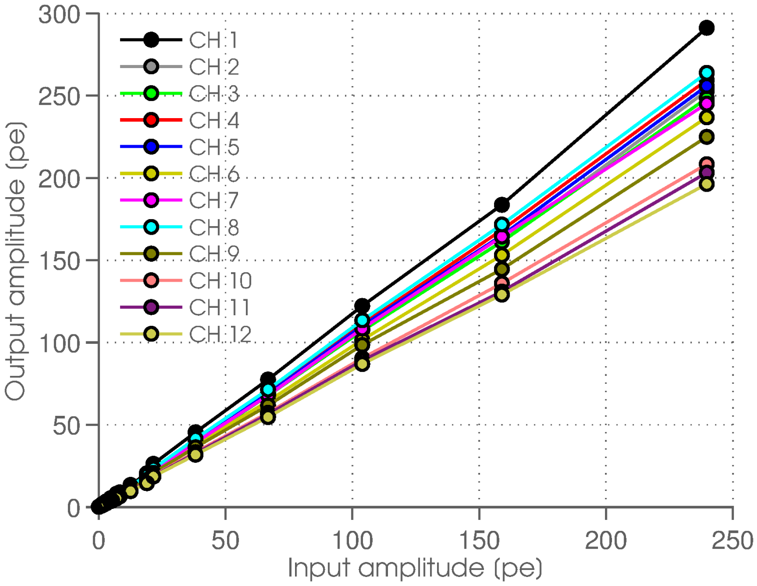

Figure 5.20: Zoom in of figure 5.18, plotted linear in both axes. The running apart of the data (dots) towards higher input amplitudes is mainly due to PMT gain uncertainties and the different QE of the PMTs.

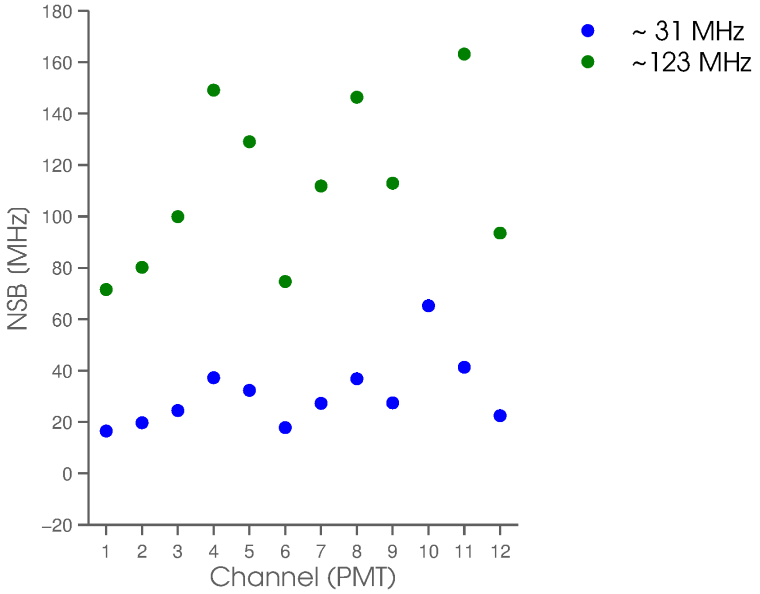

Figure 5.21: NSB measurements with a filament bulb and the fully populated PDP board. The NSB light produced by the filament bulb illuminates all PMTs evenly. The legend shows the mean NSB frequency taken over all twelve PMTs.

5.3.2 Night sky background measurements

The NSB measurements done with the single-pixel electronics were all done with a filament bulb operated at very low intensities. The bulb spectrum peaks at about 750 nm in the reddish with almost no contribution in the blue regime (see figure 6.1). The quantum efficiency of the Hamamatsu R11920-100 PMT above 650 nm is only a few percent and varies by almost 100% from PMT to PMT. The variations in QE are of no relevance as long as single PMTs are measured and the NSB rate is adjusted accordingly. However, a comparison of multiple PMTs on their NSB behavior is very difficult, as the QE variations influence the measurements too much. The individual channels vary, as expected with up to ~100% in the worst case (figure 5.21). Changing the NSB light source to a blue LED with a smaller frequency spectrum, which peaks at ~420 nm where the PMT QE varies from PMT to PMT only by about ±3% for the first Hamamatsu batch and about ±1.5% for the second batch[1] leads to more comparable results, as figure 5.22 shows. Figure 6.1 in section 6.1.2 shows the spectrum of the LED, the

---

[1] QE measurements have been performed at MPI Munich for R11920-100-01 and R11920-100-02. Results are only available for CTA members.

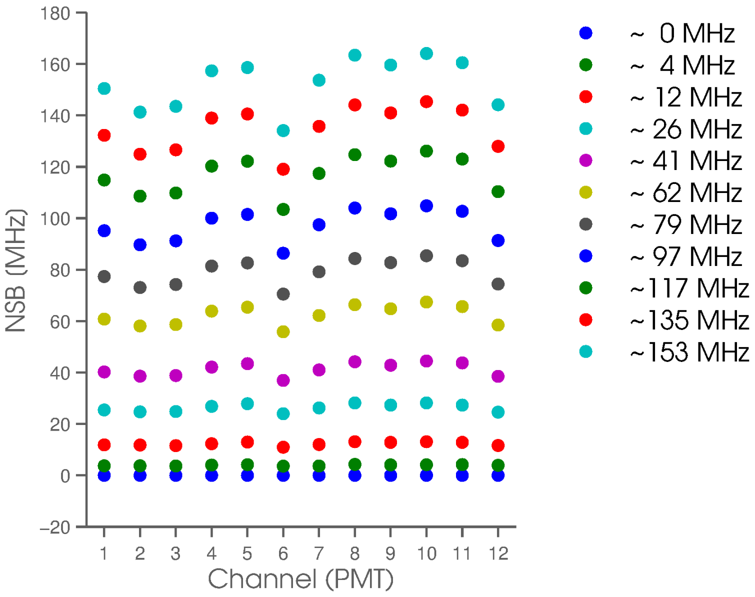

Figure 5.22: NSB measurements with a blue LED with the fully populated PDP board. The NSB light source illuminates all PMTs evenly. The legend shows the mean NSB frequency taken over all twelve PMTs.

bulb and a typical QE curve of the Hamamatsu R11920 PMT. The variations between the single PMTs come mainly from the different quantum efficiencies of the PMTs. The NSB rate is determined for each PMT individually by calculating the area under each measured event waveform and divide it by the area of the single photoelectron pulse. The mean value of all these calculated NSB rates is shown in the plots as legend.

The measurements with NSB generated by a single light source could be used for a flat-field calibration of the camera where the high voltages are adjusted such that all PMTs deliver the same NSB rate.

5.3.3 Crosstalk

The electronics crosstalk of signals between channels has been measured with the full electronics chain, including the PMTs and different CAT6 cables. The crosstalk is defined here as the peak amplitude of the picked up signal, even though the picked up signal look less like PMT signals but more like transients (figure 5.23). The first measurements have been performed with the 5 m unshielded CAT6 cables from Wirewin and later changed to shielded types to identify the best cable with the lowest crosstalk. The setup is such that the laser points to one PMT at a time, optically de-

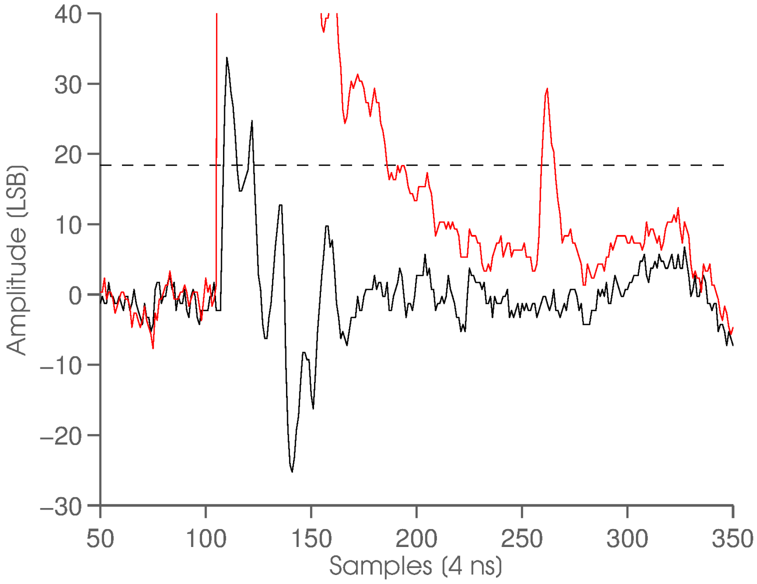

Figure 5.23: Picked-up crosstalk signal from neighboring channels. Channel 5 is illuminated with a laser pulse yield of about 3000 pe (red). The picked-up crosstalk of channel 7 is shown in black. The dashed line marks the 1 pe amplitude. The bump seen in both channels at the right side between about 300 to 350 samples is pick-up noise from an external unknown source (the PMT leads act like antennas).

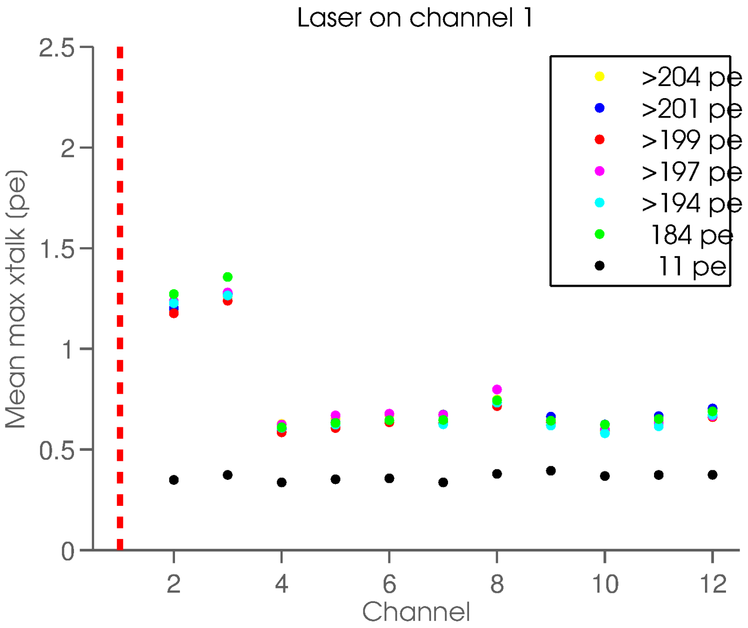

Figure 5.24: Amplitude of crosstalk of channels 2 to 12 with the laser pulsing light on channel 1. No crosstalk but noise is visible for light pulses ≤10 pe. The crosstalk is worst and does not change as soon as the amplifier starts to clip the input signal.

coupled from the remaining eleven PMTs, and its intensity is changed to check for the worst electronics crosstalk on the other channels. All PMTs are operated at gain 40000 and the amplifiers are set to gain 10. Figure 5.24 shows a typical measurement of a crosstalk measurement with the laser on channel 1. The largest crosstalk is noticeable in the channels 2 and 3, whose signals are assigned to the same cable as channel 1. The largest crosstalk is actually always most noticeable in the channels assigned to the same cable as the channel receiving the laser pulse but they never exceed 2.5 pe for unshielded cables (on average <1.5% crosstalk for pulses with >170 pe). This points to the cables being the component with the largest contribution to crosstalk. Changing the cables to shielded pair cables reduced the worst crosstalk to an average of about 1.3 pe over the whole dynamic range. Shielded cables also eliminate the crosstalk completely between the CAT6 cables, compared to unshielded cables. The crosstalk for a 5 m unshielded and a 15 m shielded CAT6 cable is shown in figure 5.25 and 5.26, respectively. No crosstalk is noticeable for signals ≤10 pe, for both cable types. The worst crosstalk measured, introduced by the fast and large transients of the clipped signals, never exceeds 2.5 photoelectrons,

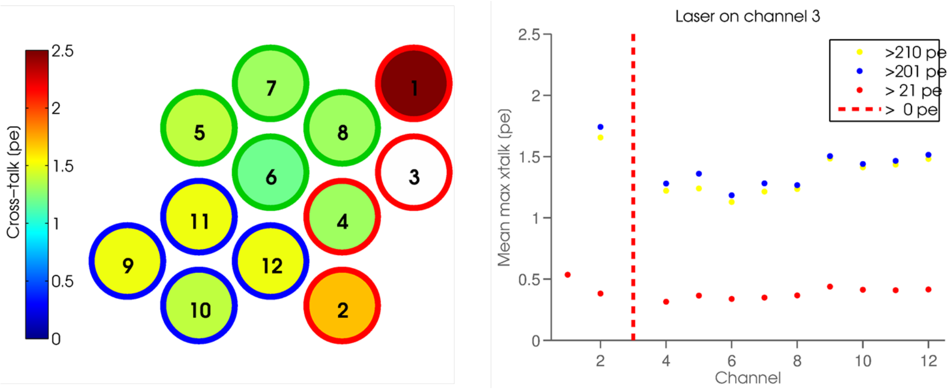

Figure 5.25: Crosstalk for a 5 m unshielded CAT6 cables (Wirewin). The channels 1-4, 5-8 and 9-12 are assigned to a cable each. The laser points to PMT 3 producing about 3000 pe and the colors on the left plot show the crosstalk intensity. The right plot shows the average crosstalk of each channel for different laser intensities.

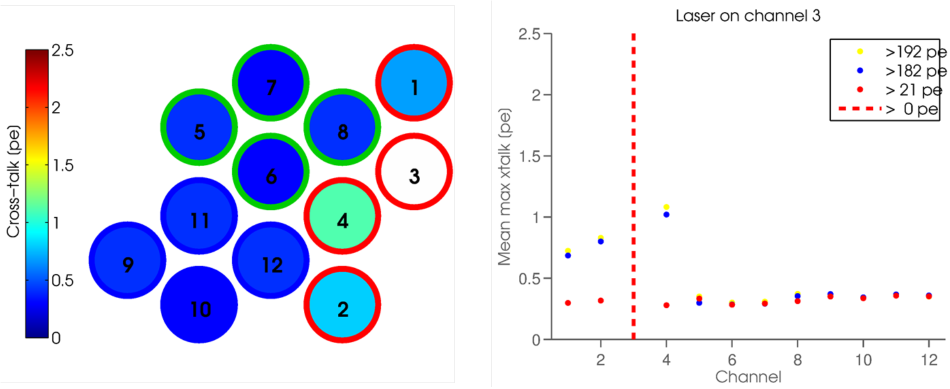

Figure 5.26: Crosstalk for a 15 m shielded CAT6 cables (Wirewin). The channels 1-4, 5-8 and 9-12 are assigned to a cable each. The laser points to PMT 3 producing about 3000 pe and the colors on the left plot show the crosstalk intensity. The right plot shows the average crosstalk of each channel for different laser intensities.

even with unshielded cables. Crosstalk is no problem for FlashCam, given the shape of a Cherenkov light pulse with fading borders and hence not having neighbor pixels with huge differences in signal yield.

5.4 First measurements with silicon detectors

PMTs have the disadvantage to be very expensive and damageable under high light intensities. The former accounts for almost half of the total camera electronics price and hence strongly limits the number of telescopes that can be built with a given budget. The latter limits the time of observation that has to be on very low moon light nights. Replacing the PMT by a cheaper and less damageable detector, as with the MPPC, is desirable. MPPCs have the disadvantages of having a very small active area, compared to the PMTs used in IACTs and of being very temperature sensitive. The temperature coefficient for most Hamamatsu MPPCs is typically 56 mV/K (change of the breakdown voltage) and hence a temperature stability of better than ±1 K is needed for the stable operation of MPPCs. Companies like Hamamatsu are developing MPPCs with larger active areas, but the products are still in their infancy.

One idea of FlashCam, besides its modularity, is the flexibility of being able to exchange the photo-detector part. A new board with the same non-inverting amplifier circuit as used with the PMTs has been designed by D. Florin at UZH. The major difference to the PMT amplifier design is the clipping of the signals on the positive output voltage, instead of on the negative, due to the used MPPC circuit which delivers a positive signal. The Hamamatsu MPPC 10985-050C combines four individual MPPC devices (called channels) with 3600 GAPD cells per device and is used for the first tests. The device is operated around 72 V, slightly above its breakdown voltage to have Geiger-mode operation conditions. Each channel of the device is connected to an AD8001 amplifier circuit with FET gain setting (section 4.3) and to the common bias voltage. Figure 5.27 shows a photograph and a sketch of the MPPC device with its four channels connected to the amplifiers.

Replacing the existing PMT design with a MPPC design, maintaining the pixel size and in addition use the individual amplification per MPPC channel is essentially not feasible for an IACT camera, since the number of needed MPPC to cover the pixel area and hence the number of signal channels and the power consumption would explode.

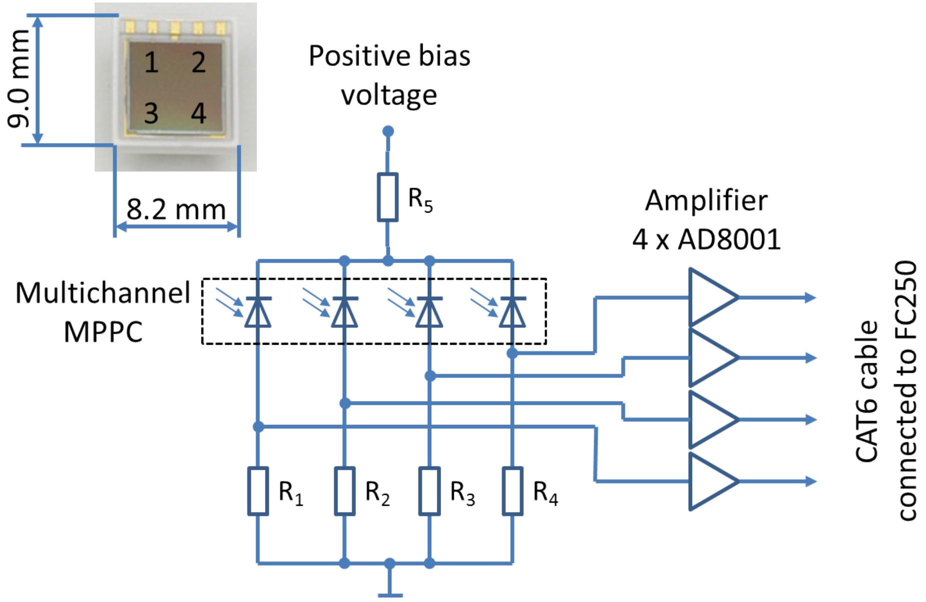

Figure 5.27: Sketch of the four channel MPPC connected to individual amplifiers (AD8001). The amplifier outputs are connected via a CAT6 cable to the FC250 digitization board. The photograph shows an Hamamatsu 10985-050C MPPC device with the four channels labeled.

Figure 5.28 shows a PMT pulse and an MPPC pulse (MPPC signals are summed up with an AD8001 summing amplifier circuit) measured with the FC250 for comparison. Note the time axis scaling in units of 4 ns.

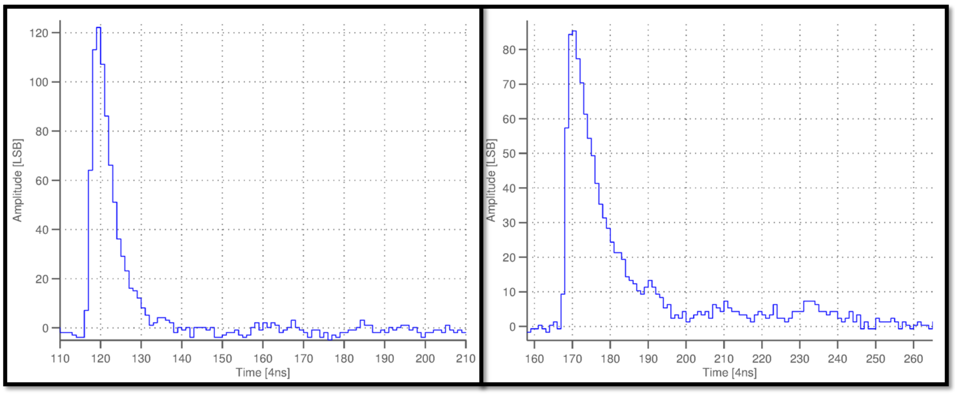

Figure 5.28: Comparison of a PMT (left) and the summed MPPC (right) signal for an arbitrary light yield.

The two measurements are done with different laser intensities. The MPPC pulse has a slightly longer trailing edge due to the larger capacitance of

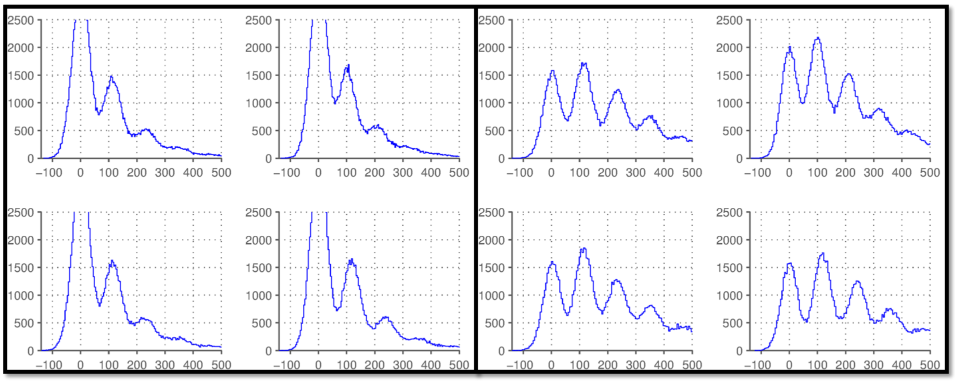

Figure 5.29: MPPC #230 in single channel mode. Bias voltage is (72.257 ± 0.003) V. Shown are measurements for two different light intensities (left plot and right plot).

the device (~320 pF per channel) and hence compels the adjustment of the load resistor (33Ω per channel) and of the pole-zero cancellation parameter to prevent under or overcompensation of the undershoot introduced by the differentiation. However, the PMT and MPPC pulses match each other very nicely otherwise, especially their leading edges are very alike. Two MPPC devices have been measured to analyze the effect of bias voltage matching of the four individual channels. The breakdown voltages of the two devices are listed in table 5.2.

Channel	Serial # 230 Breakdown voltage [V]	Serial # 233 Breakdown voltage [V]
1	72.04	72.35
2	72.09	72.35
3	72.14	72.35
4	72.17	72.36
ΔU	0.13	0.01

Table 5.2: Breakdown voltages for Geiger-mode operation for the single MPPC channels. ΔU specifies the largest difference of the four breakdown voltages.

The four channels of the #230 are not matched very well in their breakdown voltages, which leads to different gains and hence different output amplitudes for the same light yield. Figure 5.29 shows the spectrum taken with the #230 MPPC for the single MPPC channels for different light intensities. The spectra show a good distinction of the individual event counts (num-

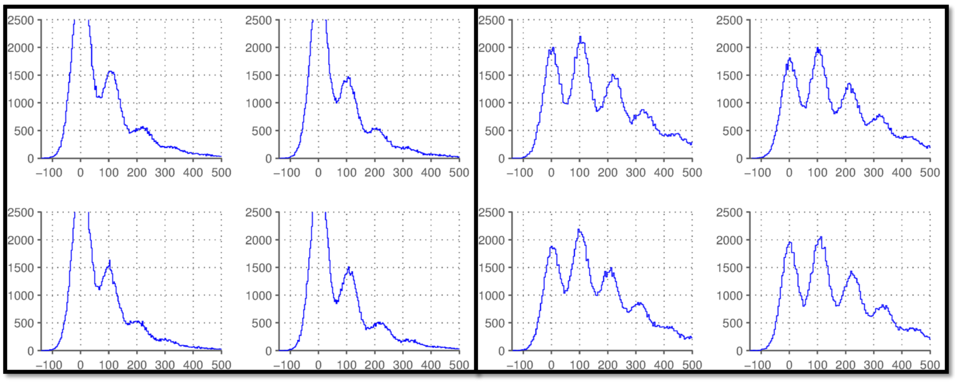

Figure 5.30: MPPC #233 in single channel mode. Bias voltage is (72.430 ± 0.003) V. Shown are two different light intensities (left plot and right plot).

ber of photons) and also the very slight difference of amplitudes introduced by the uneven breakdown voltages. The effect is however marginal. Figure 5.30 shows the same measurement with the #233 MPPC. These quick measurements have shown that exchanging the front-end detectors is not only possible but that viable results can already be achieved without changes on the existing readout electronics and just slight changes on the post-processing algorithms.

Chapter 6

Light and signal sources for the test setup

Artificial light sources to simulate a Cherenkov pulse and or the night sky background are used in conjunction with the PMTs to test the camera electronics. However, calibration of the electronics is more difficult with PMTs as signal sources due to the statistical nature of the signal formation. This makes the application of electric pulser to simulate the PMTs necessary for controlled and reproducible results. The following sections discuss these light and signal sources in more detail.

6.1 The light sources

The light events seen by an IACT camera can be divided into two sources: the Cherenkov light of a cosmic ray event and the night sky background light containing all other light sources. The Cherenkov light is very fast and the photons are correlated, while the NSB is permanently present and the photons are uncorrelated. These conditions can be simulated in the lab as described in the following.

6.1.1 Emulation of Cherenkov pulses

The choice of the Cherenkov light emulation is significantly reflected in the quality of the gathered results for the electronics. Hence, a reliable, steady, reproducible and precise light source is needed for that purpose. First experiences were gained with a self-built laser system with a blue laser diode and a laser driver chip [77]. The circuit worked well in terms of light pulse production. However, the light pulses had a FWHM of about 6 ns and hence were too long to simulate the short Cherenkov-like pulses. The laser system was also not steady enough for long term measurements. A better solution was found with a professional laser system from PicoQuant [78]. The PicoQuant laser system consists of the control unit PDL 800-D and the temperature regulated 50 mW laser-diode head LDH-D-C-405. The laser has a wavelength of (405±10) nm and a pulse FWHM of <70 (low power) and <500 ps (high power). The pulse-to-pulse jitter is about 2.6 ps, as stated in the product specifications. The laser diode should be operated within the lasing regime to achieve a stable and compact light pulse.

The laser intensity can be adjusted with the control unit, which unfortunately changes the spot size of the laser. Furthermore, it is very difficult to consecutively set the same intensity with the dial. A better method is to use neutral density (ND) filters, which attenuate or reflect the laser light. The pulse repetition rate is set to the lowest value of 31.25 kHz to avoid any interfering of consecutive events. The laser control unit is used as the master trigger and is connected via a delay line to the FC250 boards. The delay line prevents crosstalk of the trigger signal upon the measured PMT signal. Triggering the control unit from an external source is possible but not recommended, since the trigger pulses have to be rather long to be recognized by the control unit and hence forbid the production of ultrashort laser pulses. Moreover, the laser spot changes its shape and the pulse duration and intensity are unstable with the use of an external trigger.

The optical bench setup contains a piece of white paper in front of the laser output, tilted by about 45° to avoid reflections into the laser system, which could damage the diode. The paper reduces the intensity and a following pinhole with 370 μm diameter reduces the solid angle of the laser beam. The trimmed beam passes first a filter setup with three single absorption ND filters (Thorlabs: NE510B, NE513B, NE520B) with optical densities of 1.0, 1.3 and 2.0. The filters can only be put separately into the beam. Two more 'filters' are added for letting pass the beam without any attenuation and for blocking the beam completely. The next stage is a step variable circular ND filter wheel (Thorlabs: NDC-50S-3) with optical densities of 0.04, 0.2, 0.4, 0.6, 0.8, 1.0, 2.0 and 3.0. The laser beam is thereafter focused with 1 m distance directly or via a 8 m plastic fiber on the PMT.

The optical bench is calibrated with a photodiode (Hamamatsu S1227-16BR) placed in the beam and directly readout with a picoampere meter (Keithley 6487). Table 6.1 lists the total optical density D and the corresponding transmission $T = 10^{-D}$ as well as the measured and normalized transmission T_N for the wheel alone and for the three absorption filters together with the 0.04 density of the wheel. The uncertainties are estimated as being about 10% but for the lowest transmission value (~20%), since that ND filter is more difficult to determine.

Optical density D [ ]	Transmission T [%]	Measured and normalized transmission T_N [%]
0.04	91.2	100
0.2	63.1	66.3
0.4	39.8	43.3
0.6	25.1	27.9
0.8	15.8	15.9
1.0	10.0	9.0
2.0	1.0	0.5
3.0	0.1	0.03
1.04	9.1	7.9
1.34	4.6	2.9
2.04	0.9	0.2

Table 6.1: Calibration of the optical bench.

6.1.2 Emulation of night sky background

The night sky background consists, as mentioned earlier, of light sources which are not originating from cosmic rays and their secondary products. The main sources are stars, the moon and light from nearby cities scattered at the sky. The telescope's camera sees these sources either as uniformly distributed or point-like but uncorrelated light. Operation of the camera is only possible, if the NSB per pixel is rather low (<200 MHz [49]), or in case of a star shining into a pixel, if the pixel is turned off. The individual NSB amplitudes measured in a single PMT are only between one and a few photoelectrons large, since the NSB photons are uncorrelated.

The NSB can be emulated by a filament bulb or another light source that covers the according wavelength regime. A filament bulb is rather steady after it has reached its working temperature, but its current consumption needs to be monitored at all measuring time. The disadvantage of a bulb is its wavelength spectrum that peaks in the red regime around 750 nm, as shown in figure 6.1. The quantum efficiency of most IACT PMTs is $\lesssim$1-2% in that wavelength range and the values vary with up to 100% from PMT to PMT. This makes the filament bulb a good NSB source, but an unreliable light source for PMT comparing measurements. A light source with a spectrum matching the QE curve of the PMTs is more suitable for such

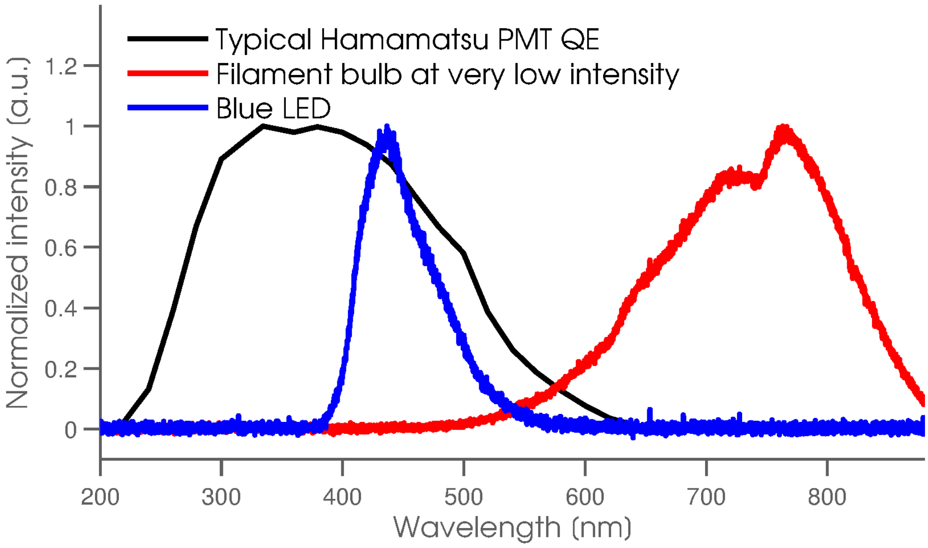

Figure 6.1: Spectra of a filament bulb (red) and a blue LED (blue) compared with the average quantum efficiency of a Hamamatsu R11920-100-01 PMT (black).

measurements. A good choice is to use a blue LED, which spectrum overlaps much better with the QE (figure 6.1).

The filament bulb chosen for the NSB measurements is a standard 6 V, 3 W bulb with bayonet base (Philips 6910). It is operated with currents of 100 to 250 mA and placed such that the light is faint enough to generate NSB up to 700 MHz (figure 6.2). A blue LED mounted in a white plastic sphere of about 40 mm diameter and placed in a box with a white POM window for light diffusion is used for comparative measurements. The uniformity of the construction is tested with a spectrum analyzer by running it over the POM window and checking the amplitude of the light yield. The box is place about 1 m in front of the PDP module, illuminating uniformly all PMTs. Figure 6.3 shows the average NSB rate seen by all twelve PMTs according to a set LED current. The NSB rate is estimated by subtracting the channel offset, measured separately without NSB, of each pixel individually, then summing up all samples of a measured event (= area under the waveform) and dividing this sum by the area of a single photoelectron pulse.

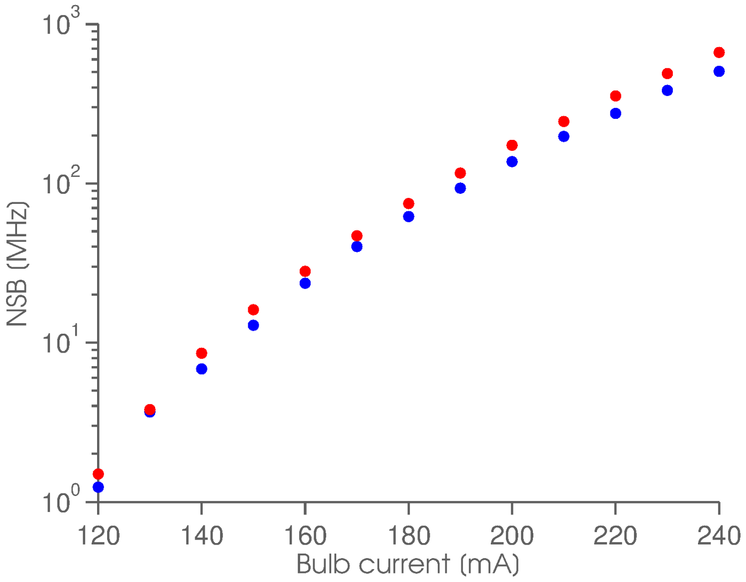

Figure 6.2: NSB rate in function of the filament bulb current for PMT voltages of 1000 (blue) and 1360 V (red). PMT is a Hamamatsu R11920-100-01.

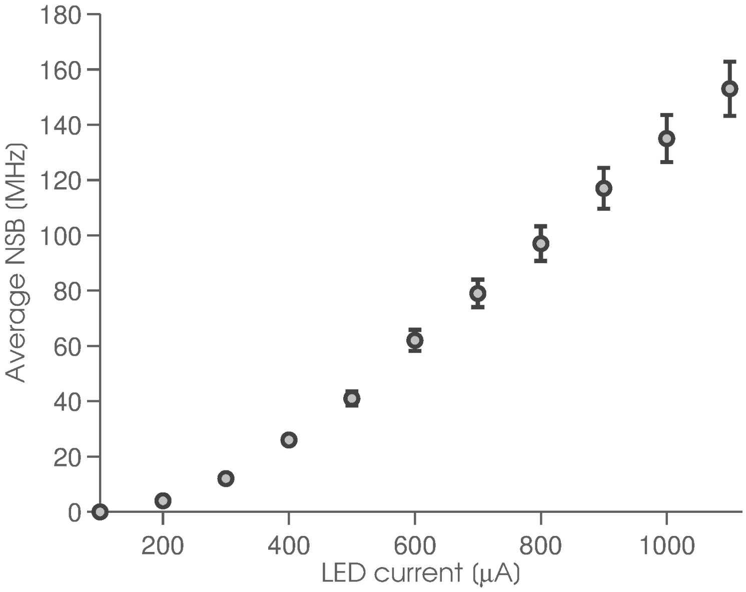

Figure 6.3: Mean NSB rate measured with the twelve PDP PMTs at 40000 gain in function of the LED current.

6.2 Emulation of a PMT with a charge terminator

The emulation of a PMT output pulse can be done by replacing the PMT with a charge terminator consisting of a single capacitor that acts like an AC coupling. This capacitor corresponds to the capacitance of the PMT, which mainly defines together with the load resistor the trailing edge of the output pulse. The leading edge is defined by the charge collection time at the anode of the PMT. This time is mainly determined by the transit time spread (TTS) for the secondary electrons. Typical TTS for linear focusing dynode PMTs are in the order of 0.3 to 2 ns (1.3 ns for the first batch and 2.0 ns for the second batch of Hamamatsu PMTs). This can be simulated with a step function signal with adjustable slope fed into the charge terminator capacitor. Most PMTs are capable of providing $\geq$100 MHz analogue bandwidths over a large range of output pulse amplitudes. The capacitance of the PMT and the load resistor limit the analogue bandwidth (BW) of the PMT, which can be estimated by

$$\mathrm{BW} = \frac{0.35}{2.2 \cdot RC} \tag{6.1}$$

with R being the load resistor and C the capacitance of the PMT. The capacitance of the used PMTs are ~5 pF for the Photonis XP2960, ~8 pF for the Hamamatsu R11920-100-01 and ~4.5 pF for the Hamamatsu R11920-100-05 PMT. The load resistor has hence been changed from 2 kΩ, to 1 kΩ and back to 2 kΩ for the different PMTs to maintain the same analogue bandwidth of about 16-20 MHz. The capacitors used for the charge terminator are a 4.7 pF and a 10.2 pF multilayer ceramic capacitor (VP31BA100KA, Vishay Vitramon). They are charged by the square-pulse generator Datapulse 110B with fixed amplitude. The leading slope of the generator's negative pulses is adjusted such that the output leading slope of the charge terminator corresponds to the expected ~8 ns of the PMT. The amplitude of the signal is adjusted with an attenuator (Trilithic BMA-580, S/N 4213), wired between the pulse generator and the capacitor. An additional 50 Ω resistor in front of the charge terminator prevents signal reflections. The charge or number of electrons that is loaded into the capacitor can be calculated as

$$Q = \int u(t) C dt \tag{6.2}$$

with Q the total charge, $u(t)$ the square wave voltage and C the capacitance of the charge terminator.

Chapter 7

Monte Carlo camera simulation

Many measurements have been done to test and verify the functionality of the fully digital FlashCam approach on the level of single pixels with external light or pulse sources. For the physics case, a full camera performance is of more relevance but difficult to measure in the lab. Hence, a Monte Carlo (MC) simulation is set up to determine the performance of the FlashCam on 'real' Cherenkov pulses and NSB. One measure of performance of an IACT telescope is its effective detection area, which defines the area a telescope 'sees' at a time. This effective detection area depends strongly on the cosmic-ray energy and impact distance to the telescope, but also on camera parameters like digitization rate and trigger efficiency. The MC data production was set up by K. Bernlöhr, MPI-K Heidelberg, with the official CTA MC software packages to simulate the shower formation and development, the telescope mechanics parameters and a simple camera electronics for the digitization of the signals. The data are analyzed for ADC sampling rates of 250 MSps and 1 GSps and effective detection area plots produced to show the performance.

7.1 Monte Carlo data production

The MC simulation contains the steps from the shower generation induced by a cosmic ray, the Cherenkov light production and development towards ground, the imaging of the Cherenkov light into the camera focal plane, the photo-detector with its statistics and finally the electronics behind the photo-detector. A PMT is simulated as photo-detector and the electronics is implemented in a simplified form. The output signals of the PMT, which in the simulation are individual single photo-electron delta-like pulses induced by the Cherenkov and NSB photons, are convolved with measured

PMT pulses for the 250 MSps and the 1 GSps system to get the correct tail time constant and the analogue bandwidth of the electronics. The single convolved photo-electron pulses are added up and the resulting signal is digitized either with 250 MSps or 1 GSps and the signal waveform (raw data) of each pixel written to disk.

The MC simulation is done with several software packages [79]. The software CORSIKA (COsmic Ray SImulations for KAscade, [80]) generates a cascade of extensive air showers induced by high-energetic cosmic particles like gamma rays, protons, electrons, etc. The output of the generator contains, amongst other information, the location, arrival time, and wavelength of the produced Cherenkov photons. Cherenkov light hitting single or arrays of IACT telescopes with predefined locations can be simulated by using the *IACT*-option of the simulation package. An array of four midsize telescopes with 12 m dish diameter and a focal length of 16.7 m is implemented for the production of the data used in this study.

The CORSIKA output is fed into the next software package, the *sim_telarray* [53], which simulates the atmospheric absorption of the Cherenkov light and the camera details of the telescope(s). The software contains a raytracing of the Cherenkov photons from hitting the mirrors until entering the PMTs after passing light funnels. The simulation of the PMT characteristics like quantum efficiency, gain and afterpulsing, triggering schemes on pixel and on telescope level, and the digitization of the analogue signals is included as well. The single signal path and the linear-nonlinear amplifier introduced by FlashCam is not yet implemented in the software for lack of time. Instead, a dual signal path with linear transmission of the signals, as described in section 2.3, is implemented.

The output data of *sim_telarray* contain the raw waveforms, calibration data, pedestals, photo-electron conversion factors, ADC conversion factors, impact parameter and energy of the primary particle, etc. These data can be extracted from the nearly 1 TB of MC data files with a modified version of the *read_hess* software and written to files readable and processable with MATLAB. The waveform data used to calculate the numbers presented in the following sections are differentiated in MATLAB to get rid of the long PMT pulse tail, before being processed further.

7.2 Telescope detection efficiency

7.2.1 Accidental trigger rate

The accidental trigger rate (ATR) describes the trigger rate caused by events with solely NSB content. The ATR depends, besides the NSB rate, on the trigger class performance and on the trigger threshold. A low trigger threshold produces a large ATR but allows the detection of low energy gamma-ray events with low Cherenkov light yield, which otherwise may slip through with a higher threshold. Normally, an ATR is specified according to the data acquisition system and the corresponding trigger threshold determined with simulations. The trigger threshold values in function of the ATR is determined by running the 173 MHz NSB MC data through the trigger class routine, without applying a threshold on the trigger data.
The implemented trigger class is a sum class which sums first unique patches of three pixels (P3) and subsequently sums seven unique three-pixel patches (P3-7). This is done in two steps to allow for a possible clipped sum and a digital bandwidth reduction of the P3. The output of the trigger class for each analyzed data sample is binned in function of amplitude. The cumulative sum of the bins is subtracted from the total number of processed samples and plotted in a histogram, as shown in figure 7.1 for the 250 MSps and in figure 7.2 for the 1 GSps data. The plots show the integrated number of triggered samples above trigger threshold in function of the threshold. The trigger threshold of the 250 MSps data for the selected ATR of 100, 500 and 3000 Hz are 10.15, 9.28 and 8.46 in arbitrary units. The trigger threshold of the 1 GSps data for the selected ATR of 100, 500 and 3000 Hz are 13.86, 12.26 and 10.9 in arbitrary units, respectively. These trigger thresholds are applied to the gamma-ray data to determine the effective detection area of the telescope.

7.2.2 Effective detection area

An IACT telescope can 'see' the Cherenkov light of a shower, as long as the telescope is located within the Cherenkov light pool that can extend over areas ~400 times larger than the mirror area of the telescope. The area that the telescope can observe is the area of the light pool of a shower, called the detection area. Only gamma rays entering the atmosphere perpendicular to the ground are taken into account for the definition of the detection area. Figure 7.3 shows a sketch of a telescope located in the Cherenkov light pool of two gamma ray events with the same energy and the resulting detection area.

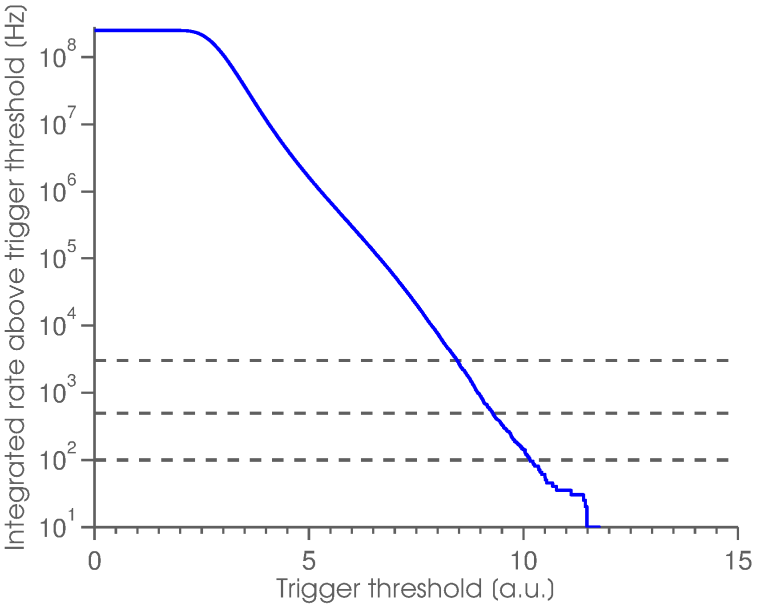

Figure 7.1: Integrated accidental trigger rate above trigger threshold plotted against the trigger threshold for the 250 MSps data. The NSB rate of the MC data is 173 MHz. The horizontal lines define the accidental trigger rates for 100, 500 and 3000 Hz.

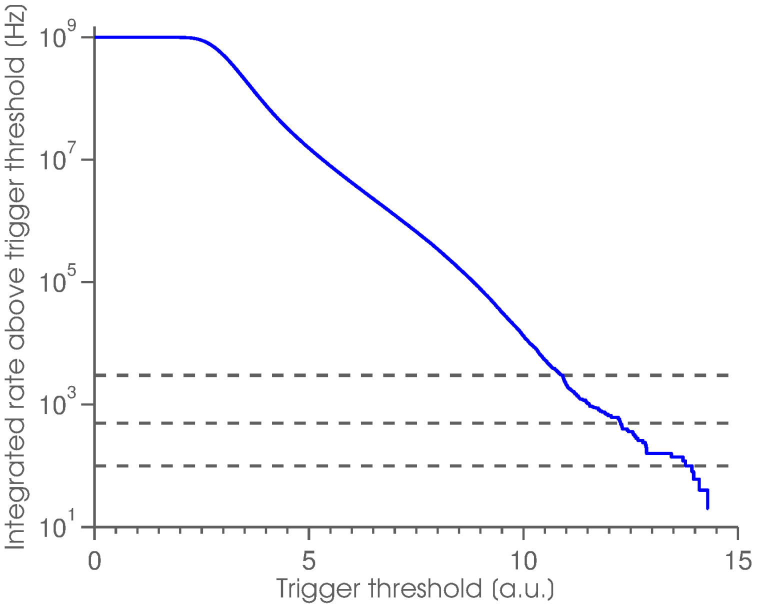

Figure 7.2: Integrated accidental trigger rate above trigger threshold plotted against the trigger threshold for the 1 GSps data. The NSB rate of the MC data is 173 MHz. The horizontal lines define the accidental trigger rates for 100, 500 and 3000 Hz.

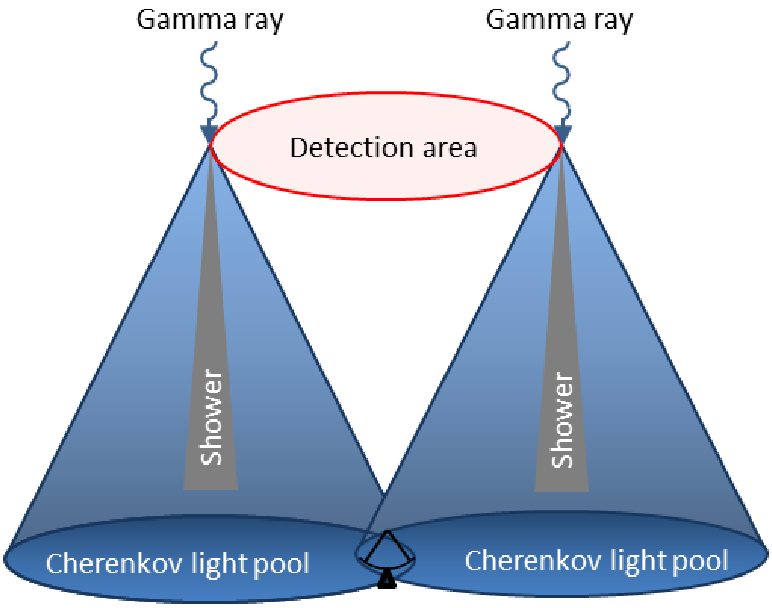

Figure 7.3: Sketch for the explanation of the detection area of a telescope. A telescope located within the Cherenkov light pools, induced by gamma rays of the same energy impinging the atmosphere perpendicular to the ground, 'sees' all gamma rays entering perpendicular through the indicated detection area.

The effective detection area of an IACT telescope takes also the efficiency of the telescope to detect an event into account. This efficiency includes mainly the photo-detector and trigger efficiency. The effective detection area can only be defined for a given energy interval. Hence, the MC data has to be binned in energy to calculate the effective area. For each energy bin, a detection efficiency ϵ is calculated. The detection efficiency is determined by the ratio of detected events and total number of incident gamma rays. $\epsilon(E, I)$ is calculated per impact parameter interval I, since the detection efficiency depends on the telescope location within the shower. The impact parameter I is the distance between the shower center and the telescope, as mentioned previously in section 1.3.4. Figure 7.4 shows the binned detected ($M(E, I)$) and binned total ($N(E, I)$) events in function of the impact parameter for different energy bins. The detection efficiency is given as

$$\epsilon(E, I) = \frac{M(E, I)}{N(E, I)} \tag{7.1}$$

with the impact parameter interval $I = [r_{i+1} - r_i]$ and r_i the lower edge

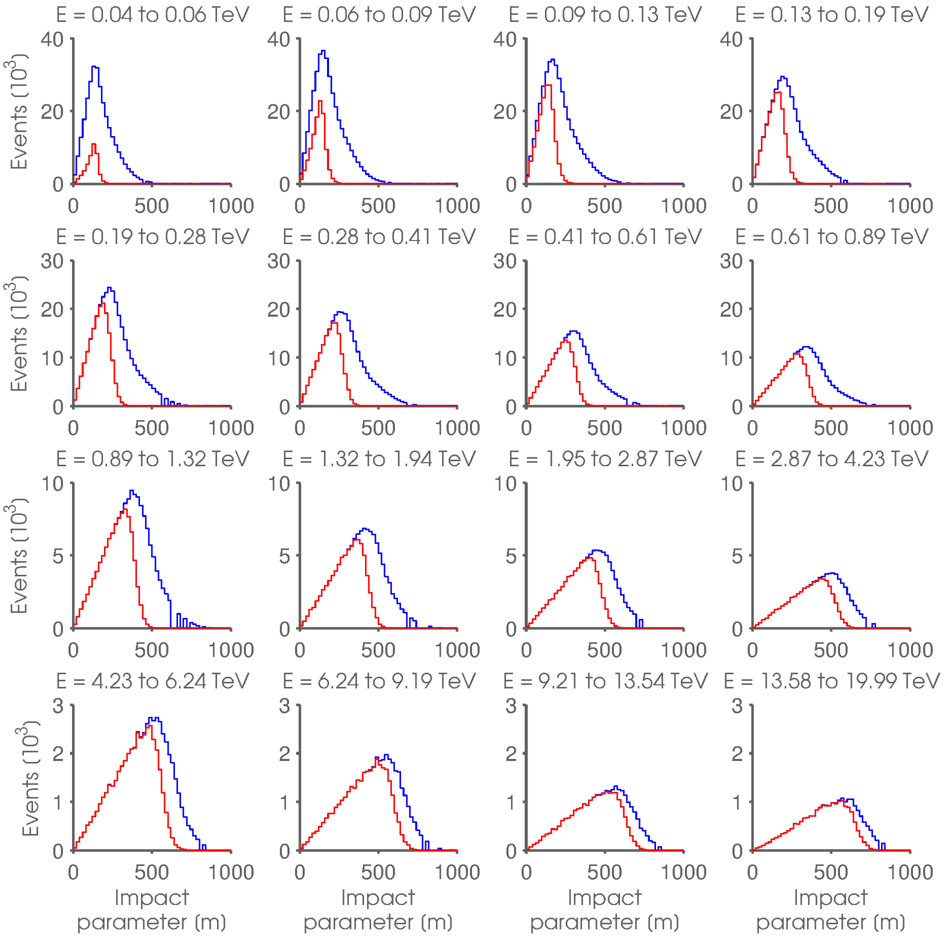

Figure 7.4: Plot of the binned number of triggered (red) and total (blue) events of the 250 MSps data in function of the impact parameter (horizontal axis) for 16 energy bins. The empty bins at larger impact parameters in some histograms are due to lack of data statistics. Note the different y-axes.

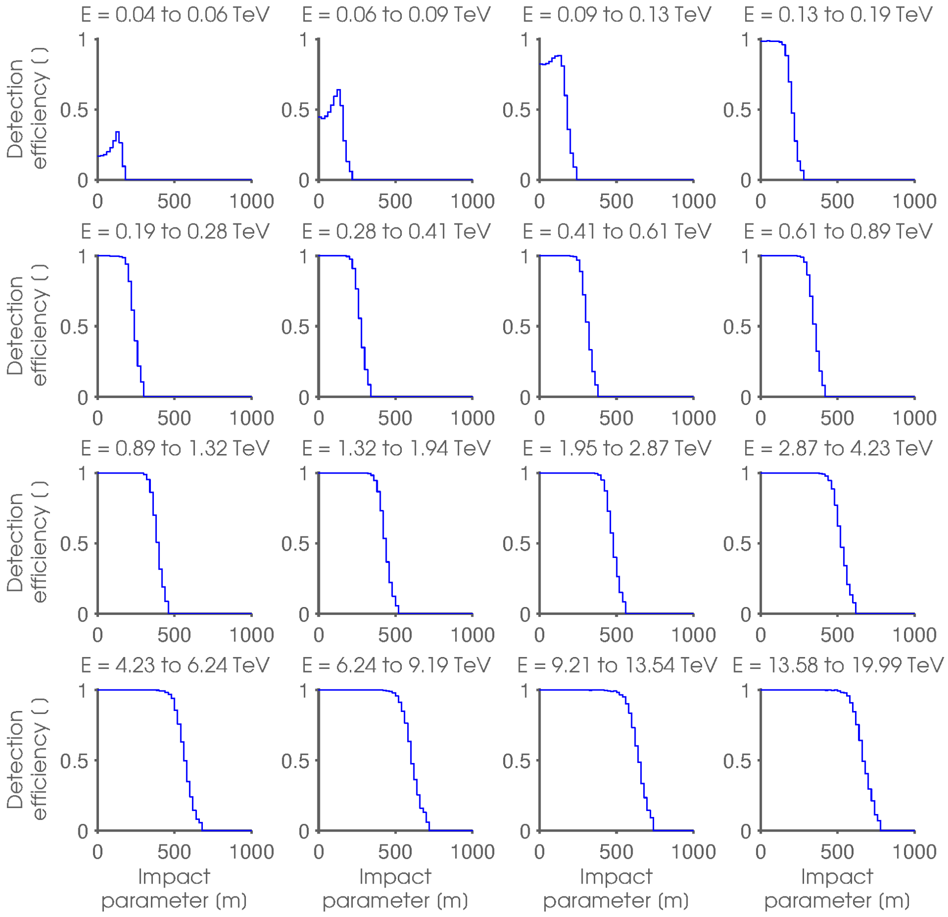

Figure 7.5: Plot of the binned detection efficiency $\epsilon(E, I)$ in function of the impact parameter (horizontal axis) for 16 energy bins.

of the impact parameter bin i (corresponds to the radial distance of the telescope to the shower center). Figure 7.5 shows the detection efficiency for the 250 MSps data in function of energy bins. The effective detection area for an energy bin E is finally the integrated detection efficiency over the whole light pool:

$$A_{eff}(E) = \sum_{i=1}^{n-1} \frac{M(E,I)}{N(E,I)} (r_{i+1}^2 - r_i^2)\pi \tag{7.2}$$

with n the total number of impact parameter bins. Equation 7.2 has to be corrected by the factor $2\pi(1 - \cos(\theta))$ for cosmic particles with a non-perpendicular incident angle θ.

The calculated effective detection area $A_{eff}(E)$ per energy bin can be plotted against the energy, as shown in figure 7.6. The effective detection area data points are calculated with a cut in the detection efficiency at 5%, avoiding outliers due to statistical fluctuations at large impact parameters. The energy is binned logarithmicaly in 80 bins within the energy range of 20 GeV to 20 TeV. The impact parameter is binned in 15 m wide bins. The plot shows a slightly better performance of the 250 MSps system above 200 GeV and a smaller effective detection area at lower energies compared to a 1 GSps system. However, these curves should be taken with care since both systems (i.e. the analogue signal path) are implemented in a very simplified manner in the MC production. Using a clipped sum also improves the results of the 250 MSps system, as inofficial simulations done by A. Manalaysay have shown. The 250 MSps FlashCam seems to be very competitive to a faster system according to the MC simulations.

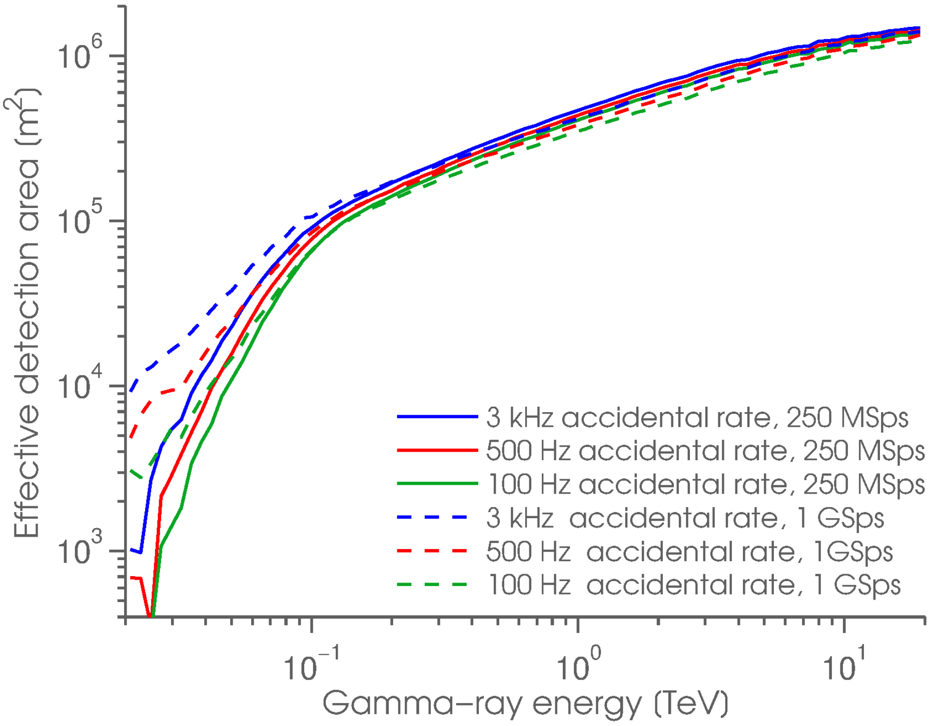

Figure 7.6: Effective detection area of a mid-size telescope of 12 m diameter and a focal length of 16.7 m for a digitization electronics with 250 MSps (blue) and 1 GSps (red) in function of the gamma-ray energy and for different trigger thresholds.

Chapter 8

Concluding remarks

Several concepts for the first fully digital IACT camera have been studied, developed and improved. The first step was the verification of the MC simulations dealing with the sampling speed of analogue-to-digital converters. The measurements have reproduced the MC results and have strengthen the confidence in the simulations. These first simulations have shown that using ADC sampling rates of 250 MSps in an IACT camera allow for a similar performance as current systems with higher sampling rates. The linear-nonlinear amplifier circuit for the amplification of the analogue detector signals has been tested in conjunction with the FC250 digitization electronics and the results show that the behavior of the circuit is well reproducible and mainly understood. The connection of the front-end detector electronics with the FC250 has been tested with various CAT6 cables. Signal crosstalk tests have shown that crosstalk is never larger than about 2.5 pe even for the cheaper and more light-weight unshielded twisted-pair cables.

The field of IACT telescopes can surely profit from a very flexible trigger implementation and from electronics that are suitable for various photodetectors as PMT or MPPCs. The use of a linear-nonlinear amplifier allows for a single signal path per pixel and hence reducing the number of signal channels, ADCs and subsequent FPGAs. This again lowers the power consumption and the costs for such a camera.

Appendices

A.1 Low pass Bessel filter

The low pass filters were designed with the freeware ELSIE [81]. Figure A.1 and table A.1 show the filter schematics and the component values for the 5th order Bessel filters with 10, 80 and 230 MHz cutoff frequency. The input and output impedance is 50 Ω.

Cutoff frequency [MHz]	L1 [nH]	L2 [nH]	L3 [nH]	C1 [pF]	C2 [pF]
10	1.8	620	130	360	160
80	220	82	18	39	18
230	75	27	6.2	15	6.8

Table A.1: Component values for 5th order Bessel low pass filters. The simulated values have been rounded to the nearest E24 values.

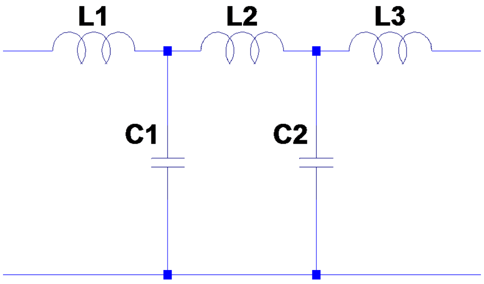

Figure A.1: Low pass 5th order LCLCL filter.

A.2 High voltage generator

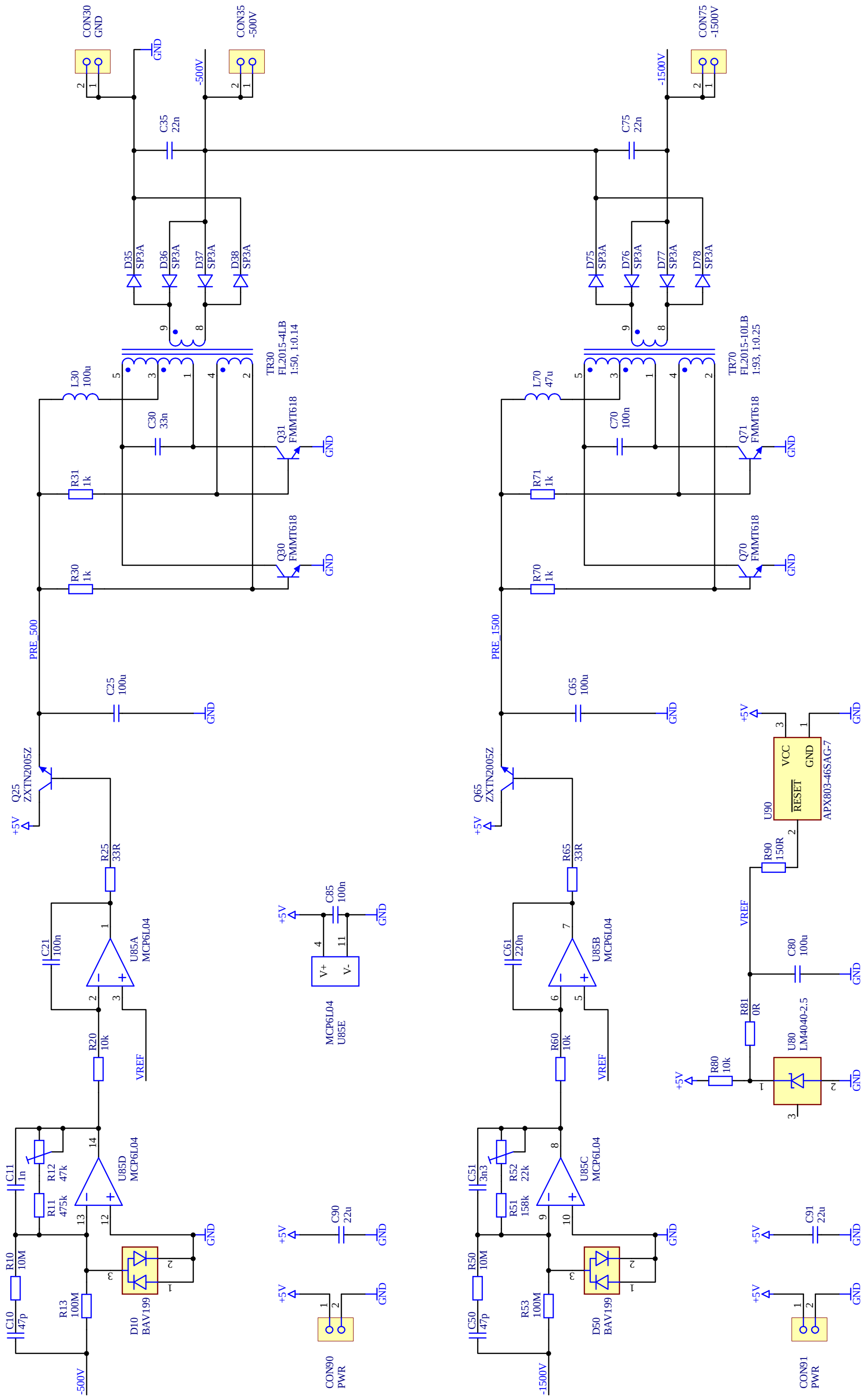

A.3 PDP PMT active base

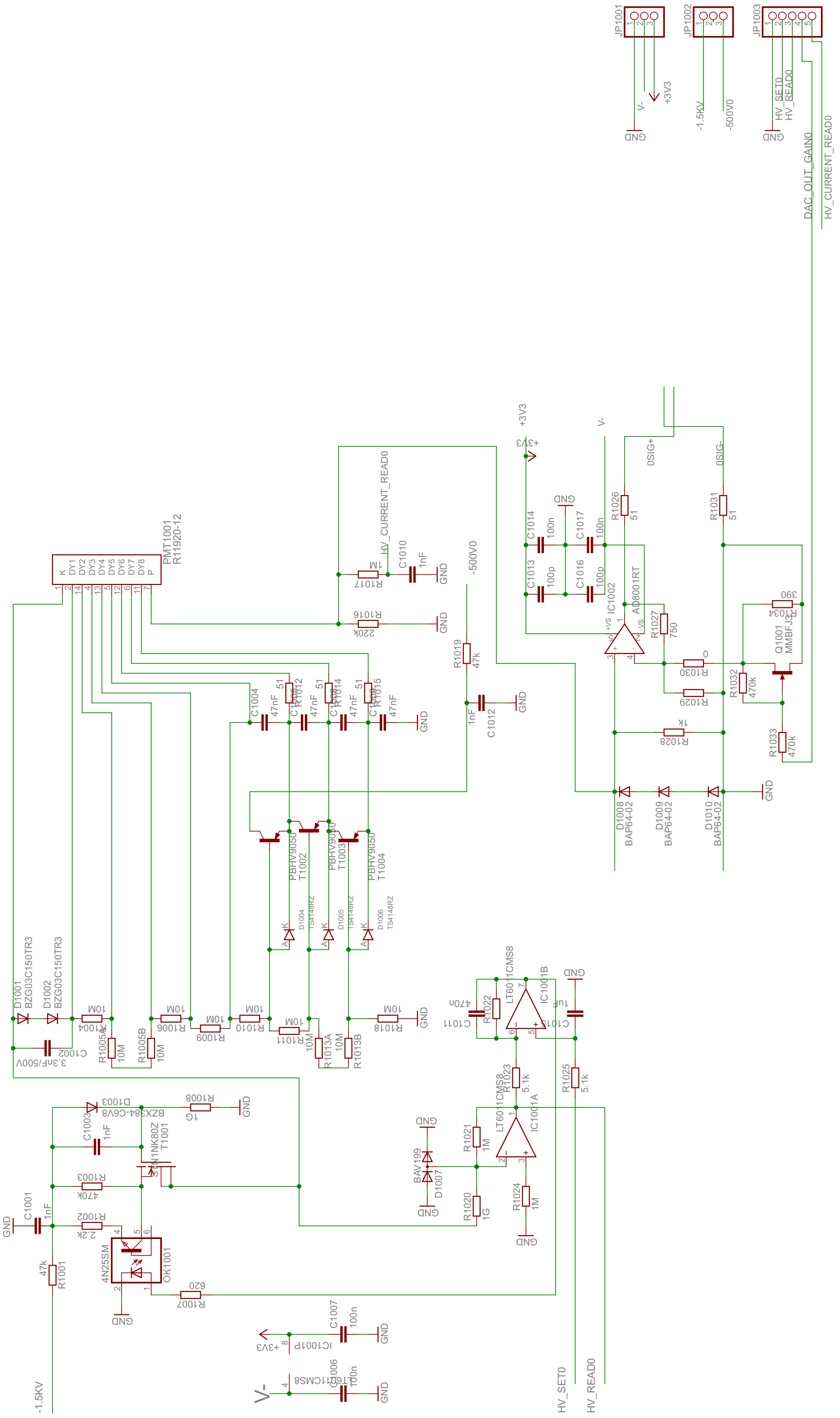

A.4 ADC-driver input stage of the FC250

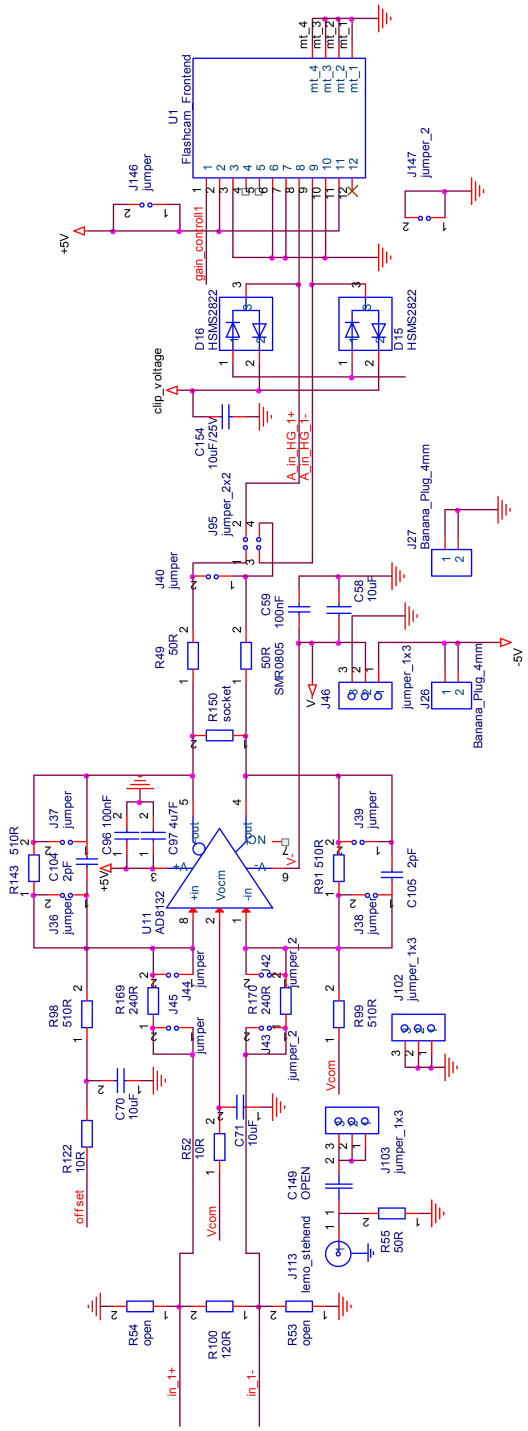

A.5 Commands for the *fc250* software

The most important commands used with the fc250 software are showing single triggered events on screen like a scope and saving of a number of triggered events in a file:

- `./fc250 eth0,efb1,1 0 512 0 ff`
- `./fc250 eth0,efb1,1 1000 > filename.txt 245 -10 26`

The single pieces of the first command line are: *./fc250* runs the program, *eth0* defines the Ethernet card of the computer, *efb1* is the address of the FC250 board. The numbers describe the board ID, number of events to be stored in the file (0 opens up a graphics window and sets the *fc250* in scope mode), number of samples per event (max. 512), read out start referenced to the trigger (also negative numbers are possible for pre-trigger data) and a mask for the ADC channels in HEX that are read out (ff = all eight channels). The second command line for instance writes 1000 triggered events of channels 2, 3 and 6 with 245 samples per event in the file *filename.txt*, starting 10 samples before the trigger.

A.5.1 FC250 synchronization

The procedure and the commands needed to set both boards in a master and slave stage, and to read them out simultaneously are:

- power off both boards
- change DIP-switch 2 of the slave board to 0x2 (sets the Ethernet address of the board: 0xefb2)
- connect the RJ45 plug 'Clk_Sync_Trig_OUT' of the master and the 'Clk_Sync_Trig_IN' of the slave with a CAT5 cable (as short as possible to reduce the shifting of the clock phase)
- put jumper on J10 of slave board (clock source is now external)
- connect both boards over Ethernet to a computer
- power on both boards
- if necessary, add delay (max. 2 ns) of the transmitted clock on the master with the command[1]: `./fc250 eth0,efb1,1 1 16 0 ff -11 0 x0a1 x21 0 -11 0 x0a2 x1a 0 -11 0 x0a0 0 0`

---

[1] The data sheet of the clock generator chip AD9517-4 gives the equation how to calculate a clock delay (pages 46/47).

- change the parameter x1a in the previous command line to adjust the clock phases measured with a scope at R369 (master) and R373 (slave)

These steps have to be completed once only, since all parameters are stored in the FPGAs. There may still be jumps of the slave clock phase of ±2 ns from time to time, however, this only affects the time measurements. The synchronization of the trigger signal, which is also sent over the CAT5 cable, needs to be set every time the boards are powered on. The steps are:

- add ′-101 13 x37 x23′ without the ′ ′ to each master *fc250* command line. This routes the trigger signal coming from the laser control unit and fed into the trigger input (LEMO_4) to the ′Clk_Sync_Trig_OUT′ output

- add ′-101 13 xd xb′ to each slave *fc250* command line. This selects the external trigger delivered over the ′Clk_Sync_Trig_IN′ input as the trigger source

- if reading out both boards simultaneously, start the slave *fc250* first to have synchronous event numbers in the files

A time stamp is saved in the data file for each trigger event. Synchronization of the time stamps can be done with an external clock generator signal of about 1 pps (TTL signal with ≥16 ns high state) fed over two equally long cables into the LEMO_7 input of the boards. It is also possible to use the internal clock generator of the master board, connecting LEMO_1 of the master with the two LEMO_7 and adding the command ′-101 12 xaca0 x3b9′ to the master *fc250* command line.

A.6 Pole-zero cancellation

The principle of operation of the pole-zero cancellation (PZC) for discrete data has been explained in section 4.5.1. A more mathematical approach starting with the formation of the PMT signal, using electronic circuits, is shown here to explain the PZC. The PMT can be approximated as a CR-circuit responding to a step function (figure A.2 first and second plot). The C is the capacitance of the PMT and the R is the load resistor connected to the PMT. The transfer function of the CR circuit after Laplace transformation is

$$H_{PMT}(s) = \frac{\tau_p s}{\tau_p s + 1} \tag{A.1}$$

with $\tau_p = CR = C_p R_p$. Differentiation of this signal is performed with another CR circuit, so that the new transfer function becomes

$$H_{\textit{PMT+diff}}(s) = \frac{\tau_p s}{\tau_p s + 1} \cdot \frac{\tau_d s}{\tau_d s + 1} \tag{A.2}$$

with $\tau_d = C_d R_d$ and poles at $s = \{-1/\tau_p; -1/\tau_d\}$. The output of the CR-CR circuit (figure A.2 third plot) shows an undershoot, which will cause an uncertainty in the amplitude reconstruction, if pile-up occurs. Modifying the second CR circuit as shown in figure A.3 leads to the transfer function

$$H_{\textit{PMT+diff+pole-zero}}(s) = \frac{\tau_p s}{\tau_p s + 1} \cdot \frac{\frac{R_d}{R_{pz}+R_d} + (R_d||R_{pz})C_d s}{(R_d||R_{pz})C_d s + 1}. \tag{A.3}$$

Choosing $R_{pz} = \tau_p / C_d$ will eliminate the pole of the first CR circuit which introduces the undershoot. The new transfer function has no poles and no undershoot anymore (figure A.2 bottom)

$$H_{\textit{PMT+diff+pole-zero}}(s) = \frac{\tau_p \tau_d s}{\tau_p + \tau_d \ + \tau_p \tau_d s}. \tag{A.4}$$

The pole and thus the undershoot are only compensated as long as R_{pz} is exactly τ_p / C_d. Temperature changes and component tolerances will always lead to a slight over or under compensation of the undershoot, which will introduce a small error in the amplitude reconstruction of a piled-up pulse.

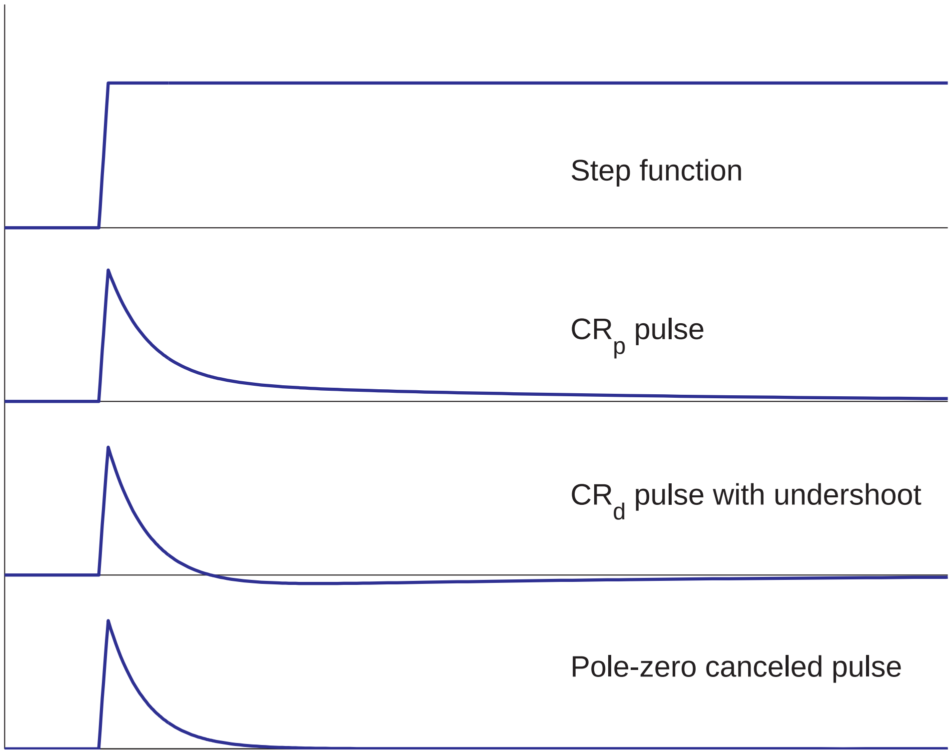

Figure A.2: A step function (top) is fed into a CR circuit to simulate a PMT on a load resistor (curve 2). Another CR circuit simulated the differentiation of the PMT signal and introduces the undershoot (curve 3). Modifying the second CR circuit by adding a small portion of the original signal to the differentiated one eliminates the undershoot (bottom).

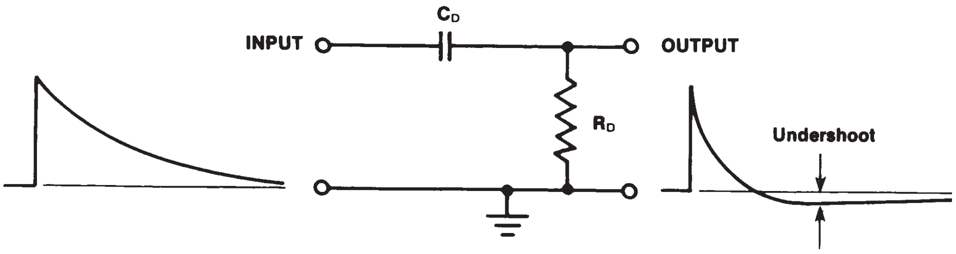

(a) Simple CR Differentiator

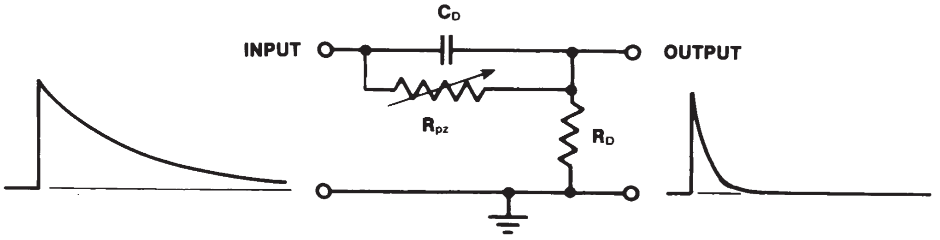

(b) CR Differentiator with Pole-Zero Cancellation

Figure A.3: Differentiator circuit without (top) and with (bottom) pole-zero cancellation. Picture taken from [82], Fig. 12, p.6.

References

[1] Th. Wulf, "Beobachtungen über die Strahlung hoher Durchdringungsfähigkeit auf dem Eiffelturm." Physikalische Zeitschrift Nr. 11 (1910) 811-813.

[2] A. Gockel, "Luftelektrische Beobachtungen bei einer Ballonfahrt." `http://www.unifr.ch/sfsn/pdf/Gockel%20Phys%20Zeitsch%20XI%201910%20p280.pdf`. Physikalische Zeitschrift Nr. 11 (1910) 280-282.

[3] V. Hess, "Über Beobachtungen der durchdringenden Strahlung bei sieben Freiballonfahrten." `http://www.mpi-hd.mpg.de/hfm/HESS/public/HessArticle.pdf`. Physikalische Zeitschrift Nr. 13 (1912) 1084-1091.

[4] A. A. Watson, "Extensive Air Showers and Ultra High Energy Cosmic Rays." `http://www.ast.leeds.ac.uk/Auger/augerthesis/thesis.htm`. Pierre Auger Observatory, Lectures 2002.

[5] "The Large Hadron Collider." `http://public.web.cern.ch/public/en/LHC/LHC-en.html`.

[6] "Cosmic ray spectrum, W. Hanlon." `http://www.physics.utah.edu/~whanlon/spectrum.html`.

[7] R. Beck, "Galactic and Extragalactic Magnetic Fields," *arXiv*, no. 0810.2923v4 [astro-ph], 2009.

[8] T. C. Weekes, *Very high energy gamma-ray astronomy*. Inst of Physics Pub, 2003.

[9] "CTA The Cherenkov Telescope Array." `http://www.cta-observatory.org/`.

[10] A. Goldwurm, "An overview of the high-energy emission from the Galactic Center," *arXiv*, no. 1007.4174v1 [astro-ph.HE], 2010.

[11] D. Hooper and L. Goodenough, "Dark Matter Annihilation in The Galactic Center As Seen by the Fermi Gamma Ray Space Telescope," *arXiv*, no. 1010.2752v3 [hep-ph], 2011.

[12] H.E.S.S. Collaboration: F. Aharonian et al., "Very high energy gamma rays from the direction of Sagittarius A*," *arXiv*, no. 0408145v2 [astro-ph], 2004.

[13] "TeVCat, Catalog for TeV astronomy." `http://tevcat.uchicago.edu/`.

[14] E. O. Ofek et al., "An outburst from a massive star 40 days before a supernova explosion," *Nature*, no. Nature **494**, 65-67, doi:10.1038/nature11877, 2013.

[15] MAGIC collaboration, "A Model of the Spectral Evolution of Pulsar Wind Nebulae," *arXiv*, no. 1004.3098v1 [astro-ph.HE], 2010.

[16] Fermi-LAT collaboration, "Gamma-ray flares from the Crab Nebula," *arXiv*, no. 1011.3855v3 [astro-ph.HE], 2011.

[17] G. Di Sciascio, for the ARGO-YBJ collaboration, "ARGO-YBJ: Status and Highlights," *arXiv*, no. 1210.2635v1 [astro-ph.HE], 2012.

[18] G. L. Israel, *A Systematic Search of New X-ray Pulsators in ROSAT Fields*. PhD thesis, Trieste, 1996.

[19] C. Grupen, *Astroparticle physics*. Springer, 2005. ISBN 3540253122.

[20] He Gao et al., "Bright broad-band afterglows of gravitational wave bursts from binary neutron star mergers as a probe of millisecond magnetars," *arXiv*, no. 1301.0439v1 [astro-ph.HE], 2013.

[21] "CHANDRA X-ray observatory." `http://chandra.harvard.edu/resources/ppt/xray/index.html`.

[22] HESS Collaboration: F.A. Aharonian, et al., "Fast variability of TeV gamma-rays from the radio galaxy M87," *arXiv*, no. 0612016v1 [astro-ph], 2006.

[23] E. G. Berezhko and H. J. Völk, "Theory of cosmic ray production in the supernova remnant RX J1713.7-3946," *A&A 451, 981-990*, no. DOI: 10.1051/0004-6361:20054595, 2006.

[24] G. Bertone, D. Hooper and J. Silk, "Particle Dark Matter: Evidence, Candidates and Constraints," *arXiv*, no. 0404175v2 [hep-ph], 2004.

[25] P. D. Serpico and D. Hooper, "Gamma rays from dark matter annihilation in the central region of the Galaxy," *arXiv*, no. 0902.2539v3 [hep-ph], 2009.

[26] Various authors, *Encyclopaedia of Occupational Health and Safety*. International Labour Organization, 1998.

[27] I. Frank and I. Tamm. Comptes rendus de l'Acad. Sci. U.R.S.S., 14 (1937) 109.

[28] M. Döring et al., "Measurement of the Cherenkov light spectrum and of the polarization with the HEGRA-IACT-system," *arXiv*, no. 0107149v2 [astro-ph], 2001.

[29] S. Gillessen, *Sub-Bogenminuten-genaue Positionen von TeV-Quellen mit H.E.S.S.* PhD thesis, Ruprecht-Karls-Universität Heidelberg, 2004.

[30] D. Tescaro, "Timing analysis of the MAGIC telescope data after the installation of the ultra-fast 2 GSamples/s FADC readout," Master's thesis, IFAE, Barcelona, September 2007.

[31] "Particle Data Group." `http://pdg.lbl.gov/`.

[32] "Cosmic ray / Gamma-ray / Neutrino and similar experiments, list maintained by K. Bernlöhr." `http://www.mpi-hd.mpg.de/hfm/CosmicRay/CosmicRaySites.html`.

[33] "The Energetic Gamma Ray Experiment Telescope (EGRET)." `http://heasarc.gsfc.nasa.gov/docs/cgro/egret/`.

[34] R. Ong, "Very high-energy gamma-ray astronomy," Tech. Rep. 305, Elsevier Physics Reports, http://dx.doi.org/10.1016/S0370-1573(98)00026-X, Nov 1998.

[35] "EGRET all-sky map." `http://heasarc.gsfc.nasa.gov/docs/cgro/cgro/egret_allsky.html`.

[36] "Fermi, Gamma-ray Space Telescope." `http://fermi.gsfc.nasa.gov/`.

[37] "NASA Goddard space flight center." `http://imagine.gsfc.nasa.gov/docs/features/exhibit/glast_exhibit.html`.

[38] "NASA Fermi." `http://www.nasa.gov/mission_pages/GLAST/news/gamma-ray-census.html`.

[39] "The Pierre Auger Observatory." `http://www.auger.org/`.

[40] The Pierre Auger Collaboration, "The Fluorescence Detector of the Pierre Auger Observatory," *arXiv*, no. 0907.4282v1 [astro-ph.IM], 2009.

[41] HiRes Collaboration, "First Observation of the Greisen-Zatsepin-Kuzmin Suppression," *arXiv*, no. 0703099v2 [astro-ph], 2008.

[42] P. Sokolsky, for the HiRes Collaboration, "Final Results from the High Resolution Fly's Eye (HiRes) Experiment," *arXiv*, no. 1010.2690v2 [astro-ph.HE], 2010.

[43] "The Telescope Array Project." `http://www.telescopearray.org/`.

[44] L. Thompson, "The discovery of air-Cherenkov radiation," *Cern Courier*, no. Volume 52, number 6, 2012.

[45] T.C. Weekes et al., "Observation of TeV gamma rays from the Crab nebula using the atmospheric Cerenkov imaging technique," *DOI*, no. 10.1086/167599, 1989.

[46] A. M. Hillas, "Cerenkov light images of EAS produced by primary gamma," pp. 445–448, August 1985. 1985ICRC....3..445H.

[47] D. Britzger, "Studies of the Influence of Moonlight on Observations with the MAGIC Telescope," Master's thesis, Ludwig-Maximilians-Universität, München, June 2009.

[48] Y. Becherini et al. for the CTA consortium, "Advanced analysis and event reconstruction for the CTA Observatory," *arXiv*, no. 1211.5997v1 [astro-ph.IM], 2012.

[49] The CTA Consortium, "Design Concepts for the Cherenkov Telescope Array," *arXiv*, no. 1008.3703v3 [astro-ph.IM], 2012.

[50] "HAWC, The High Altitude Water Cherenkov Experiment." `http://umdgrb.umd.edu/hawc/science.php`.

[51] R. Winston, *Nonimaging optics*. Academic Press, 2005.

[52] B.K. Lubsandorzhiev, "On the history of photomultiplier tube invention," *arXiv*, no. 0601159v1 [physics.ins-det], 2006.

[53] K. Bernlöhr, "Simulation of Imaging Atmospheric Cherenkov Telescopes with CORSIKA and sim_telarray," *arXiv*, no. 0808.2253v1 [astro-ph], 2008.

[54] M. Kurz, "Precision Measurements of Ultra-fast Low Light Level Candidate Sensors for the CTA Project," Master's thesis, Max-Planck-Institut für Physik, München, February 2011.

[55] "FACT First G-APD Cherenkov Telescope." `http://www.isdc.unige.ch/cta/fact`.

[56] H. Anderhub et al., "FACT - the First Cherenkov Telescope using a G-APD Camera for TeV Gamma-ray Astronomy," *arXiv*, no. 1010.2397v2 [astro-ph.HE], 2010.

[57] A. Daum et al., "First Results on the Performance of the HEGRA IACT Array," *arXiv*, no. 9704098v1 [astro-ph], 1997.

[58] "Hamamatsu." `http://www.hamamatsu.com/`.

[59] "DRS Chip, PSI." `http://drs.web.psi.ch/`.

[60] D. Tescaro et al., "The readout system of the MAGIC-II Cherenkov Telescope," *arXiv*, no. 0907.0466v1 [astro-ph.IM], 2009.

[61] E. Delagnes et al., "SAM: A new GHz sampling ASIC for the H.E.S.S.-II front-end electronics," *Nuclear Instruments and Methods in Physics Research Section A: Accelerators, Spectrometers, Detectors and Associated Equipment*, no. doi:10.1016/j.nima.2006.05.052, 2006.

[62] D. Haefner, "Development of a new analog Sum-trigger for the MAGIC experiment with a continuously adjustable analog delay line and automatic calibration," Master's thesis, Ludwig-Maximilians-Universität, München, November 2010.

[63] "CTA FADC simulations by Thomas Kihm." `http://www.mpi-hd.mpg.de/personalhomes/mizzi/cta-simulation/`.

[64] I. Fedorko, S. Tokar, I. Chirikov-Zorin, "Simulation of Photomultiplier Response," *CERN document server*, no. ATL-TILECAL-99-012, 1999.

[65] T. Kihm, MPI-K Heidelberg, "Private communication."

[66] C. Owen, "Owen resistive splitter." `http://www.microwaves101.com/encyclopedia/Resistive_splitter2.cfm`, December 2011.

[67] "MATLAB." `http://www.mathworks.ch/products/matlab/`.

[68] G. Pühlhofer et al., "FlashCam: A fully digital camera for CTA telescopes," *arXiv*, no. 1211.3684v1 [astro-ph.IM], 2012.

[69] "National Semiconductors: AN-597 Current Feedback Amplifiers." `www.national.com/an/AN/AN-597.pdf`.

[70] U. Tietze, Ch. Schenk, *Halbleiterschaltungstechnik, 13. Auflage*. Springer, 2010.

[71] Lutz von Wangenheim, *Analoge Signalverarbeitung*. Vieweg+Teubner Verlag, 2010. ISBN 3834807648.

[72] "LTSpice." `http://www.linear.com/designtools/software/`.

[73] "Analog Dialogue." `http://www.analog.com/library/analogDialogue/archives/43-09/Edch%201%20op%20amps.pdf`.

[74] "Intersil: AN-9420.1 Current Feedback Amplifier Theory and Applications." `www.intersil.com/data/an/an9420.pdf`.

[75] R. Dossi, A. Ianni, G. Ranucci, and O. Y. Smirnov, "Methods for precise photoelectron counting with photomultipliers," Tech. Rep. 623-637, Nucl. Instrum. Meth. A451, 2000.

[76] R. J. Stokey and P. J. Lee, "Approximation to the Probability Density at Output of a Photomultiplier Tube," Tech. Rep. 36, TDA Progress Reports 42-73, 1983.

[77] A. Gadola, "A fast online and triggerless signal reconstruction based on cross-correlation," Master's thesis, Physik-Institut of the University of Zürich, January 2009.

[78] "PicoQuant GmbH, Rudower Chaussee 29, D 12489 Berlin." `www.picoquant.com`.

[79] K. Bernlöhr et al., "Monte Carlo design studies for the Cherenkov Telescope Array," *arXiv*, no. 1210.3503v1 [astro-ph.IM], 2012.

[80] "D. Heck et al., CORSIKA, extensive air shower generator." `http://www-ik.fzk.de/corsika/`.

[81] "Elsie, Windows program for electrical filter design." `http://tonnesoftware.com/elsie.html`.

[82] "ORTEC, Introduction to amplifiers." `www.ortec-online.com/download/Amplifier-Introduction.pdf`.

Acknowledgments

Now the work is almost done and the last sentences are written. However, the last words shall not belong to physics but to the expression of my deepest gratitude to all of the people who have assisted and supported me with great effort and personal contributions. First and foremost I would like to thank Ueli Straumann for giving me the chance to realize this PhD thesis in his unique group. With his support and his generosity he encouraged me and gave me the possibility to work independently, to realize my own ideas and to continue my education. A big thank you for this Ueli. My special thanks go to Achim Vollhardt and Stefan Steiner for their very valuable input and discussions on electronics, mechanics and life. I enjoyed their very pleasant and interesting company in particular while being on construction jobs and at meetings all over the world. Our common Currywurst experiences will be remembered with a big smile. Another person who earns a big thank you for his substantial contributions, his priceless tips and some long, instructive, and often amusing discussions is Thomas 'Mizzi' Kihm. I would also like to express my gratitude to Aaron Manalaysay for his great thoughts and his assistance in helping me to find my way back to the right path when I was at a dead end. I very much appreciate his very valuable input and comments during the correction of the thesis. Thanks to Roland Bernet, who always had a minute to spare for solving my various IT problems. I would also like to say thank you to the mechanical workshop team, in particular to Kurt Bösiger, and to the electronics workshop with Peter Soland and Daniel Florin. The administrative staff Carmelina Genovese, Monika Röllin and Ruth Halter deserves a thank you for supporting me in managing the subtleties of the administration jungle and for the diverting chats. I would also like to thank all the other colleagues of the physics institute, and especially Ueli's group for the very interesting and pleasant time at the institute. Thanks Roman, Ben, Olaf, Nicola, Christian, Marco, Michel, Johnny, Mark, Albert, Katharina, Angela, and Christophe for all the laughter and the lively and thought-provoking discussions. I very much enjoyed

sharing with you thoughts about physics, life and being a PhD student.

I'm also very grateful to the following people for their great support and for opening up new fields of life and physics to me: German Hermann, Konrad Bernlöhr, Christian Bauer, Christian Föhr, Stefan Schlenstedt, and everybody who contributed to make the last four years an interesting, instructive and nice time.

Before I finally close this thesis I would like to express my deepest gratitude to my parents, my brothers and their families, my friends and especially to Adeline, who all supported me emotionally during the last four years and in particular during the time of writing of the thesis.

CURRICULUM VITAE

PERSONAL INFORMATION

Last Name: Gadola
First Name: Arno
Date of birth: 08. April, 1975
Hometown: Disentis/Mustér, GR

EDUCATION

2009–2013	**Dissertation** in Physics, University of Zurich *Towards the First Imaging Atmospheric Cherenkov Telescope Camera with Continuous Signal Digitization* Supervisor: Prof. Dr. Ulrich Straumann
2009	**Master of Science in Physics** at University of Zurich
2008–2008	Master Thesis, University of Zurich *A fast online and triggerless signal reconstruction based on cross-correlation* Supervisor: Prof. Dr. Ulrich Straumann, Dr. Achim Vollhardt
2007–2007	Bachelor Thesis, University of Zurich *Identification of isolated photons at high energies at H1* Supervisor: Prof. Dr. Ulrich Straumann, Dr. Katharina Müller
2004–2009	Study of Physics, University of Zurich
2004–2004	Specialist for Excel, Hewlett Packard, Dübendorf, ZH
2002–2003	Development engineer at Integral Drive Systems AG, Zurich
2001–2002	Attending preparatory course at WIAM, School of Jazz, Winterthur
1999–2001	Development engineer at Integral Drive Systems AG, Zurich
1999	**Elektroingenieur HTL**
1995–1999	Study of electrical engineering, Neu Technikum Buchs, Buchs SG
1991–1995	Apprenticeship as Elektroniker, Hamilton Bonaduz AG, Bonaduz GR